EUROPEAN ORGANISATION FOR NUCLEAR RESEARCH

CERN-PPE/90-114
August 14, 1990

The OPAL Detector at LEP

The OPAL Collaboration.

Abstract

The OPAL detector at the e^+e^- storage ring LEP is designed to provide precise measurements of charged particles and of electromagnetic energy over nearly the full solid angle. Its main elements are a central tracking system, a solenoidal coil, an electromagnetic calorimeter made of lead glass, a hadron calorimeter made of iron and wire chambers, and a muon detector. A pair of forward detectors is used to measure the luminosity and to identify particles emitted at small angles with respect to the beam line. In this paper all detector elements are described and their performance is discussed.

This paper is dedicated to the memory of Mario Morpurgo,
who died on May 29th 1990

(submitted to Nucl. Instr. and Meth.)

K. Ahmet[12], M.Z. Akrawy[11], G. Alexander[21], J. Allison[14], P.P. Allport[5], B.E. Anderson[13], K.J. Anderson[8], J.C. Armitage[6], R.L. Armstrong[8], G.T.J. Arnison[18], G. Artusi[2], P. Ashton[14], G. Azuelos[16], J.T.M. Baines[14], L. Baisin[7], A.H. Ball[15], J. Banks[14], R.L. Bard[15], G.J. Barker[11], R.J. Barlow[14], J.R. Batley[5], G. Bavaria[16], C. Beard[7,a], M. Beaulieu[16], F. Beck[7], A. Beer[7], T. Behnke[7], K.W. Bell[18], G. Bella[21], O. Biebel[3], L. Bifferi[2], I.J. Bloodworth[1], P. Bock[10], H. Börner[7,b], H.M. Bosch[10], F. Bourgeois[7], H. Breuker[7], L. Briot[7], R.M. Brown[18], R. Brun[7], A. Buijs[7], H.J. Burckhart[7], G. Canova[7], P. Capiluppi[2], R.K. Carnegie[6], A.A. Carter[11], J.R. Carter[5], M. Chamot[7], C.Y. Chang[15], A. Charalambous[13], D.G. Charlton[7], J.L. Chevalley[7], J.T.M. Chrin[14], S.A. Clark[18,c], I. Cohen[21], D.C. Colley[1], J.D. Colmer[15], J.E. Conboy[13], J.F. Connolly[18], B. Cornet[7], M. Couch[1], M. Coupland[12], R. Cranfield[13], G. Crone[13], M. Cyvoct[7], I. D'Antone[2], S. Dado[20], G.M. Dallavalle[2], O.W. Davies[14,d], M.M. Deninno[2], L.G. Denton[18], F.L. Desrosier[15], A. Dieckmann[10], M. Dittmar[4], M.S. Dixit[17], D. Duchesneau[16], E. Duchovni[24], G. Duckeck[10], I.P. Duerdoth[14], B.G. Duff[13,i], D. Dumas[6], A. Dupenloup[7], H. El Mamouni[16], P.A. Elcombe[5], E. Elsen[10], P.E. Estabrooks[6], W.M. Evans[18], A. Eyring[3], F. Fabbri[2], M. Ferrari[2], P. Farthouat[19], M. Fillion[7], H.M. Fischer[3], A.L. Fletcher[5], M.T. French[18], C. Fukunaga[22], G. Gagnon[16], B. Gaillard-Grenadier[7], Y. Gal[24], B. Gandois[19], O. Ganel[24], H. Gao[9], J.W. Gary[10], J. Gascon[16], N.I. Geddes[18], C.N.P. Gee[18], S.W. Gensler[8], F.X. Gentit[19], G. Giacomelli[2], V. Gibson[5], W.R. Gibson[11], G. Giles[6], J.D. Gillies[18], P. Giudici[7], R.G. Glasser[15], W. Glessing[7], L. Godfrey[17,f], T. Goiffon[7], J. Goldberg[20], P.R. Goldey[15], M.J. Goodrick[5], P. Gorce[7], W. Gorn[4], D. Granite[20], E. Gross[24], S. Gross[3], M. Grossi[7], J. Grunhaus[21], M. Guillot[7], J. Hagemann[7], R. Hammarstrom[7], M. Hansroul[7], C.K. Hargrove[17], J. Hart[5], H. Hartmann[3], P.M. Hattersley[1], D. Hatzifotiadou[7], M. Hauschild[7], C.M. Hawkes[7], J. Heintze[10], R.J. Hemingway[6], R.-D. Heuer[7], F.F. Heymann[13], J. Hill[7], J.C. Hill[5], S.J. Hillier[1], P.S. Hinde[14,g], J.D. Hobbs[8], P.R. Hobson[23], D. Hochman[24], B. Holl[7], R.J. Homer[1], S.R. Hou[15], C.P. Howarth[13], R.E. Hughes-Jones[14], R. Humbert[9], P. Igo-Kemenes[10], M. Imori[22], D.C. Imrie[23], S. Jaroslawski[18], P.W. Jeffreys[18], M.D. Jeffs[18], H. Jeremie[16], M. Jimack[7], E. Jin[4,h], M. Jobes[1], R.W.L. Jones[11], D. Joos[9], P. Jovanovic[1], D. Karlen[6], K. Karner[7], K. Kawagoe[22], T. Kawamoto[22], R.G. Kellogg[15], B.W. Kennedy[13], C. Kleinwort[7], D.E. Klem[17], G. Knop[3], T. Kobayashi[22], P. Kobe[3], L. Köpke[7], T.P. Kokott[3], R. Kolpin[9], M. Koshiba[22], R. Kowalewski[6], H. Kreutzmann[3], J. Kroll[8], P. Kyberd[11], G.D. Lafferty[14], F. Lamarche[16], M. Lamblin[7], B. Langeset[7], W.J. Larson[4], D. Lascols[19,i], M.M.B. Lasota[11], M. Lautscham[10], J.G. Layter[4], P. Le Du[19], P. Leblanc[16], A. Lefrancois[7], D. Lellouch[7], P. Lennert[10], L. Lessard[16], L.J. Levinson[24], A. Levy[21], J.A. Lidbury[18], G. Linser[7], S.L. Lloyd[11], F.K. Loebinger[14], J.M. Lorah[15], B. Lorazo[16], R. Lorenzi[7], R. Losserand-Madoux[7], M.J. Losty[17], J. Ludwig[9], N. Lupu[20], J. Ma[4,h], A.A. Macbeth[14], M. Mannelli[7], S. Marcellini[2], G. Maringer[3], M. Marquet[7], L. Marradi[13], J.P. Martin[16], T. Mashimo[22], F. Massera[2], M. Mast[7], R.M. Matson[18], H. Matsumura[10], P. Mättig[3], E. Mauer[3], U. Maur[3], L. Mazzone[7], T.J. McMahon[1], A.C. McPherson[6,j], F. Meijers[7], D. Menszner[10], F.S. Merritt[8], H. Mes[17], H.J. Meyer[9], A. Michelini[7], D. Micolon[19], R.P. Middleton[18], K. Miels[6], G. Mikenberg[24], R.S. Milborrow[18], D.J. Miller[13], W.W. Miller[15], C. Milstene[21], A. Mincer[20,k], M. Minowa[22], W. Mohr[9], A. Montanari[2], M. Morpurgo[7,i], M.W. Moss[14], A. Muller[19], P.G. Murphy[14], W.J. Murray[5], B. Nellen[3], E. Neuheimer[17], H.H. Nguyen[8], M. Nozaki[22], A.J.P. O'Dowd[14], S.W. O'Neale[7], B. O'Neill[1], M. O'Neill[6], F.G. Oakham[17], M.J. Oreglia[8], S. Orito[22], B. Parkinson[18], G.N. Patrick[18], S.J. Pawley[14], R. Payne[6], A. Penton[18,l], J.O. Petersen[7], J.E. Pilcher[8], J.L. Pinfold[24], D.E. Plane[7], E. Pod[8], A. Possoz[8,e], F. Pouyat[7], G. Pozzo[7], T.W. Pritchard[11], G. Prodon[7], G. Quast[7], J. Raab[7], P. Rada[7], P. Rapp[15,m], M.W. Redmond[8], D.L. Rees[1], M. Regimbald[16], A. Renoux[7], K. Riles[4], C.M. Roach[5], F. Rochner[9], A. Rollnik[3], J.M. Roney[8], A.M. Rossi[2,n], M.D. Rousseau[18,i], P. Routenburg[6], P.S. Rozmarynowski[15,o], K. Runge[9], O. Runolfsson[7], R. Rusniak[10], D. Rybkowski[7], H. Sanders[8], R.A. Sansum[18], A. Sato[22,s], B.J. Saunders[18], A.D. Schaile[9], O. Schaile[9], W. Schappert[6], P. Scharff-Hansen[7], K. Scheuring[9], G. Schmidlin[7], H. von der Schmitt[10], S. Schreiber[3], J. Schwarz[9], W. Seidl[7], U. Seidler[9], D.M. Sendall[7], V. Sergo[7], R. Shally[6], A. Shapira[24], R.J. Shaw[5], B.C. Shen[4], P. Sherwood[13], M. Shoa[24], A. Simon[3], G.P. Siroli[2], A. Skuja[15], A.M. Smith[7], T.J. Smith[1], K.H. Souten[18], E.J. Spreadbury[13,i],

R.W. Springer[15], M. Sproston[18], R.J. Staley[1], P.H. Steinberg[15,i], K. Stephens[14], R. Stephenson[18], H.E. Stier[9], W.N. Stokes[1], D. Strom[8], H. Takeda[22,t], T. Takeshita[22], A. Therond[7], J. Thiebes[3], Y. Totsuka[22,u], T. Tsukamoto[22], S. Tuffanelli[2], M.F. Turner[5], G. Tysarczyk[10], M. Uldry[7], D. Van den plas[16], G.J. VanDalen[4], F. Verkerk[7], D. Voillat[7], C.J. Virtue[17], B. Vuillerme[7], P. Vande Vyvre[7], A. Wagner[10], C. Wahl[9], P. von Walter[10], H. Wang[4,h], C.P. Ward[5], D.R. Ward[5], J. Waterhouse[6,q], P.M. Watkins[1], A.T. Watson[1], N.K. Watson[1], M. Webel[9], H.C. Weber[9], S. Weisz[7], A. Weltin[9], H. Wenninger[7], N. Wermes[10], M. Weymann[7], D.J. White[18], P. Wicht[7], G.W. Wilson[7], J.A. Wilson[1], I. Wingerter[7], N.C. Wood[13], S. Wotton[7], B. Wünsch[3], T.R. Wyatt[14], R. Yaari[24], S. Yamada[22,v], H. Yamashita[22], G. Yekutieli[24], K. Zankel[7], T. Zawistowski[15,p], W. Zeuner[7], J. Zimmer[10], G.T. Zorn[15], N. Zwang[24], S. Zylberajch[19].

[1]School of Physics and Space Research, University of Birmingham, Birmingham, B15 2TT, UK
[2]Dipartimento di Fisica dell' Universita di Bologna and INFN, Bologna, 40126, Italy
[3]Physikalisches Institut, Universität Bonn, D-5300 Bonn 1, FRG
[4]Department of Physics, University of California, Riverside, CA 92521 USA
[5]Cavendish Laboratory, Cambridge, CB3 0HE, UK
[6]Carleton University, Dept. of Physics, Colonel By Drive, Ottawa, Ontario K1S 5B6, Canada
[7]CERN, European Organisation for Particle Physics, 1211 Geneva 23, Switzerland
[8]Enrico Fermi Institute and Dept. of Physics, University of Chicago, Chicago Illinois 60637, USA
[9]Fakultät für Physik, Albert Ludwigs Universität, D-7800 Freiburg, FRG
[10]Physikalisches Institut, Universität Heidelberg, D-6900 Heidelberg, FRG
[11]Queen Mary and Westfield College, University of London, London, E1 4NS, UK
[12]Birkbeck College, London, WC1E 7HV, UK
[13]University College London, London, WC1E 6BT, UK
[14]Department of Physics, Schuster Laboratory, The University, Manchester, M13 9PL, UK
[15]Dept. of Physics and Astronomy, University of Maryland, College Park, Maryland 20742, USA
[16]Laboratoire de Physique Nucleaire, Universite de Montreal, Montreal, Quebec, H3C 3J7, Canada
[17]National Research Council, Herzberg Institute of Astrophysics, Ottawa, Ont. K1A 0R6, Canada
[18]Rutherford Appleton Laboratory, Chilton, Didcot, Oxfordshire, OX11 0QX, UK
[19]DPhPE, CEN Saclay, F-91191 Gif-sur-Yvette, France
[20]Department of Physics, Technion-Israel Institute of Technology, Haifa 32000, Israel
[21]Department of Physics and Astronomy, Tel Aviv University, Tel Aviv 69978, Israel
[22]Int. Center for Elementary Particle Phys. and Dept. of Phys., Univ. of Tokyo, Tokyo 113, Japan
[23]Brunel University, Uxbridge, Middlesex, UB8 3PH, UK
[24]Nuclear Physics Department, Weizmann Institute of Science, Rehovot, 76100, Israel

[a]Present address: British Aerospace, Stevenage, UK
[b]Present address: Philips, Hamburg, FRG
[c]Present address: Digital Equipment Corporation, Basingstoke, UK
[d]Present address: British Steel, Sheffield, UK
[e]Present address: EPFL, Lausanne, Switzerland
[f]Present address: University of California, Davies, USA
[g]Present address: Ferranti, Manchester, UK
[h]On leave from Harbin Institute of Technology, Harbin, China
[i]Deceased
[j]Present address: Applied Silicon Inc, Ottawa, Canada
[k]Present address: New York University, NY 10003, USA

[l]Present address: Research Machines, Abingdon, UK
[m]Present address: Department of Energy, Washington DC, USA
[n]Present address: Dipartimento di Fisica, Universita della Calabria, 87036 Rende, Italy
[r]Present address: NASA, Goddard Space Flight Center, USA
[q]Present address: Culham Laboratory, Abingdon, UK
[r]Present address: DPS S.A., 1217 Meyrin, Switzerland
[s]Present address: KEK, Japan
[t]Present address: Kobe University, Kobe 657, Japan
[u]Present address: Institute for Cosmis Ray Research, University of Tokyo, Tokyo 188, Japan
[v]Present address: Institute for Nuclear Study, University of Tokyo, Tokyo 188, Japan

1 Introduction

OPAL [1] is one of the 4 large detectors built for the e^+e^- storage ring LEP at CERN. It is a multipurpose apparatus with excellent acceptance for Z^0 decays over a solid angle of nearly 4π. The basic concept guiding its design has been to detect all types of interactions occurring in e^+e^- collisions with efficient and accurate reconstruction and unambiguous classification of the events. The main features of the detector are:

- Tracking of charged particles in the central region of a solenoidal coil with measurements of their direction and momentum, particle identification by dE/dx and reconstruction of primary and secondary vertices at and near the interaction region.

- Identification of photons and electrons and measurement of their energy.

- Measurement of hadronic energy by total absorption using the magnet yoke instrumented as a calorimeter.

- Identification of muons by measurement of their position and direction within and behind the hadron absorber.

- Measurement of absolute machine luminosity using Bhabha scattering events in the very forward direction with respect to the beam line.

The general layout of the detector is shown in fig. 1, indicating the location and relative size of the various components. Fig. 2 shows cross sections of the detector parallel and perpendicular to the beam axis. A system of central tracking chambers is contained inside a solenoid which provides a uniform magnetic field of 0.435 T. The solenoidal coil is surrounded by a time-of-flight counter array, a lead glass electromagnetic calorimeter with a presampler, an instrumented magnet return yoke serving as a hadron calorimeter and four layers of outer muon chambers. A forward detector measures the luminosity.

The LEP beam at the OPAL interaction region, and also the OPAL solenoid axis, is inclined at an angle of 13.9 mrad relative to the horizontal plane. The coordinate system is illustrated in fig. 1; the x axis is horizontal and points approximately towards the centre of LEP, the y axis is approximately vertical, and the z axis is in the e^- beam direction. The polar angle, θ, is measured from the z axis, and the azimuthal angle, ϕ, from the x axis about the z axis.

The central tracking system is divided into a precision vertex detector, a large volume jet chamber and z-chambers. The main tracking is performed with the jet chamber, a drift chamber approximately four metres in length and two metres in radius with 159 layers of wires, providing both high redundancy and precision for the reconstruction of multihadronic events. The central tracking system operates at a pressure of 4 bar and is therefore contained inside a pressure vessel whose cylindrical structure provides mechanical support to the solenoidal coil mounted around it. The pressure vessel is closed at the two ends by bell shaped covers.

The time-of-flight system covers the barrel region, $|\cos\theta|<0.82$. It consists of 160 scintillation counters, 6.8 m long and 45 mm thick, located at a radius of 2.36 m.

The main electromagnetic calorimeter consists of a cylindrical array of 9,440 lead glass blocks of 24.6 radiation lengths ($X_\circ$) thickness, covering $|\cos\theta|<0.82$ in the barrel region, and 2,264 lead glass blocks of 20 $X_\circ$ thickness in the endcaps, covering $0.81<|\cos\theta|<0.98$. Each block subtends a solid

angle of approximately 40×40 mrad^2 and projects towards the interaction region in the barrel region and along the beam direction in the endcaps. The two sections of the electromagnetic calorimeter together cover 98% of the solid angle.

Just inside the lead glass calorimeter and surrounding the pressure vessel, thin gas detectors (presamplers) provide measurements of the position and energy of electromagnetic showers which start in front of the lead glass. The overall energy resolution is improved by correcting for the energy lost in the material in front of the lead glass calorimeter.

The yoke of the magnet is made of welded iron plates, 10 cm thick, with gaps which are instrumented with streamer tubes and form the main hadron calorimeter. The poles are instrumented with thin multiwire chambers and complete the coverage of the solid angle for hadronic shower detection. Since hadronic showers usually begin in the lead glass calorimeter, the hadronic energy is measured by combining the signals of the hadron calorimeter with those of the lead glass.

The entire iron structure is surrounded by several layers of chambers in order to identify muons by measuring the position and direction of all charged particles which have traversed the iron absorber.

The luminosity of the colliding beams is determined by the observation of small angle Bhabha scattering with the forward detector. This device consists of two identical elements surrounding the beam pipe at either end of the central tracking system. Its acceptance covers angles from 40 to 150 mrad from the beam and 2π in azimuth. Each element consists of a lead-scintillator calorimeter of 24 X_0 thickness, divided into 16 azimuthal segments, with three layers of position measuring tube chambers located behind the first 4 X_0. In front of each calorimeter there is a set of precisely located scintillators and drift chambers.

Electronics is contained in multi-storey counting rooms attached to either side of the iron yoke, and in single storey units suspended above the upstream and downstream ends of the detector. Signals are carried from the front end electronics at the detectors to the electronics huts by typically 40 m of twisted pair or coaxial cable. Both sets of electronics huts move as the detector is opened or rolled from its beam to its "garage" position. Access to the inner parts of the detector can be obtained by opening the magnet as illustrated in fig. 3.

In the following sections the detector elements are described in more detail.

2 Magnet and Beam Pipe

2.1 Magnet

The magnet consists of a solenoidal coil and an iron yoke. The coil has to be "thin" and "transparent" for particles produced in the interaction region. This has been achieved by making a self-supporting water cooled solenoid, without the extra mass of a coil-support mandrel, which gives an adequate field strength with less than 5 MW power consumption.

The return yoke is made of soft steel plates. The yoke can be split into five main parts, a central part, two "C"s and two poletips, which can be separately displaced on a system of rails and rollers, to provide access to the experimental apparatus located inside and around the solenoid. An isometric view of the magnet in the "open" position is given in fig. 3. The main magnet parameters are listed in table 1.

In the central cylindrical volume (used for tracking) the magnetic field of 0.435 T is measured to be uniform to within ±0.5%. A severe requirement is that the field in the annular region between the outside of the solenoid and the iron yoke should not exceed a few tens of Gauss. In that region photomultipliers are installed which cannot be operated if the magnetic field is too high. To satisfy the second requirement it has been necessary to wind the solenoid as a single long unit, i.e. it was not possible to split the solenoid into a number of shorter sections assembled together. Shorter sections would have been easier to manufacture but the discontinuity at the joining point of two adjacent sections would have created unacceptable nonuniformities in the magnetic field. Independently powered correction windings at the poletips were also provided, but it has not been necessary to use them.

2.2 Beam Pipe

The beam pipe supports the 4 bar absolute pressure of the gas of the central tracking system. Its structure has been chosen to provide an acceptable transparency in terms of radiation lengths. The inner radius of the pipe was fixed at 78 mm based on the results of calculations of the expected flux of synchrotron radiation [2].

A pipe of carbon fibre composite construction was chosen, following development work carried out at CERN [3]. The radiation length of the carbon fibre epoxy used is estimated to be 235 mm. The pipe consists of a 0.1 mm aluminium tube onto which are epoxied a series of overlapping layers of carbon fibre. The inner skin of aluminium is required for continuity of the conducting surface seen by the wake field of the LEP beams. This reduces the RF losses and local heating. The thickness of aluminium is sufficient to provide electromagnetic shielding of the detector from the bunched beams. The aluminium is also needed to provide a vacuum tight surface with minimum outgassing.

The pipe was made in three sections each about 1150 mm long. In each case the aluminium tube was machined by honing a seamless tube of original wall thickness around 12 mm. The final tubes were of 0.1 mm thickness over their central 1050 mm and then increased in thickness via a ridged taper at each end to provide 4 mm thick end rings suitable for welding the sections together. The carbon fibre was layered by filament winding and was impregnated with high temperature epoxy which permits baking the assembly at 150°C. The central section was made of 1.3 mm thick carbon fibre composite with two 5 mm thick stiffening rings. Together with the aluminium liner, this represents 0.66% of a radiation length. The two outer sections are smooth tubes of 2 mm carbon composite. These three sections were welded together and had end flanges added, before being pumped and baked out. The assembly was filled with dry nitrogen at atmospheric pressure before being installed within the vertex detector. The final pump-down was carried out after the tube had been connected to the rest of the LEP beam pipe.

3 Central Tracking System

3.1 General Concept

The central tracking system consists of three elements, a high resolution vertex detector, a pictorial drift chamber of the "jet chamber" type and the z-chambers. The chambers are shown in figs. 1 and 2 together with the other elements of the detector. The vertex detector, located between the beam pipe and the jet chamber, is used to locate decay vertices of short lived particles and to improve the momentum resolution. The jet chamber records the tracks of charged particles over almost the entire

solid angle and measures their momenta. Particle identification is done by multiple sampling of the energy loss in the gas. The measurement of up to 159 points per track and an excellent two track resolution guarantee a high tracking efficiency. Z-chambers, mounted around the outer mechanical support of the jet chamber, are used to obtain a precise measurement of the z coordinate of the tracks, thereby enhancing the invariant mass resolution. Details of the different tracking chambers may be found in table 2.

3.2 Vertex Detector

The vertex detector is a 1 metre long, 470 mm diameter, cylindrical drift chamber that surrounds the carbon fibre beam pipe and operates within the common 4 bar central tracking system pressure vessel. It is based on a scaled down jet chamber design. The chamber consists of an inner layer of 36 cells with axial wires and an outer layer of 36 small angle (4°) stereo cells.

The axial cells provide a precise measurement of position ($\sigma = 50$ μm) in the r-ϕ plane to aid the measurement of secondary vertex topologies in e^+e^- annihilation events, while maintaining a good multi-hit detection capability to resolve individual particles within jets. Good drift time resolution is obtained by having 4 bar gas pressure and by limiting the maximum drift distance to reduce diffusion effects. A coarse measurement of the co-ordinate (z) along the wire, by measuring the time difference between the signals from the two ends of the anode wire, is used in the fast track trigger and for offline track finding. The combination of stereo and axial cell information provides an accurate z measurement for charged particles close to the interaction region.

Design

The design of the chamber was developed from the experience gained in constructing and operating a prototype chamber [4,5] containing 4 axial cells and 2 stereo cells instrumented with prototype readout electronics. Fig. 4 gives a schematic view of the vertex detector and its associated components. The chamber wires are strung between two 32 mm thick G10 fibreglass end plates that are held 1 metre apart by a single 1.5 mm thick carbon fibre tube located at the detector outer radius of 235 mm. A thin aluminised mylar cylinder, at the detector inner radius of 88 mm, allows a different gas to be used within the pressure vessel of the central tracking system. The preamplifiers and the high voltage distribution components are mounted on each G10 end plate within an extension of the vertex detector gas volume defined by gas-tight inner and outer aluminium cylinders and an aluminium end bulkhead. High voltage and signal cable feedthroughs are inserted into this bulkhead.

The detector is mechanically supported from the inner edge of the jet chamber end cones by two aluminium extender tubes [4,5] and is mechanically independent of the beam pipe.

The vertex detector cell geometry is formed with radial anode and cathode wire planes for each of the axial and stereo cells. Fig. 5 shows the wire layout for 3 cells at one end-plate. The anode planes consist of alternating 200 μm diameter gold plated Cu-Be potential wires and 20 μm diameter gold plated W-Rh anode wires. The axial cells have 12 anode wires with a radial spacing of 5.3 mm, located between chamber radii of 103 and 162 mm. The stereo cells have 6 anode wires, 5 mm spacing and lie between 188 and 213 mm radii. The stereo angle is $\sim$4°. The anode wires are offset into the cell by a $\pm$41 μm alternating stagger in order to resolve the left-right drift ambiguity. There is an additional anode wire bow of 50–100 μm due to the electrostatic forces when chamber voltages are applied. The cathode planes use 125 μm diameter Cu-Be wires spaced 1 mm apart.

The electrostatic field conditions within a cell are defined by the anode wire surface field, which

determines the gas gain, and the drift field. These fields are determined by the voltages applied to the potential and cathode wires; the anode wires are at ground potential. The drift field is perpendicular to the anode plane. A uniform potential gradient is produced on the cathode plane by a voltage divider network. The potentials of each of the wires in the boundary field shaping rings are also set by resistor networks. Foils at the inner and outer radii of the axial and stereo cell layers operate at fixed potentials and terminate the electrostatic fields.

The high voltage (HV) system includes resistor divider networks mounted on the chamber, an external distribution network, power supplies, and computer controlled ramping and monitoring facilities. It is a modular system with the capability of independently controlling the voltages on 18 separate HV cells for each of the axial and stereo systems. Each HV cell corresponds to 2 readout anode planes.

The setting of the power supply voltages is controlled by individual DACs and monitored by a multiplexed ADC system, both operating within a CAMAC based HV control system. This control system ensures that the complete axial or stereo system can be turned on or off, or adjusted simultaneously using a computer controlled common ramp function. The system also includes synchronous handling of HV trip conditions and provides for several safety interlocks.

Electronics

Both ends of each anode wire are connected at the chamber end-plates to preamplifiers with appropriately matched characteristic impedances of 360 Ω and a gain of 2.5. Electric cross-talk between neighbouring sense wires is compensated by resistive feedback [6,7]. Pole-zero shaping shortens the fall time of the pulses, thus reducing the dead-time between signals to 40–50 ns which corresponds to a two-particle separation of about 2 mm.

Time digitising is performed for both the drift (r-ϕ) and the z coordinates in "converter" modules, where the signals from each wire-end are amplified and fed to a constant fraction discriminator. The drift time measurement is obtained by combining the outputs from the two wire-ends in a mean-timer, which results in the measurement being independent of the position of the hit along the wire. The drift time measurement has an intrinsic bin width of 0.67 ns and a 12-bit range [6,7].

The signals from the two constant fraction discriminators are also passed to a unit which measures the difference in their time of arrival. A measurement of this quantity to a precision of 0.1 ns allows the z coordinate to be determined to ~4 cm.

A more detailed description of this readout electronics system may be found in ref. [7].

Performance

Details of tests with various operating conditions can be found in ref. [6]. During the physics run at LEP in 1989 the chamber was operated at a drift field of 2.5 kV/cm and an anode surface field of 360 kV/cm, using the same gas mixture as the jet chamber. The spatial resolution as a function of drift distance in the r-ϕ plane for the axial cells is shown in fig. 6; the average resolution is 55 μm. Results on the combined performance of the tracking chambers can be found in section 3.5.

3.3 Jet Chamber

Design

The jet chamber is designed to combine good space and double track resolution, essential for the efficient recording of jet-like events, with the possibility of particle identification, within a solid angle close to 4π. The design principle was first established with the jet chamber of the JADE experiment [8] at PETRA. The sensitive volume of the jet chamber is a cylinder with a length of about 4 m, surrounding the beam pipe and vertex detector. The outer diameter is 3.7 m, the inner 0.5 m. The chamber is subdivided into 24 identical sectors, each containing a plane with 159 sense wires. Cathode wire planes form the boundaries between adjacent sectors. All wires are parallel to the beam direction and the wire planes are radial. The maximum drift distance varies from 3 cm at the innermost sense wire to 25 cm at the outermost wire. Many of the design features of the OPAL jet chamber are described in refs. [9,10].

In the range $43° < \theta < 137°$ 159 points are measured along each track, and at least 8 points on a track are obtained over a solid angle of 98% of 4π. For each point true three-dimensional coordinates (r, ϕ, z) are determined from the wire position, the drift time and from a charge division measurement. The charge division method requires the measurement of the integrated charges for each hit at both ends of the signal wire. The ratio of these charges determines z, and their sum is used to calculate the energy loss dE/dx of the particle in the chamber gas.

The signal wires are located between radii of 255 mm and 1835 mm, equally spaced by 10 mm, alternating with potential wires. In order to resolve the left-right ambiguities the signal wires are staggered by ± 100 μm alternately to the left and right side of the plane defined by the potential wires. The signal wires are at ground potential. The voltage of the potential wires determines the gas gain and is normally set to -2.38 kV.

The wires are stretched between two conical end plates which are held apart by a set of 24 hollow aluminium panels located at the outer radius of the chamber. There is no inner support tube.

Fig. 7 shows a perspective view of the mounting scheme of the sense and potential wires at the end plates. The wires run through slots between the field shaping electrodes, situated at the inside of the conical end plates, and then through holes in those plates to the outside. They are precisely positioned at the outside of the end plates with the help of an accurately machined ($\sigma<10$ μm) comblike structure [11]. The method of wire positioning is described in detail in ref. [12].

The cathode planes are inclined in ϕ by 7.5° with respect to the anode planes. Since the equipotential surfaces in the drift region are parallel to the anode plane, each wire of the cathode plane is held at a different potential by a resistor network. At the innermost radius a field cage made of wires and a foil terminate the electrostatic field. At the outermost radius of each sector the correct electrostatic boundary conditions are provided by a field shaping electrode, an insulator covered with copper strips. Also on the end plates similar field shaping electrodes generate the correct field termination. Fig. 7 shows, together with the anode wire support, a cut-away picture of the endcap field shaping electrode, the mounting of the cathode wires, and the resistor chain defining the cathode potentials. More details of the field cage can be found in ref. [10].

The high voltage system [11,13] has to supply voltages from -25 kV at the outer, to -2.5 kV at the inner feed points. In order to avoid non-linearities in the drift field, e.g. caused by leakage currents and by the presence of large ion currents under certain beam conditions, 4 intermediate points are also supplied with high voltage. For adjusting the voltages, a master/slave system has been built where

the master ramps all voltages simultaneously according to the slave settings. All 24 cathode planes are connected to the same power supplies to guarantee the same voltages throughout the chamber. The currents into the resistor chains are monitored separately for each feed point of the cathodes with high accuracy; for example the current of 700 μA per cathode plane drawn at the outer feed point is measured with a resolution of 8 nA.

Under normal operating conditions all potential wires are connected to one power supply. The currents in the chamber are monitored individually per group of 16 wires using current meters similar to those used for the cathodes. The sense wire currents are monitored with a precision of 8 nA again in groups of 16 wires and the values can be used to correct for space charge effects in the dE/dx measurements as described in ref. [14].

To protect the chamber against overcurrents, the current measuring circuits are equipped with comparators. If the current in any of the HV-lines of the cathode exceeds the hard-wired threshold, all power supplies are disconnected and the potential wires are grounded by a fast transistor switch in $\sim$2 μs. An overcurrent in one of the potential wire groups activates only the potential wire protection circuit.

Electronics

Electric cross talk between neighbouring wires can lead, for certain track directions, to a significant deterioration of the chamber resolution. The chamber was therefore built with hardware cross-talk compensation [10], using a resistor network at the output of the preamplifiers. The remaining cross talk signal on the first and second neighbouring wires after compensation amounts to less than 1% of the signal on the primary wire, compared with 8% before compensation.

Fig. 8 shows a schematic drawing of the readout electronics. Low noise preamplifiers are mounted on the end plates close to the points where the anode wires are attached. The waveforms of the amplified signals from each end of every sense wire are recorded with 100 MHz flash analogue-to-digital converters (FADCs). The high speed sampling greatly improves the time measurement and the double hit resolution [15]. The components of the FADC system (DL300) are described in detail elsewhere [16]. The FADCs have a 6-bit resolution, which is effectively extended to 8-bit by a nonlinear response function. Digitised hit data are stored in fast memories.

The digitised information is read out via hardware scanners, which also perform zero suppression. The valid data from all 80 front-end FADC crates are transferred to 20 microprocessors residing in two VME crates for further data reduction. The first step in this reduction is an online pulse shape analysis [17] in which the pulse shape of each hit is used to calculate the corresponding drift time and the signal charge. This information is used in a second step to perform online track finding [18].

Calibration and Monitoring

The chamber is operated with a three-component gas mixture of argon (88.2%), methane (9.8%) and isobutane (2.0%) at a pressure of 4 bar. In order to achieve the desired spatial and charge resolutions, gas properties such as drift velocity and electron attachment must be kept stable over a period of several months in the presence of outgassing materials. The gas system was therefore built as a closed system with recirculation and purification of the gas in order to eliminate oxygen with high efficiency down to a level of a few ppm, since oxygen has a large electron attachment coefficient. With one volume exchange per day the oxygen level reaches values as low as 2 ppm after a few days of purification. The corresponding loss of electrons is <5% for a drift distance of 25 cm. There are indications from several experiments that the presence of a certain amount of water vapour in the chamber gas has beneficial effects on the chamber lifetime [19]. On the other hand small quantities

of water affect the drift velocity [20]. Therefore the jet chamber is operated with a water content of ~500 ppm which is kept constant to ±50 ppm. A small test chamber [20] is used to monitor the drift velocity, gas amplification and electron attachment.

A laser system based on a Nd-Yag laser (wavelength 266 nm, pulse length 3 ns) with 2×24 double beams at fixed positions is used to monitor the drift velocity and to provide calibration constants for the charge division measurements. A dielectric beam splitter generates two parallel beams with a precisely known separation. The chamber is illuminated with each beam in turn using polarised laser light and a Pockels cell. It has been shown [21] that distortions in the electric field or in the mechanical structure can easily be spotted, and that the drift velocity (v_d) can be measured with an accuracy of $\sigma_{v_d}/v_d < 0.1\%$.

Performance

The overall design of the chamber and the optimisation of performance were done with several prototype setups, mainly with the full scale prototype (FSP) [9,14]. The chosen working point of the jet chamber (gas gain $\sim 10^4$, drift field 890 V/cm, pressure 4 bar) represents an optimisation of the competing requirements for good particle identification through dE/dx (low gas gain) and good z resolution through charge division (high gas gain). Preliminary performance figures achieved during the first operation in 1989 are given in the following paragraph.

Fig. 9 shows the spatial resolution in r-ϕ, as a function of the drift distance. The average resolution, $\sigma_{r\phi}$, is 135 μm at the mean drift distance of 7 cm. The average resolution in z, σ_z, is 6 cm. The distribution of inverse momentum, $1/p$, for tracks in events of the type $e^+e^- \rightarrow \mu^+\mu^-$ is shown in fig. 10, and indicates that the resolution, σ_p/p^2, is 2.2×10^{-3} GeV^{-1}. In fig. 11a the energy loss dE/dx is plotted as a function of momentum for tracks in a sample of multihadron events and events of the type $e^+e^- \rightarrow \mu^+\mu^-$. Demanding at least 130 measurements per track a truncated mean is calculated providing a resolution, $\sigma_{(dE/dx)}/(dE/dx)$, of 3.8% for the dimuon sample. Fig. 11b shows the distribution of the truncated means for these dimuon events. Results on the combined performance of the tracking chambers can be found in section 3.5.

3.4 Z-Chambers

Design

The z-chambers are arranged to form a barrel layer around the jet chamber covering the polar angle from 44° to 136° and 94% of the azimuthal angle. They are designed to make precise measurements of the z coordinates of charged particles as these leave the jet chamber and thus to improve both the polar angle and invariant mass resolutions.

They consist of 24 drift chambers, 4 m long, 50 cm wide and 59 mm thick. Details of their construction and performance are described elsewhere [22]. Each chamber is divided in z into 8 bidirectional cells of 50 cm × 50 cm, so that the maximum drift distance is about 25 cm in the z direction. The chambers use the same gas as the jet chamber and require a maximum drift voltage of about 20 kV to achieve a drift field of 800 V/cm. Each cell (see fig. 12) has six anode wires (about 50 cm long in the ϕ direction) at increasing radii with 4 mm spacing and a stagger of ±250 μm to resolve the left-right ambiguity. The wires have an amplifier at each end, so that the ϕ coordinate may be determined by charge division. A grid isolates the anode region from the drift region and results in a very linear response in the drift region up to the grid and also allows stable chamber operation over a wide range of gas gains and pressures [22].

Electronics

The differential output signals are multiplexed two to one [23], in a fashion that minimises the confusion within jets, and are digitised by a FADC system [24], which is read out using VME microprocessors. The z-chambers are controlled in stand-alone mode by a dedicated micro-VAX-II.

The high voltage system uses controllers, equipped with 7 kV modules for the grid and guard high voltages, and interfaces to 30 kV supplies for the drift voltages [25]. All the high voltages are filtered as they enter the pressure vessel, and there are further filters on the lines at the point where they are attached to the wires; this last filtering was added to reduce cross-talk between adjacent anode wires.

Performance

Experience with prototypes and with the final chambers shows that the chosen design results in a very uniform electrostatic field, which allows the ionisation electrons to drift in the narrow 29 mm wide drift gap for the full 25 cm drift distance with high efficiency. Furthermore, the chamber performance is unaffected by small misalignments between the axis of the drift field and the external magnetic field. The intrinsic z resolution, for minimum ionising particles normal to the drift direction, varies from less than 100 μm at the shortest drift distances, to 200 μm at the longest drift distances (see fig. 13). The absolute resolution is determined by the precision of the survey, and is expected to be around 300 μm. The r-ϕ resolution was measured to be of the order of 1.5 cm.

3.5 Combined Performance

Fig. 14 illustrates the accuracy of the measurement of the primary vertex in the 1989 physics run using all three subdetectors of the central tracking system. Whereas in the vertical direction the width of the distribution is dominated by the detector resolution, a clear broadening in the horizontal direction is seen corresponding to the larger beam dimension in this plane. The impact parameter resolution measured with events of the type $e^+e^- \rightarrow \mu^+\mu^-$ is shown in fig. 15. In the r-ϕ plane the r.m.s. resolution is found to be 75 μm and in the r-z plane it is 2 mm with and 2.7 cm without the stereo wire information of the vertex detector. The invariant mass resolution, σ_{K^0}, for $K^0 \rightarrow \pi^+\pi^-$ decays is 8 MeV as shown in fig. 16.

4 Time-of-Flight System

The time-of-flight (TOF) system covers the barrel region $|\cos\theta|<0.82$. It generates trigger signals and, by measuring the time of flight from the interaction region, allows charged particle identification in the range 0.6–2.5 GeV. It also aids in the rejection of cosmic rays.

Design

The TOF system consists of 160 scintillation counters [26] forming a barrel of mean radius 2.360 m which is positioned outside and coaxial with the aluminium coil. Each counter is 6.840 m long and has a trapezoidal cross section (45 mm thick, 89 to 91 mm wide). The counters are individually wrapped in aluminised mylar foil and black PVC sheet. The maximum gap between adjacent counters is 2.6 mm.

The light is collected at both ends of each counter via 300 mm long conical and cylindrical plexiglass light guides glued directly to phototubes [27]. The phototubes have a nominal gain of 3×10^7 at

1850 V, and are carefully shielded from stray magnetic fields by a combination of μ-metal, soft iron and compensating coils.

Electronics and Monitoring

Each of the 320 analogue phototube signals is passively split into two. One signal (one third of the amplitude) goes to a 12-bit charge integrating ADC. The other signal (two thirds of the amplitude) goes to a constant fraction discriminator with three outputs, which go to a strobed pattern unit, an 11-bit (50 ps/count) TDC, and a mean timer. Trigger signals from the TOF system are generated from the mean timers, and require the discriminators on both ends of a counter to have fired (within 50 ns of each other and within 50 ns of the arrival time of a relativistic particle from beam interactions).

A laser calibration system will monitor the response of the counters and associated electronics to light pulses which simulate the effect of the passage of charged particles through the scintillator. The ultra-violet light from a pulsed nitrogen laser is wavelength-converted and diffused by a small piece of scintillator before being fed to each end of each counter via an optical fibre and a plexiglass prism glued to the conical light guides.

Performance

The response of each counter of the TOF system was measured in a 5 GeV test beam at the CERN-PS. Signal times and amplitudes were measured at both ends for 11 different longitudinal positions of the beam through each counter. Along the counters the mean speed of scintillation light was found to be 0.582 c, and its mean attenuation length 2.33 m. From the width of the time distribution obtained for each measurement, the timing resolution of the TOF is expected to be 280 ps at the centre of the counters and 350 ps at the ends (not using any z measurement coming from any other detector) and its z resolution is expected to be 5.5 cm. If in addition a z measurement from another detector is used, then the resolution at the centre should be unchanged but the resolution at the ends should improve to 220 ps.

The timing resolution which is currently achieved in situ at LEP has been measured with events of the type $e^+e^- \rightarrow \mu^+\mu^-$. The comparison of the z measurement from the TOF system with the z measurement of the barrel lead glass calorimeter indicates a z resolution of 7.5 cm. The measured flight time for muons compared to their expected flight time has a resolution of 460 ps (without using external z information). These two distributions are shown in fig. 17.

5 Electromagnetic Calorimeter

5.1 General Concept

The electromagnetic calorimeter detects and measures the energies and positions of electrons, positrons and photons ranging from tens of MeV to 100 GeV. It provides π^0-photon discrimination and, in conjunction with the central tracking system, electron-hadron discrimination. It is a total absorption calorimeter, and is mounted between the coil and the iron yoke of the magnet as shown in figs. 1 and 2. It consists of three large overlapping assemblies of lead glass blocks (the barrel which surrounds the magnet coil, and two endcaps) together covering 98% of the solid angle. It is complemented by the gamma catcher and the calorimeter of the forward detector, and is thereby hermetic down to the inner radius of the forward calorimeter. Lead glass was chosen for the electromagnetic calorimeter because of its excellent intrinsic energy resolution ($\sigma_E/E \sim 5\%/\sqrt{E}$, where E is the electromagnetic energy in

GeV), linearity, spatial resolution (~1 cm), granularity, electron-hadron discrimination, hermeticity and gain stability.

Since there are ~2 X_0 of material in front of the lead glass, due mostly to the coil and pressure vessel, most electromagnetic showers are initiated before the lead glass itself. Presampling devices are therefore installed in both the barrel and endcap regions immediately in front of the lead glass, to measure the position and sample the energy of these electromagnetic showers, thereby improving the π^0-photon and electron-hadron discrimination and the electromagnetic energy resolution. In the barrel region the presampler consists of a cylinder of tubes operated in the limited streamer mode, while the endcap presampler is an umbrella type arrangement of thin multiwire chambers operating in a high gain mode. A presampler is able to improve the electromagnetic energy resolution on a shower by shower basis because the pulse height (or number of hits) observed is approximately proportional to the number of (charged) shower particles entering the device, which is itself roughly proportional to the energy deposited in the material in front of the presampler. In the barrel region, the time-of-flight system can provide additional presampling information from the observed pulse-heights.

The properties of the electromagnetic calorimeter are summarised in table 3. Fig. 18 shows the typical total number of radiation lengths of material a) in front of and b) inside the active material of the electromagnetic calorimeter.

5.2 Barrel Electromagnetic Presampler

Design

The barrel electromagnetic presampler [28,29] consists of a cylinder of limited streamer mode chambers located between the time-of-flight system and the barrel lead glass calorimeter. The structure of the presampler is shown in fig. 19. It consists of 16 chambers covering the surface of a cylinder of radius 2388 mm and 6623 mm length. Each chamber has two layers of limited streamer mode tubes with the wires running axially. The tubes are similar in design, but not identical, to those pioneered by Battistoni [30].

Each layer of a chamber is made from four PVC extrusions, each having 24 cells. The layers are offset by half a cell width to avoid inefficiencies associated with the cell walls. The cells have an internal size of 9.6 mm square, with 1 mm thick walls. The cell walls are sprayed with a high resistance graphite suspension [31] and buffed to form a hard smooth coating of surface resistivity ~1 MΩ/square. The cells are closed with a similarly coated flat PVC cover. The anode wires are stainless steel, 75 μm in diameter, and are supported in the cells by a plastic bridge every 50 cm. The chambers are operated with a gas mixture of n-pentane (32%) and CO_2 (68%), obtained by bubbling CO_2 through a tank of n-pentane maintained at a constant temperature.

Readout of the chambers is obtained from 1 cm wide cathode strips located on both sides of each layer of tubes, and oriented at 45° to the wire direction (see fig. 19). The strips on opposite sides of a layer are orthogonal. In addition, the charge collected on each wire is measured at both ends to allow position measurement along the wire by charge division. To facilitate this measurement the wires are operated at ground potential and the resistive cathodes at high voltage. To obtain good noise isolation a pair of ground planes is located on either side of each layer just outside the cathode strips. The relative accuracy in strip position is 1 mm over the length of each chamber. The chambers are read out independently. To limit the number of readout channels, signals from corresponding strips in the two layers are passively added.

The high voltage is supplied individually to each of the 8 extrusions of a chamber. Commercial high voltage supplies [32] are used for the 128 channels of the system. Typical quiescent currents for single channels are under 100 nA.

Electronics

Each chamber requires the readout at each end of 480 strip signals and 192 wire signals for a detector total of 21,504 channels. A system of charge sensitive amplifiers and multiplexers is located at each end of the chambers.

The front-end electronics is built around an 8-channel charge sensitive hybrid circuit [33] and a second hybrid which is a combination summing amplifier and line driver. The latter serves 32 channels. The circuit boards are mounted in a copper cage which provides both thermal and electrical noise isolation.

At the digitising electronics, each signal appears on two outputs, one at normal gain and a second at 8 times the amplitude. Two special VME readout modules are used. One is a digitiser module having a pair of 12-bit ADCs, one for the high- and one for the low-gain measurement. This module performs 21:1 multiplexing of its input signals. The pedestals, gains, and polarities of all channels are equalised prior to digitisation using data previously downloaded to the module. The other is a sequencer module which controls the multiplexing both in the front-end electronics and in the digitisers. It also controls the block transfer of data from the digitiser to a memory module in the same crate. From there, a VME processor performs zero suppression and clustering.

Performance

The performance has been determined by measurements of a complete chamber in a test beam, using both electrons and charged pions over a range of momenta and radiator thicknesses. Results on the spatial resolution are given below, while results on the energy resolution of the combined barrel presampler and lead glass calorimeter are given in section 5.6.

The spatial resolution based on the cathode strips is shown in fig. 20 for both single charged particles and for electromagnetic showers after 2.1 X_0 of material. The intrinsic resolution for single charged particles, unscattered by material, varies from 1 to 2 mm depending on the angle of incidence of the track and on whether one is considering the direction along a wire or transverse to a wire. The resolution for the position of electromagnetic showers, in the plane perpendicular to the shower direction, varies from about 6 to 4 mm as the energy changes from 6 to 50 GeV. This corresponds to an angular resolution for photon trajectories of $\sim$2 mrad.

The resolution in z from current division is $\sim$10 cm for a single charged particle. This measurement, together with the pulse height correlation with the strips, aids significantly in the removal of ambiguities during data analysis.

5.3 Barrel Lead Glass Calorimeter

Design

The barrel lead glass calorimeter, shown schematically in fig. 2, consists of a cylindrical array of 9,440 lead glass blocks of 24.6 X_0, located at a radius of 2455 mm, outside the magnet coil, covering the full azimuthal angle and $|\cos\theta|<0.82$. The calorimeter is instrumented with magnetic field tolerant phototubes.

The longitudinal axes of the lead glass blocks point towards the interaction region to minimise the probability of a particle traversing more than one block. However the blocks are tilted slightly from a perfectly pointing geometry to prevent neutral particles from escaping through the gaps between the blocks. In the z direction, the calorimeter is segmented into 59 blocks and the gaps are pointing to different z positions ($|z|= 55.5-157.9$ mm) along the beam line depending on the position of the block. In the ϕ direction, the calorimeter is segmented equally into 160 blocks, each covering 2.25° in azimuth, and each tilted by 0.574° in such a way that the gaps point away from the beam axis by 30 mm. To achieve such a quasi-pointing geometry, blocks of 16 different shapes are used. Mechanically, the calorimeter is divided into 10 half-ring structures. Each half-ring contains 80 identical ϕ-segment modules of 12 lead glass counters (11 for the middle ring).

To achieve good energy resolution at high energies it is vital to minimise shower leakage from the back of the calorimeter. In order to maximise the effective counter thickness in radiation lengths in a limited space, a newly developed heavy glass, SF57 [34], was adopted. Each lead glass block is $\sim 10 \times \sim 10$ cm^2 in cross section and 37 cm in depth (21.6 X_0). The assembly of a block with light-guide, phototube and fibre optic connector is shown in fig. 21. All surfaces of each lead glass block are polished. For optical isolation each block is wrapped with a black sheet of vinyl fluoride laminated on each side with a polyester film. The inner surface of the sheet is coated with aluminium for efficient reflection of light. The thickness of the wrapping amounts to 70 μm. The Čerenkov light produced by relativistic charged particles in the blocks is viewed by a newly developed phototube [35] of 3 inches diameter which is insensitive to small magnetic fields.

Between each phototube and lead glass block is a 4 or 6 cm long light guide made of SF57. They are coupled together by an optical glue [36]. A 2 mm thick cylindrical tube of Permaloy metal [37] surrounds each phototube to reduce the effect of the stray field of the magnet. With this shielding, the phototube can be operated in an external field of up to 100 G with a gain deviation of less than 1%.

Each phototube has an independent high voltage channel [38] which can be controlled in 2 V steps. The stability of the applied high voltage was measured to be better than 0.1 V over a week, corresponding to less than 0.08% change of phototube gain.

The signals from the phototubes are digitised by charge integrating FASTBUS ADCs [39]. One ADC module contains 96 input channels with a quasi-differential input mode. Each channel has two sensitivities, 30 fC/count and 225 fC/count, and their full scales correspond to 120 pC and 900 pC, respectively. These two sensitivities assure a high-precision measurement over a wide energy range. The non-linearity of the ADC was measured to be less than ± 1 count over the full range of the low sensitivity channel.

Calibration and Monitoring

In order to calibrate the gains of the lead glass counters, each counter was exposed both in 1987 and in 1988 to 50 GeV electrons in a CERN-SPS beam [40]. A special handling device was developed [41] which supported the 30 ton half-ring and oriented each lead glass block into the beam line in turn. The phototube gains were adjusted by changing the applied high voltage in such a way that a 50 GeV electron should correspond to a charge of 500 pC. The accuracy of the gain measurement was typically 0.1%. The non-linearity of the counters was measured to be less than 1% in the energy range of electrons from 6 to 70 GeV.

A gain monitoring system of high quality is indispensable to maintain the accuracy of the energy calibration over a long period. An optical monitoring system using a xenon flash lamp [42] was adopted. The spectrum of light from the xenon lamp is similar to that of Čerenkov light in lead

glass when the light attenuation in lead glass and the quantum efficiency of a photocathode are taken into account. For each half-ring, the xenon light is distributed to 80 ϕ-segment modules through optical fibre bundles [43] and at each module it is further distributed to the individual counters via an optical fibre cable connected at one corner of each lead glass support flange (see fig. 21). A 1 mm thick white-painted aluminium plate is attached to the front surface of each lead glass block to reflect the monitoring light efficiently and to distribute the light uniformly on the cathode surface of the phototube. The xenon flash lamp is operated at a repetition rate of 10 Hz by external triggers. The light pulse with about 150 ns FWHM produces a phototube signal of 20–30 GeV electron equivalent. The light output of the flash lamp is monitored by a PIN photodiode [44]. The pulse to pulse fluctuation of the intensity observed by the PIN diode is 0.4–0.5% r.m.s..

The calibration with the electron beam was repeated within 1 to 2 days for most of the half-rings to confirm the reliability of the calibration and to check the short term stability of the counter response. A stability of 0.2% r.m.s. was obtained after correction by the xenon monitoring system. The long term drift in response was also studied using the electron beam over a time interval of about one year. A typical increase in response of ~2% with 1.5% r.m.s. spread was observed. The xenon monitoring system tracked the gain drift and the spread was reduced to 0.9% after the correction.

Results on the energy resolution of the barrel lead glass calorimeter, in particular with and without additional material in front and the presampler to correct for this, are given in section 5.6.

5.4 Endcap Electromagnetic Presampler

Design

Each endcap electromagnetic presampler [45] is an umbrella shaped arrangement of 32 chambers in 16 wedges (sectors) located between the pressure bell of the central tracking system and the endcap electromagnetic calorimeter, covering the full azimuthal angle and $0.83<|\cos\theta|<0.95$. The physical structure of the presampler is shown schematically in fig. 22.

Thin multiwire chambers operating in a high gain mode are ideally suited to match the constraints imposed by the requirements of good energy and position resolution and by the severe space restrictions in the endcap regions. The same chamber design as for the hadron pole tip calorimeter (see section 6.2.2 for further details) with modified geometry and readout is used; the chamber size is optimised to the available space between the pressure bell and the endcap lead glass detector. At the outer radius acceptance coverage is guaranteed for showers which traverse at least half of the thickness of an endcap lead glass block. Geometrical constraints prevent coverage of the regions at the inner radius, where the total material thickness in front of the calorimeter exceeds 4 X_0 and varies so rapidly with position that the usefulness of a presampler correction would be limited.

Each sector has one large and one small trapezoidal chamber, the large one being inclined by 18° with respect to the plane perpendicular to the beam in order to follow the shape of the pressure bell and the lead glass. The small chamber is at 90° to the beam axis. Neighbouring sectors overlap each other to ensure complete coverage of the endcap region.

Space coordinates are provided, for showers and for minimum ionising particles, by the simultaneous readout of groups of 4 wires and strips. The energy correction for showers is best obtained using the pad readout, because the summation over fewer electronic channels improves the signal to noise ratio. The pad readout also provides a reduction of ambiguities present on wires and strips to aid offline cluster finding. All 6,080 channels have analogue readout using 24 × 32 fold multiplexing

electronics.

Performance

The performance has been determined by measurements of a production sector in a test beam, using both electrons and charged pions over a range of momenta and radiator thicknesses. Results on the spatial resolution are in good agreement with the intrinsic chamber resolution, namely $1/\sqrt{12}$ of the effective wire or strip pitch. Results on the electron-hadron discrimination of the combined endcap presampler and lead glass calorimeter are given in section 5.6.

5.5 Endcap Electromagnetic Calorimeter

Design

The endcap electromagnetic calorimeter [46,47] consists of two dome-shaped arrays, each of 1,132 lead glass blocks, located between the pressure bell of the central tracking system and the pole tip hadron calorimeter, covering the full azimuthal angle and $0.81<|\cos\theta|<0.98$. It is shown schematically in figs. 2 and 22. It differs from the barrel lead glass calorimeter in two important aspects: the lead glass blocks are mounted with their axes coaxial with the beam line, because of tight geometrical constraints, and it is instrumented with novel devices, single stage multipliers known as vacuum photo triodes (VPTs) [48], which were developed in conjunction with industry to be able to operate in the full axial field of the magnet.

Fig. 23 is a schematic view of a lead glass block assembly. The lead glass used is CEREN-25 [49]. The surfaces of the blocks are polished, and each block is housed in a brass can of wall thickness 0.45 mm. This acts as a vital electrical screen, and provides mechanical support for the assembly via the end plate of the can which is secured to a rigid back plate. For efficient reflection of light, each block is wrapped with aluminium foil, at ground potential, and is enclosed in a protective layer of mylar. The front faces of the blocks are arranged to follow the contours of the pressure bell of the central tracking system (see fig. 22). The blocks were manufactured in three lengths (380, 420 and 520 mm), and arranged over the endcap to give a total depth of at least 20.5 $X_\circ$ (typically 22 $X_\circ$) for all particles emerging from the interaction region.

Prototype triode devices from several manufacturers were studied [50]. The tubes finally selected [51,52] have an average internal gain of 12.3 (at a field of ~0.4 T) and an average quantum efficiency of 26% [46]. The photocathode sensitivity as a function of wavelength is well matched to the spectrum of Čerenkov light transmitted by the lead glass. The triodes are optically coupled to the lead glass by an epoxy resin [53], selected for optical transparency and high refractive index. Significant additional amplification is required close to the VPTs, and a high gain, low noise, amplifier has been specially developed for this application [54].

A pulse transformer and resistive attenuation network located near the ADCs provide matching between the screened twisted pair cable from the amplifier and the 50 Ω coaxial cable feeding the input of the charge integrating FASTBUS ADCs [39]. It also provides additional noise immunity, and allows the assembly inputs into the ADCs to be equalised for triggering. Careful ripple filtering of the high voltage supply is important, and is achieved via a two stage low pass filter. All VPTs are operated at a photocathode potential of −1.0 kV.

The mean number of photoelectrons produced by an electromagnetically showering particle is found to be 1.8×10^3 per GeV [46]. The overall noise (dominated by amplifier noise, but including pick-up

and ADC noise) of a single channel, expressed in units of equivalent energy, is typically 14 MeV (at a field of ~0.4 T).

Calibration and Monitoring

As seen in fig. 23 each assembly has two reference light sources which are used for monitoring its performance. In one system, light is taken via optical fibres to each assembly from a liquid scintillator cell which is excited by a pulsed ultra-violet nitrogen laser. A fibre optic connector joins an external fibre from the cell to an internal fibre which injects the scintillation light into the lead glass. In addition, each assembly has a green light emitting diode (LED). The LED is mounted on a perspex rod which is glued to the end of the lead glass block. This arrangement avoids the electrical driving pulse passing near the very sensitive amplifier. With the laser driven system all assemblies must be pulsed together, while the LED system allows an individual assembly or any subset of assemblies to be selected. The laser and LED systems produce pulses of, respectively, ~10 and ~20 GeV electron equivalent.

Each assembly was calibrated several times in a high energy electron beam at the CERN-SPS [40]. Most assemblies showed excellent stability. The short term (1-2 day) stability of the response was 0.3% r.m.s., and the stability observed over a 7 month period was 1.3% r.m.s. with a 0.2% shift in the mean.

The performance of the endcap electromagnetic calorimeter has been extensively studied in π^- and e^- beams [46,47]. The energy response was found to be linear in the range 3–50 GeV to within the measurement errors of ~1% and the energy resolution was $\sigma_E/E \sim 5\%/\sqrt{E}$ at low energies. The spatial resolution was found to be 8–14 mm for a 6 GeV e^- beam incident at 15° to the longitudinal block axes. Results on the electron-hadron discrimination of the endcap lead glass calorimeter are given in the following section.

5.6 Performance of Combined Presampler and Lead Glass System

Many test beam studies have been undertaken [45,46,47,48,52] to understand how best to combine the information from the presampler and lead glass, and to understand the anticipated performance of the combined system in the experiment. For example, fig. 24 shows the measured energy resolution as a function of incident e^- energy for a prototype barrel section of the calorimeter. The typical energy resolution without any material in front was found to be $\sigma_E/E = 0.2\% + 6.3\%/\sqrt{E}$, as indicated by the solid line in the figure. It can be seen that adding 2.08 X_0 of aluminium in front degrades the energy resolution substantially, e.g. by a factor ~2 at 6 GeV, but that ~50% of this degradation can be recovered by using the information from the presampler chambers.

Fig. 25 shows the measured π^- misidentification probability as a function of e^- detection efficiency for isolated 20 GeV particles incident into 1.6 X_0 of aluminium in front of a production endcap section of the calorimeter. By exploiting the correlated response of the presampler and lead glass, a pion rejection in the order of 10^{-3} is achieved for an electron identification efficiency of 80–90%. The charged particle identification capability of the jet chamber via its dE/dx measurements which is discussed in section 3.3.4 significantly enhances the electron-hadron discrimination power of the entire detector.

6 Hadron Calorimeter and Muon Detector

6.1 General Concept

The hadron calorimeter measures the energy of hadrons emerging from the electromagnetic calorimeter and assists in the identification of muons. The iron of the return yoke provides 4 or more interaction lengths of absorber over a solid angle of 97% of 4π. The yoke is segmented into layers, with planes of detectors between each layer, and forms a cylindrical sampling calorimeter about 1 metre thick. The energy resolution is limited mostly by the material of the electromagnetic calorimeter, and by the structure of the return yoke itself. To achieve the coverage in solid angle, the hadron calorimeter is constructed in three parts—the barrel, the endcaps and the pole tips, as shown in fig. 3. The main properties are summarised in table 4.

The muon detector, see table 5, is constructed as a barrel and two endcaps and covers the iron yoke almost completely. While muons penetrate to the muon detector and leave a single clean track, most hadrons are absorbed in the yoke. The barrel muon detector consists of planar drift chambers whereas both the hadron calorimeter and the muon endcap detectors use plastic limited streamer tubes. However, their construction details differ because the mechanical and safety constraints and the physics requirements are different.

6.2 Hadron Calorimeter

6.2.1 Barrel and Endcap Hadron Calorimeter

The barrel consists of 9 layers of chambers, alternating with 8 iron slabs, and spans radii from 3.39 m to 4.39 m. The slabs are 100 mm thick with 25 mm gaps. It is closed at each end by a doughnut-shaped endcap, where 8 layers of chambers alternate with 7 slabs of iron. Here the slabs are 100 mm thick with 35 mm gaps. Since there is a high probability of hadronic interactions being initiated in the 2.2 interaction lengths of material before the hadron calorimeter, the overall hadronic energy has to be determined by combining signals from the electromagnetic and hadron calorimeters. The chosen sampling thickness of 100 mm gives an approximate match between the uncertainties in hadronic energy measurements by these two calorimeters.

The active elements of the detector layers are based on the limited steamer tube design developed at INFN Frascati [30,55,56,57]. A low cost, 'comb like', PVC extrusion was used with 7 or 8 cells, as shown in fig. 26, with 100 μm diameter anode wires, 10 mm apart, and an extruded PVC gas envelope. The inside surface of each cathode cell is coated with graphite and a stabiliser [58,59] giving a surface resistance in the range 0.1 to 5 MΩ/square. Refs. [30,55,56,57,60,61,62] give further details of the design, construction and testing of the chambers. Signals are read out through both upper and lower faces of the chambers, but the signals from the wires themselves are used only for monitoring purposes. On one side (outer radius), they are induced through the cell wall and gas envelope onto large area (typically 500 mm $\times$ 500 mm) pads. On the other side, where there is no cathode wall, they are induced through the gas envelope onto 4 mm wide aluminium strips which run the full length of each cell and are centred over the wires. In the barrel the wires are parallel to the beam and in the endcap they are horizontal (see fig. 27). The calorimeter contains in total 2,400 m^2 of detector. The 57,000 strips are exploited for precise single particle tracking for muon identification and for shower profile mapping. Layers of pads are grouped together to form towers, which divide the solid angle into 976 equal elements radiating from the interaction region. There are 48 bins of 7.5° in ϕ and 21 bins in

θ. Unit gain analogue summing amplifiers mounted near the chambers sum the signals from the 8 or 9 pads in each tower and provide an estimate of the energy of hadronic showers. A typical hadronic shower initiated by a normally incident 10 GeV pion produces about 25 strip hits and generates a charge of about 600 pC.

Fig. 27 shows the configuration of the chambers. As the width of a wedge varies with radius, an appropriate mix of 7 and 8 cell chambers was used to optimise the coverage. Layers 2 through 8 consist of half-length chambers, about 5 m long, with a junction near the detector equator (θ=90°). This junction is staggered from layer to layer. The width at the ends of these layers is obstructed by the iron of the magnetic return yoke. Layers 1 and 9 are shorter, and are constructed from single chambers, each about 7.3 m long.

The endcap consists of units of 36 chambers (each with 8 wires) and each unit covers a quarter of a layer. The innermost layer has a reduced radial coverage compared with layers 2 to 8.

A mixture of isobutane(75%) and argon(25%) is flushed through the chambers; the total volume of 22 m^3 is changed once per day. Small monitoring chambers are used to sample the output of the gas mixer and to measure variations in gain, due, for instance, to changes in atmospheric pressure. The chambers are operated in limited streamer mode with the anode wires at a voltage between 4.65 kV and 4.85 kV, depending on the atmospheric pressure, so as to maintain approximately constant gain. The voltage can be adjusted individually for groups of typically 6 chambers (48 wires). The current supplied to each group of $\sim$ 48 chambers (the even or odd layers at one end of a wedge) is limited to 3 μA, and is typically a few hundred nA.

Strip signals above a remotely adjustable threshold of typically 3 mV are latched into 72 locally mounted shift registers, which are read out sequentially with zero suppression. The signals from the towers are integrated for 2.5 μs and digitised twice with 12-bit ADCs (which are offset in gain by a factor of about eight). Also, 92 analogue trigger pulses are formed by summing the signals from sets of 16 towers (which form 4 $\times$ 4 arrays). The mean noise level from the 4 $\times$ 4 arrays corresponds to an energy of about 300 MeV, roughly equivalent to the effective energy per single hit. The charge from the innermost pad of each tower is recorded separately, and this information assists in the interpretation of anomalously high signals in the electromagnetic calorimeter caused by charge exchange interactions of hadrons near the back of the lead glass blocks. A monitoring system enables test pulses to be injected on each wire, and the recording of singles rates, voltages and currents.

Several prototype modules were tested in pion beams [63]. Fig. 28 shows the average response of a 3 $\times$ 3 tower module to single pions as a function of energy for three angles of incidence. The response, at fixed angle, was found to be linear with energy and the energy resolution was $\sigma_E/E = 120\%/\sqrt{E}$ (E in GeV) at an incident energy of 10 GeV. Also shown in fig. 28 are the predictions of a Monte Carlo shower simulation which incorporates a parametrisation of the angular dependence of the charge per layer induced by a single particle. This was obtained by studying muons in the test beam and cosmic rays traversing the barrel modules. In a hadron shower, the increase with angle in the response per layer for each single particle is partially counterbalanced by the effective increase in the depth of iron between samples.

The total number of strip hits in a hadron shower is a linear function of the incident hadronic energy, provided that the number of particles traversing each hit cell is close to one, as is the case for energies less than 10 GeV. At higher energies, the long strips in the barrel, which run the whole length of each chamber, experience a slight saturation.

For identifying muon tracks, the important parameters are the positional accuracy (limited by the 10 mm wire spacing) and the efficiency and hit multiplicity for single minimum ionising particles.

There is a geometrical inefficiency of about 10% due to the cell and chamber walls. Other inefficiencies and cross-talk (which causes spurious multiple hits) depend on the operating conditions. For the 3×3 tower prototype, fig. 29 shows the relative tracking efficiency for normally incident 5 GeV muons as a function of the number of layers required to register a cluster of 5 or less strip hits. This is compared with the relative efficiency for finding fake muons in a 6 GeV hadron sample.

6.2.2 Pole Tip Hadron Calorimeter

The pole tip hadron calorimeter complements the barrel and endcap ones by extending the solid angle coverage from $|\cos\theta|$=0.91 to 0.99. Here the gap between the iron plates, available for detectors, was reduced to 10 mm to avoid perturbing the magnetic field. In order to improve the energy resolution in the forward direction, where the momentum resolution of the central detector is falling off, the distance between samplings was reduced to 80 mm and the number of samplings increased to 10 (compared to 9 in the barrel and 8 in the endcap).

Support structures between the iron slabs are inevitable but are located in an alternating way around the 45° lines. This arrangement enables the full solid angle to be covered, but with a slightly deteriorated response (half the number of samplings) in 10% of the area of the calorimeter.

The active elements of the detector consist of thin (7 mm overall thickness) multiwire chambers operating in a high gain mode, similar in construction to those of the electromagnetic endcap presampler described in section 5.4. Fig. 30a shows a cross sectional view of a chamber. More details can be found in refs. [64,65,66,67]. The anode plane consists of 50 μm diameter wires with a spacing of 2 mm and the gas gap between the cathode planes is 3.2 mm. The chambers operate with a voltage of 3.5 kV on the wires and a gas mixture of CO_2 (55%) and n-pentane (45%).

As seen in fig. 30b, each chamber has cathode pads on one side and strips on the other. The pad size, typically 500 cm^2, matches the width expected for a hadronic shower and changes from one layer to another so that corresponding pads from the 10 layers form a tower pointing to the interaction region. There are two sizes of chamber, with areas of 0.61 and 0.47 m^2, having 13 and 8 pads, and 32 and 28 strips respectively. The strips fan out radially almost perpendicular to the anode wires. The dead area, due to frames, gas lines and wire supports, amounts to 12% of the area of each layer. The alternating structure ensures that most of this (10%) is covered by chambers in the other layers. The wires are not read out directly. ADCs record the summed pulse height for each tower and the strips are recorded digitally.

One eighth of a pole tip calorimeter module was tested at CERN in a 6–50 GeV hadron beam. With no material in front, the energy response was consistent with being linear and the resolution, σ_E/E, was $100\%/\sqrt{E}$ for energies below ~15 GeV. At higher energies it deteriorated to $120\%/\sqrt{E}$ due to leakage. Another test also included the electromagnetic calorimeter. Fig. 31a shows the distribution of energy recorded in the two calorimeters for a 10 GeV beam which contained hadrons, muons and electrons. Clear electron and muon signals can be seen, and the typical sharing of energy by hadrons is illustrated. A good estimate of the energy of a hadron is given by the weighted sum, $E_{HCAL}+R\times E_{ECAL}$, where E_{HCAL} (E_{ECAL}) is the energy recorded in the hadron (electromagnetic) calorimeter, assuming the particle is a hadron (electron). R is the e/π ratio, the relative response of the electromagnetic calorimeter to electrons and pions, and was found to be ~3 at 6 GeV and ~2 above 20 GeV. With this parametrisation, the combined energy response is consistent with being linear and the distribution at each energy is well described by a Gaussian, as illustrated in fig. 31b for an energy of 10 GeV. The energy resolution, of the combined detector, varies from $100\%/\sqrt{E}$ for

energies below 15 GeV to $140\%/\sqrt{E}$ at 50 GeV. Tests also showed negligible change in performance for incident angles up to 25°.

6.3 Muon Detector

This detector is designed to identify muons, in particular in the presence of a background of hadrons. Of the full solid angle, 93% is covered by at least one layer of detector—there are gaps, inevitably, due to the beam pipe (2×0.8%), the support legs (2×2.2%), and cables (2×0.6%). Over nearly all of this solid angle the amount of material that a particle has to traverse exceeds 1.3 m of iron equivalent (over 7 interaction lengths for pions), see fig. 32. This is required to reduce the probability of a pion not interacting to less than 0.001. Three processes can be identified by which a hadron can fake a muon: sneakthrough, i.e. failure to interact strongly; punchthrough, in which the hadron interacts but secondary particles emerge and fake a muon; and decay in flight of pions and kaons to muons. Decay is important at low momenta and punchthrough at high momenta. Particles with less than about 2 GeV momentum are stopped in the absorber; muons above about 3 GeV emerge from the absorber. Some of the stopping muons may be identified in the hadron calorimeter. Some of the kaon and pion decays may be identified as kinks or mismatches in the central jet chamber.

The barrel part of the detector covers $|\cos\theta|<0.68$ for four layers and $|\cos\theta|<0.72$ for one or more layers, while the endcap part of the detector covers the range from 0.67 to 0.98 in $|\cos\theta|$, for a geometrical acceptance of greater than 50% (see fig. 33).

Muon identification relies on extrapolating the track seen in the central tracking system through the absorber, allowing for energy loss and multiple coulomb scattering, and looking for a track in the muon detector which matches in position and angle in two views. The positional and angular accuracies required for the track measurement are determined by the multiple scattering of the highest energy muons of interest and are about 2 mm and 3 mrad respectively. The design calls for emerging particles, where possible, to pass through a minimum of four layers of detector.

Ignoring the complexities of hadrons in jets, the efficiency for detecting isolated muons above 3 GeV and within the 93% solid angle is essentially 100%. The probability that an isolated pion of 5 GeV is misidentified as a muon is less than 1% .

6.3.1 Barrel Muon Detector

The barrel part of the muon detector consists of 110 large area drift chambers. The chambers have been developed from those used at JADE [69], and further details of the design will be presented elsewhere [70]. Each chamber is 1.2 m wide and 90 mm deep (this includes the integral support frame). As seen in fig.1, 44 chambers are mounted on each side of the barrel, 10 in the top module and 12 in the bottom module. The construction and cross section of the chambers are identical except for the different lengths of 10.4, 8.4 and 6.0 m. The shorter lengths were required to fit the chambers between the magnet support legs.

The chambers have sufficient mechanical strength to act as their own support; each chamber is mounted from the previous layer with simple stand off brackets. In addition, a 1 mm layer of lead sheet can be added to the outside of the outer chambers, to shield the detector from synchrotron radiation, but this has not been required. The structure and installation procedure were designed to position the chambers to an accuracy of a few millimetres. The actual positions were then determined

by surveying, to an accuracy of one millimetre. Nominally all the sense wires are parallel to the z axis. The chambers in the four layers are staggered by typically 50 mm in the ϕ direction with respect to each other—firstly to resolve the left-right ambiguities when tracks are fitted, and secondly to provide drift time checksums which are sensitive to the drift velocity and relative positions. Thus the chambers are to some extent self calibrating.

A cross sectional view of the chambers is shown in fig. 34. Each chamber consists of two cells, side by side, each containing an anode wire (50 μm in diameter) running the whole length of the chamber and supported every 1.4 m. Electrons drift a maximum distance of 297 mm from either side. The sensitive volume is defined by two printed circuit boards with a nominal gas gap of 15 mm. The outside of the PC boards is copper clad and is at ground potential, as are the extruded aluminium side supports and the longitudinal central divider. The insides of the PC boards are etched and have strips 7.5 mm wide (with 2.5 mm gaps) to define the drift electric field. Opposite the anode wire there are "diamond shaped" cathode pads [71] (see fig. 35) which run the whole length of the chamber. They are used to determine the longitudinal coordinate z.

The gas is ethane (10%) and argon (90%), with typically 200 ml per minute flowing through each chamber. The drift velocity is 38 mm/μs, and as this is not saturated the voltage and gas mixture have to be suitably controlled. The maximum drift time is 8 μs; after this delay signals are available for the trigger.

Six signals are recorded from each cell—one from each end of the anode wire and four from the cathode pads, resulting in 1320 electronic channels. The signals are decoupled from the high voltage (with capacitors and transformers), amplified (using purpose built pre-amplifiers) at the chamber and digitised in TPDs [72]. These are FASTBUS FADCs developed for ALEPH, with the input amplifier/shaper redesigned to suit our pulse size and width. They operate at 12.5 MHz, and have 8-bit resolution.

The cathode pads operate at +4.0 kV, giving an average drift field of 13.4 V/mm. The anode wire is normally set at +1.85 kV relative to these pads. The computer controlled high voltage system has been specially designed and incorporates hardwired current limits and several fail-safe features.

Having all field shaping electrodes, cathode pads and the anode wire at a positive potential results in positive ions from the avalanches being deposited on the exposed surfaces of the dielectric of the PC board. This has the effect of smoothing the electric field between the shaping electrodes and the overall electric field configuration relaxes to the ideal form required. In these chambers almost 25% of the surface is exposed [73], and charging of the surfaces relies on the background of natural radioactivity. In the underground experimental area the charging takes a few hours.

The coordinate in the ϕ direction is determined by the drift time to an accuracy of better than 1.5 mm. The chambers also determine the longitudinal coordinate, z, to an accuracy of 2 mm (i.e. 0.02% of 10 m). This is achieved by a three stage process—fine z, medium z and coarse z. The fine z measurement uses induced signals on diamond-shaped cathode pads with a repeat distance of 171 mm, and determines the z coordinate to an accuracy of 2 mm, but modulo 171 mm. The medium z measurement is based on the same technique but the repeat distance is 1710 mm, and the accuracy about 30 mm. The coarse z measurement is obtained by comparing the pulse heights and time differences of the pulses from the two ends of the wire. The wavelength ambiguities of the fine z measurement are resolved by the medium and coarse measurements [70,71]. The fine z data are used to calibrate the medium z, and the medium z to calibrate the coarse z.

6.3.2 Endcap Muon Detector

The endcap muon detector covers the angular ranges $\sim 0.67 < |\cos\theta| < \sim 0.985$. At each end of the detector an area of ~ 150 m^2 is covered with four layers of limited streamer tubes which are perpendicular to the beam axis. Each endcap consists of 8 quadrant chambers (6 m × 6 m) and 4 patch chambers (3 m × 2.5 m) as shown in figs. 36a and b. Each chamber contains two layers of streamer tubes, spaced by 19 mm, one layer having vertical wires and the other horizontal wires, see fig. 37. Pairs of chambers are separated by 670 mm (i.e. layer 2 to layer 3). The quadrant chambers overlap vertically but not horizontally as space is taken (and the geometrical acceptance limited) by the beam pipe, shielding, cables to other subdetectors, magnet supplies and mechanical support for the pole tips. The patch chambers cover much of the gap between the quadrant chambers. The acceptance, averaged over ϕ, is shown in fig. 33. There is good overlap with the acceptance of the barrel muon detector.

The basic streamer tube unit [56,57,74] consists of a 1 mm thick fire resistant plastic [75] extrusion in the form of 8 contiguous square sections, each internally 9 mm by 9 mm. As shown in fig. 37, the extrusion has one side open and is surrounded by a gastight jacket. The inner walls of the extrusion are coated with a water-based carbon suspension [76] forming a cathode with a surface resistivity of about 5MΩ/square. There are 100 μm diameter anode wires every 10 mm, supported every 500 mm, which run the full length of the chambers. The tubes are filled with a gas of argon (25%) and isobutane (75%) and the anodes operate at a common high voltage of typically +4.3 kV, the cathodes being at ground. The streamers are detected by the charge induced on planes of aluminium strips located on either side of the gas jacket. The strips are 8 mm wide, with a gap of 2 mm, and are mounted on 3 mm thick fire resistant plastic boards [77]. The outer surfaces of the boards are covered with aluminium foil which acts as a ground plane.

The strips on the open side of the extrusion are perpendicular to the wires and see the streamer directly. Typically, the charge is shared between 4 or 5 strips and a weighted average, using the recorded pulse heights, locates the streamer to an accuracy of better than 1 mm. The strips on the closed side of the extrusion are parallel to the wires and locate the streamer only to the nearest wire. Thus, within each chamber (of two layers of wires and each with two planes of strips) each coordinate, x and y, of a track can be measured twice, once coarsely, and once more accurately. This arrangement also minimises inefficiencies due to tracks passing through the walls of the tubes, gas jackets and gaps between units. The actual positions of the strips when the detector is in position are determined to an accuracy of about 1 mm by surveying the dowel pins which locate the 3 mm boards which carry the strips.

The signals from both types of strip (12,496 in all) are integrated for 5 μs following a beam crossing and the charges stored on capacitors [33]. During the readout the capacitors are discharged sequentially, in groups of 32, and the signals multiplexed (locally at the chambers) to 12-bit ADCs. A hardware processor identifies clusters of strips with a peaked distribution of charge. These clusters are extracted by software in another processor which subtracts pedestals, checks and monitors the data, formats it and passes it on.

A prototype chamber was tested and cluster algorithms developed with cosmic rays using a comparison with drift chambers (having 0.2 mm resolution). The efficiency was found to be consistent with the geometrical effects already mentioned. The strips, parallel to the wires, gave spatial resolutions of 3 mm while the perpendicular strips were better than 1 mm.

The hadronic rejection power of the endcaps to punchthrough was investigated at a test beam using separated double layers of streamer tubes behind elements of the hadron calorimeter. At 45° the fraction of incident hadrons faking muons was measured to be 0.2% at 10–50 GeV.

7 Forward Detectors

The forward detectors measure the luminosity of LEP by detecting small-angle Bhabha scattering, and also tag electrons from $\gamma\gamma$ interactions. Fig. 38 is a detailed cross-section through the forward detector between 2 and 3 m from the intersection region, showing the gamma catcher, the drift chambers, the fine luminosity monitor counters, the calorimeter and the tube chambers. Fig. 39 shows the main parts of the forward detector supported from the end of the cantilever which carries the low-beta superconducting quadrupole.

There is clean acceptance for particles from the intersection region between 47 and 120 mrad from the beam line. In this range the only obstructions are 2 mm of carbon fibre in the beam pipe (traversed obliquely, so up to 0.2 X_0 thick) and 2 mm of aluminium in the thin window of the central tracking system pressure vessel, with aluminium webs in the horizontal and vertical planes to support the beam pipe. The front drift chambers and the "acceptance" counters of the fine luminosity monitor are mounted on the front of a light stiff honeycomb plate which has a thickness equivalent to 1 mm of aluminium. The inner part of the acceptance of the calorimeter, down to 39 mrad, is obstructed by a thick aluminium ring and by the bellows and flanges joining the beam pipe to the pressure window. Beyond 120 mrad there are obstructions inside the pressure vessel, including optics for the laser beams used to calibrate the jet chamber. The 24 tubes for these laser beams are supported by the forward detector as seen in figs. 38 and 39. The space which they occupy between the forward calorimeter and the endcap lead glass causes a gap in calorimetric acceptance in the polar angle region 142 -200 mrad which is covered by the gamma catcher.

Calorimeter

The forward calorimeter has 35 layers of lead-scintillator sandwich (24 X_0), read out with wavelength shifter to vacuum phototetrodes with charge-sensitive preamplifiers [54] and the CAMAC version of the charge integrating ADCs [39]. The front 4 X_0, the presampler, has wavelength shifter at the outside only, but the main calorimeter is read out on both the inner and outer edges. There are sixteen azimuthal segments, giving 48 readout channels per end. The lead-scintillator stack and the tube chambers are contained in half-cylindrical shells with a vertical split to allow the detector to be mounted around the LEP beam pipe. Studies of well contained Bhabha events show (fig. 40) that the energy resolution is consistent with $\sigma_E/E \sim 17\%/\sqrt{E}$, as seen in beam tests. The response is linear with energy and uniform between segments. The radial position resolution on electron showers, using the ratio of the inner to outer signals from the main calorimeter, is ± 2 mm near the inner edge. The azimuthal resolution, from the ratios of signals in adjacent segments, is $\pm 1.5°$ or less. At the energy of the Z^0 peak, the cross section for Bhabha scattering into the whole area of the main calorimeter (and demanding that the average energy in the two calorimeters is greater than 70% of the beam energy) is approximately 57 nb.

Tube Chambers

Between the pre-radiator and the main sections of the calorimeter are three planes of brass-walled proportional tube chambers [78], read out by a specially packaged version of the charge multiplex system [33]. The absolute position of the tubes is surveyed to ± 1 mm, checked by the collinearity of Bhabha events and by preliminary data from the drift chambers. The improved data evaluation in 1990 results in a precision of ± 0.5 mm. Shower fluctuations (after 4 X_0 of preradiator) give errors of ± 3 mm on individual shower positions.

Drift Chambers

The drift chambers [79] in the front plane (see fig. 39) have composite faces of 150 μm glass-reinforced plastic (GRP) and polystyrene foam. Those in the rear plane have 1.6 mm GRP faces. Each chamber has two gas gaps with two sense wires per gap. Drift directions are approximately radial. The ambiguity between inward and outward drifts is resolved by displacing the sense wires in the first gap of each chamber outwards by 2 mm from those in the second gap. The position of a hit along a wire is measured by charge division and by a pattern of intersecting diamond pads [71] on the faces close to the wires. Twelve channels from each chamber are read out via FADC modules [16]. Beam and cosmic ray tests give an r.m.s. resolution of 300 μm in the drift direction and 1 mm along the wire, using the pad ratios.

Fine Luminosity Monitor

The fine luminosity monitor consists of four pairs of precisely positioned 6 mm thick scintillators (fig. 41) at each end, on the 45° diagonals to avoid showers from the beam pipe support webs. They cover the angular region 50–109 mrad from the beam axis, with an azimuthal coverage of about 36%. The front "acceptance" counters are 10 mm smaller on all sides than the rear "coincidence" counters. This reduces systematic errors due to small misalignments of beam and detectors [80]. Test beam results using electrons show a timing resolution of 300 ps which allows the rejection of "backsplash" from showers in the forward calorimeter. Both charge and time are recorded for each event. The cross section for Bhabha scattering into the fine monitor counters is ~7 nb at the Z^0.

Gamma Catcher

The gamma catcher is a ring of lead-scintillator sandwich modules, 7 X_0 thick, with wavelength-shifter readout to silicon photodiodes. Charge sensitive amplifiers [54] are read into charge integrating ADCs [39]. Beam tests have shown a linear response to electrons up to 5 GeV. The energy corresponding to an upward fluctuation of two standard deviations of pedestal noise is 1 GeV in the poorest segment. Thus any electrons or gamma rays of more than 2 GeV are detected, giving a veto on background events to the neutrino counting channel $e^+e^- \rightarrow Z^0\gamma$, with $Z^0 \rightarrow \nu\bar{\nu}$.

Far Forward Monitor

The far forward luminosity monitor counters are small lead-scintillator calorimeters (50 mm × 150 mm × 20 X_0) mounted on either side of the beam pipe 7.85 m from the intersection region, beyond the low-beta quadrupoles. They are segmented into 6 separate readout sections to give information on the position of showers. Electrons scattered through between 5 and 10 mrad close to the horizontal plane are bent outwards by the quadrupoles into the far forward acceptance, giving an effective cross section of ~460 nb for Bhabha scattering at the Z^0.

Luminosity Measurement

For the 1989 LEP running, the luminosity was measured by a combination of calorimeter and tube chamber data [81]. The forward calorimeter and the Bhabha triggers were required to be operational at all times. The relative normalisation for each LEP fill used the calorimeter with a cut on the average energy seen in the two main sections giving approximately 1.3 times as many Bhabha events as hadronic Z^0 decays at the peak. For absolute normalisation a precise acceptance region for Bhabha events was defined with the tube chambers, corresponding to 24.23 nb for Bhabha scatters at the Z^0 peak. The requirements were: $58 < \theta_{mean} < 120$ mrad; $\phi_{mean} > 10°$ from horizontal or vertical; $E_{mean} > \frac{2}{3} E_{beam}$; where θ_{mean}, ϕ_{mean} and E_{mean} are the scatter angle, the azimuthal angle and total energy (main + preradiator), averaged between the two ends. The overall systematic normalisation error was ±2.2%

absolute, with an estimated $\pm 1\%$ relative error between beam energy points [82]. A check of the absolute measurement of the luminosity was made by selecting Bhabha events which lay inside the clean "shadow" cast on the calorimeter by the thick aluminium ring (with precisely known dimensions) which supports the beam pipe.

8 Trigger and Online System

8.1 Overview

At LEP, bunch crossings occur every 22.2 μs. A flexible and programmable trigger system uses fast information from the subdetectors to select crossings with a possible e^+e^- interaction, reducing the 45 kHz bunch crossing rate to an event rate of 1-5 Hz which can be handled by the data acquisition system. The overall scheme of event triggering, readout, monitoring and data recording is shown in fig. 42.

The read out system has a distributed tree structured architecture. Microprocessors of the 68020/68030 [83] type, running the OS9 operating system [84], are used in a VMEbus [85] based system for data compression and data moving as well as monitoring. The VME crates are interconnected using a fast parallel link for (sub-)event routing. The sub-events containing the digitised information of the subdetectors are buffered in memories controlled by the subdetector processors and then collected and merged into a single data structure by an "event builder" VME system. This system also acts as an event buffer for a microprocessor matrix, where up to ten 68030, in parallel, perform a first analysis of the complete events, and undesired background can be rejected at this stage. From here, events are transferred from the underground experimental area via an optical link to the surface, where they are buffered in another microprocessor controlled VME system. It is envisaged that selected events will be sent from here to a set of fast processors for online event reconstruction. Finally, the events are transferred to the main online computer, a VAX 8700, and stored on magnetic tape cartridges.

In the following sections the trigger system and the data acquisition are described in more detail.

8.2 Trigger

The trigger system [86] is designed to provide high efficiency for the various physics reactions, and good rejection of backgrounds arising from cosmic rays, from interactions of the beam particles with the gas inside the beam pipe or the wall of the beam pipe, and from noise. Most of the physics reactions are triggered by several independent conditions imposed on the subdetector signals. This redundancy leads to a high detection efficiency and greatly facilitates the measurement of this efficiency.

The 4π range in solid angle covered by the detector is divided into 144 overlapping bins, 6 bins in θ and 24 bins in ϕ (see table 6). The subdetectors deliver trigger signals matched as closely as possible to this binning. This fine segmentation allows low thresholds for the calorimeters, since analogue sums are made over only a small region and thus noise is reduced. Besides the θ-ϕ signals, the subdetectors deliver "stand-alone" signals, derived from total energy sums or track counting.

The trigger signals from the various subdetectors are logically combined in the central trigger logic. θ-ϕ signals are used for hit counting, for the definition of back-to-back hits and to build detector

coincidences correlated in space. An overview of the θ-ϕ matrix is given in fig. 43. Programmable conditions are imposed on the θ-ϕ matrix outputs and on the stand-alone signals to decide whether an event is accepted or rejected.

The following subsections describe the trigger signals provided by the various subdetectors.

Track Trigger

The track trigger is a dedicated programmable hardware processor using input from the vertex detector and the jet chamber. Tracks are recognized in the r-z plane if they originate from the interaction region within an adjustable range in z. Four "rings" (each of 12 adjacent wires) are used, one ring consists of the axial wires of the vertex detector and the other 3 rings are provided by the jet chamber. The radial positions of the rings in the jet chamber can be varied. The z position along the wires is obtained from the measurement of the time difference of propagation of signals to the two ends in the case of the vertex detector, and by charge division in the case of the jet chamber. The values of the ratio z/r for wires hit in each of the four rings are filled in four histograms with up to 32 slices in z/r. There are 24 sets of such histograms, one for each 30°ϕ segment, i.e. a pair of neighbouring jet chamber sectors and three adjacent sectors in the vertex detector. The presence of a track is indicated by the track trigger logic if a programmable minimum number of hits is found in corresponding slices of these histograms. A more detailed description of the principle and of the hardware is given elsewhere [86,87].

The track trigger accepts tracks within $|\cos\theta|<0.95$. Tracks which are well contained by the third radial section in the jet chamber, i.e. $|\cos\theta|<0.82$, are classified as "barrel tracks". The track trigger logic provides 144 θ-ϕ signals and 6 stand-alone signals for $\geq$1,2,3 barrel tracks or $\geq$1,2,3 tracks in the full detector. Signals indicating that the number of hits in one of the four radial sections is above a preset threshold are also foreseen. Typical single-track efficiencies are measured to be about 98% for tracks originating from the interaction region.

Time-of-Flight Trigger

The trigger signals of the time-of-flight system are based on coincidences of the signals from the phototubes at the two ends of the scintillation counters. This coincidence has to occur within a gate of $\pm$50 ns around the beam crossing. The counters are combined to form 24 overlapping ϕ sectors of 36° each. There is no segmentation in θ. The 24 ϕ sectors are used to form a signal typically demanding $\geq$6 sectors to have fired. In addition a multiplicity signal is envisaged which requires the number of counters hit to exceed an adjustable threshold between 2 and 5. The average trigger efficiency for a minimum ionising particle, including geometrical gaps was measured to be ~81% in 1989, and >90% in 1990 after adjustment of high voltages and thresholds.

Electromagnetic Calorimeter Trigger

The trigger signals from the electromagnetic calorimeter are based on analogue sums of groups of ~48 lead glass counters. A total of 200 analogue signals from the barrel calorimeter and 24 from each endcap are combined in analogue summing modules [88] to form overlapping θ-ϕ signals and total energy sums for the barrel and the endcaps. The total sums are discriminated in the modules at two thresholds, the higher one at ~6 GeV and the lower one at ~4 GeV (in 1989 the thresholds in the endcap were 10 GeV and 6 GeV, respectively). For the θ-ϕ signals two thresholds of ~2.5 GeV and ~1 GeV are available in 1990. The latter is used for signals to the θ-ϕ matrix, whereas the logical OR of the higher θ-ϕ threshold is used as a stand-alone signal.

Hadron Calorimeter Trigger

Signals from the 976 hadron calorimeter towers are summed in groups of 12 or 16 to generate 92 trigger element outputs. These are arranged in 9 circular rings, one covering each pole tip and endcap, the remaining 5 covering the barrel. For processing, each ring is split vertically into 2 half-rings.

After pedestal subtraction, the signal from each element is discriminated at 3 thresholds E1,E2,E3 (E1<E2<E3). The 92 signals ">E1" (E1 is approximately 1 GeV) are transformed by matching logic into 6×24 θ-ϕ signals for input to the trigger matrix. Additionally, a logical OR of all the element signals within a given half-ring is made separately for the 3 levels. For each of the 3 thresholds, any chosen pattern of coincidences between the half-rings can be selected using programmable array logic. The result for each threshold is available as a NIM level for use in a hadronic energy trigger. The hadron calorimeter trigger was not active in 1989, but will be implemented during 1990.

Muon Detector Trigger

Trigger signals from the muon detector are formed independently in the barrel and endcap regions. Three out of the possible four layers of chambers in the barrel muon detector are demanded to have fired in one ϕ bin of slightly more than 15°. The ϕ bins are non-overlapping (in the sense of table 6), and there is no segmentation in θ at the trigger level. The efficiency has been measured to be 95% per track. The barrel muon trigger is running at a rate of ~80 Hz, mostly due to noise and cosmic ray background, and therefore is used in coincidence.

The endcap muon trigger signals are formed by summing the charge over between 64 and 128 adjacent strips. A signal indicating the presence of a track is generated if the charge in at least two out of the four planes is above an adjustable threshold and consistent with a track originating from near the interaction region. The endcap muon detector provides 4×24 θ-ϕ signals, corresponding to two θ bins with $|\cos\theta|>0.823$ and two with $|\cos\theta|<0.823$. The latter are merged with the barrel in the central trigger logic and thus form one θ bin corresponding to the range $\theta_2 \rightarrow \theta_5$. There is no overlap in ϕ or θ, except for small regions arising from the necessity to convert the cartesian geometry of the endcaps into the polar coordinate system. In addition to the θ-ϕ signals the endcap muon detector provides three stand-alone signals corresponding to hits in the left or right endcap chambers and a left-right coincidence. The single track efficiency for muons has been measured as ~95%. A 0.2 Hz rate from cosmic ray background satisfying the left-right coincidence is observed.

Forward Detector Trigger

The total energy sum from the presampler and the calorimeter, discriminated at ~15 GeV, and sums of three adjacent ϕ segments of the main calorimeter, discriminated at ~13 GeV, form 17 basic trigger signals on either side. In addition, 8 signals per side from the fine luminosity scintillators are available. The above signals enter the forward detector trigger logic, where coincidences between the left and the right side detectors are formed. The signals sent to the central trigger logic are:

- A left-right coincidence of the total energy sums (total energy trigger)
- A coincidence of any back-to-back segments on the right and left side
- Any coincidence between back-to-back fine luminosity scintillators AND the total energy trigger
- Any coincidence between back-to-back fine luminosity scintillators AND energy above threshold in corresponding back-to-back segments of the main calorimeter.

In addition to these real coincidence triggers, the forward detector trigger logic also forms accidental triggers by building the same coincidences as described above, but with signals from one side being

delayed by four bunch crossings, corresponding to one complete revolution of a bunch in LEP. Only the half-event from the side contributing the real trigger signals can be digitised normally, therefore the roles of the two sides are alternated on each bunch crossing. The accidental triggers are accepted by the central trigger logic in the same way as normal triggers and provide an event sample containing background events from off-momentum particles, used to estimate the background contribution to real luminosity triggers.

Signals indicating that the energy on one side is above threshold are also provided and are combined with trigger signals from other detectors in order to select tagged photon-photon interactions.

The efficiency of the luminosity trigger was shown to be 98.5±0.3% during most of the 1989 data taking period. After the presampler was included in the energy sum the inefficiency is measured to be 0.16±0.03%.

Central Trigger Logic

The central trigger logic is installed in a dedicated Eurocrate, with a special "trigger bus" in addition to the standard VME/VSB bus. Up to 9 standard VME cards and 10 double height, purpose built trigger cards can be installed. One of the trigger cards receives up to 64 stand-alone signals from the subdetectors and makes them available on the trigger bus. Scalers on each of these signals allow the input rates to be monitored. Five cards of double-VME size receive the θ-ϕ signals transferred from the subdetectors on differential cables. All input signals are available to the trigger crate CPU in VME registers. Programmable array logic (PAL) is used to generate signals representing four types of conditions (see also fig. 43) : (1) At least one θ-ϕ bin set in the left endcap, the right endcap and in the barrel region. (2) Multiplicity counting, i.e. $\geq$1,2 θ-ϕ bins set, performed after projection on ϕ. Due to the overlap, three adjacent bins count as one and more than three adjacent bins count as two. (3) Hits in back-to-back θ-ϕ bins for all detectors except the muon detector. (4) A coincidence in at least one θ-ϕ bin of any two of the five detectors, except the coincidence between the hadron and electromagnetic calorimeters.

Logical combinations of signals on the trigger bus (i.e. subdetector stand-alone signals and θ-ϕ matrix outputs) are formed by the "pattern arrangement module" (PAM), which uses look-up memories and PAL logic to derive the trigger decision from the 120 possible inputs.

The trigger decision is broadcast to local trigger units (LTUs) in each subdetector readout crate by the global trigger unit (GTU). If the trigger decision is negative, a reset pulse is distributed 6 μs before the next bunch crossing. If an event is to be accepted, the GTU generates a trigger pulse, and transfers a central event number and the 120 PAM input bits to the LTUs. The wired OR of "busy" signals asserted by each LTU inhibits further triggers as long as the front-end readout is in progress.

Trigger Performance

A typical trigger definition as used in 1989 contained a logical OR of about 25 stand-alone and θ-ϕ matrix output signals and a logical OR of 15 two-signal coincidences, providing high redundancy for most of the interesting physics reactions as well as good efficiency. As an example, the efficiency for multi-hadronic events for the 98% solid angle accepted by the offline selection was >99.9%, with events being selected if any of the following conditions were satisfied:

- electromagnetic energy in the barrel >6 GeV
- electromagnetic energy in barrel >4 GeV AND one track in barrel
- electromagnetic energy in barrel >4 GeV AND one time-of-flight ϕ sector hit
- electromagnetic energy in either endcap >10 GeV

- electromagnetic energy in one endcap >6 GeV AND at least one track on the other side
- electromagnetic energy in both left AND right endcaps >6 GeV
- electromagnetic energy in barrel >4 GeV AND >6 GeV in one endcap
- $\geq$6 time-of-flight ϕ sectors hit
- 2 collinear time-of-flight ϕ sectors hit
- $\geq$2 barrel tracks
- 2 collinear tracks
- $\geq$3 tracks
- $\geq$1 track AND θ-ϕ correlated time-of-flight sector hit.

A list of all active triggers can be found in [86].

8.3 Data Acquisition and Processing

The data acquisition system [89] is based on a multi-level tree structure with data being buffered at each level. For each event, data are collected from 16 acquisition subsystems (14 subdetectors, trigger and track-trigger, see table 7), and from one of the stations of the slow control system (see below). More than 150,000 analogue signals coming from the subdetectors produce after first data reduction 100 kbyte of data, on average, per multi-hadronic event. The data collection and processing is performed in a series of stages, described in the following sections and shown schematically in fig. 42.

Front End Processing

The subdetectors have widely differing detection hardware. Table 7 shows the variety of requirements and solutions for the digitiser electronics. In addition to data collection, various data reduction tasks, such as pedestal subtraction, zero-suppression, pulse shape analysis and track finding are performed at this stage.

The VME system where all data of a subdetector are assembled and from where the subdetector is controlled is called the local system crate (LSC). A typical LSC contains one or more CPU boards (FIC 8230 [90] or MVME147 [91]), at least 5 Mbyte of memory, an ethernet interface, the interface to the front-end digitisers (VME to VME, CAMAC to VME , FASTBUS to VSB are available), the local trigger unit (LTU), and a VME crate interconnect. The LSCs acquire the data, format and prepare it for the software filter and where possible parametrise the raw data in order to reduce the size of the sub-event. In general the sub-events are buffered at the level of the raw and formatted data. The present contribution to the total event size from the various subdetectors is given in table 7. Event monitoring at the sub-event level is usually also done by the processor(s) in the LSC, or by a test computer attached to the LSC.

Because of the subdetector configuration, nine out of sixteen subdetectors are split and have two LSCs on opposite sides of the experiment, connected via the interconnect bus. For these subdetectors, only one of the two LSCs, the master, is connected to the common acquisition system and builds the corresponding sub-event.

Apart from integrated operation in the full system, the LSC can be used for autonomous data acquisition and independent control, particularly useful when setting up, debugging or monitoring.

Event Builder and Filter

The event builder and filter is a multiprocessor system consisting of two VME crates. The event builder crate contains four VME crate interconnect modules corresponding to the four branches into

which the 16 subdetector LSCs are grouped. The distance to the LSC varies from a few up to 60 m and the transfer rate over the interconnect bus is up to 3 Mbyte/s. There is an n-fold repetition of a basic unit (column), each comprising a dual ported 4 Mbyte memory module in the event builder crate, acting as a multi-event buffer, accessible via the VSB port by a filter processor [92] in the filter crate. The present number of four of such columns can be increased up to ten. A processor in the event builder crate synchronises the LSC readout and initiates DMA transfers of the sub-event data into the dual-port memory of a column. The data of the concatenated sub-events are formatted into a complete event and are then accessible to the filter processors. This system can handle 10 Hz of, on average, 100 kbyte events. A processor in the filter crate supervises the multi-event buffer of the accepted events and their transfer to the next stage.

The filter processors perform a fast analysis of each event. Events are classified into various physics candidate categories and events flagged as background can optionally be rejected or downscaled. The filter program uses the calibrated calorimeter signals, the time-of-flight and muon chamber information, and the jet chamber tracks, reconstructed by the jet chamber LSC processors. The program also manages many online monitoring histograms. The filter code is written in standard FORTRAN 77, and therefore runs also in the offline environment, where the filter algorithm code is developed and tested on data and Monte Carlo simulated data.

A Macintosh II microcomputer is connected to the filter crate by a memory-map link. It runs an event display program, for visual inspection of event properties and as a powerful monitoring facility.

Top Crate and Vax

The equipment described so far is close to the actual detector, about 100 m below ground. An optical fibre, operating at 4 Mbyte/s, conveys the data from the filter crate to the "top" VME crate at ground level. This crate is able to distribute events to attached fast processors, where it is envisaged that the event reconstruction will be performed in real time, using the full offline reconstruction program.

Finally, the events are transmitted via a high-speed parallel link [93] to the main online computer, a VAX 8700. Events are normally recorded on magnetic tape cartridges, but the option exists to write them to disk. Special classes of events (e.g. classified by the filter) can be written to both media.

The VAX 8700 is also the host for a cluster of 20 μVAXs and VAXstations, some of which are connected to LSCs and serve as subdetector test computers.

Software Environment

All processors in VME run the OS9 operating system [84]. Programming languages used are Assembler, C and FORTRAN (RTF/68k [94]).

Networking protocols over the ethernet local area network (LAN) between processors in VME crates, the VAX 8700, various workstations and the CERN main site include OS9 net [95], DECnet, TCP/IP [96] and CATS [97]. In addition, the OS9 systems have access over the LAN to virtual disks on the VAX [98].

Some of the VME systems, equipped with a SCSI interface [99], are connected to hard disks or magnetic tape drives. The latter allow local data recording on tapes at the LSC or event builder level.

Both online and offline analysis software use the FORTRAN memory manager ZEBRA [100]. From the LSC onwards the underlying structure of the event data is always the FZ ZEBRA memory format.

ZEBRA is also used for histograms and calibration data.

8.4 Vax Software Infrastructure

The data acquisition system is controlled by the online VAX cluster, which provides essential facilities for controlling the data taking operations. Much of the software is based on the MODEL suite of programs available from the CERN Data Division [101].

- Overall run control [102] uses an object oriented rule based system written in PROLOG. The different parts of the detector are separated into "objects", each of which has a certain set of defined states and a known set of commands for changing one state to another. The whole set of objects and state transitions is given as input to the rule based system, which then determines which state transitions have to be made and in which order. Commands to the run-controller are sent through a specially written human interface based on DEC windows.
- Gathering and display of status information is based on a distributed database developed within OPAL.
- Error messages from any VAX or VME crate in the experiment are routed to different screens or disk files. The OS9 implementation is OPAL specific.
- The run conditions are logged in a database [103].
- Access to a calibration database [104] is given to each OS9 crate.
- The flow of event data from VME/OS9 can be routed to tape, cartridge or disk files. Several output streams are possible.
- Final online monitoring is performed before the data are stored on mass media for offline analysis.

8.5 Slow Control

A control system [105] ensures the safe operation of the detector and also serves as a homogeneous interface to all subdetectors and to the general infrastructure of the experiment. The system consists logically of two parts. The first part supervises the common environment including safety aspects, and the second is specific to each subdetector. Since the same software and hardware frame is used for both parts, they are operated in a coherent way. The parameters of the common infrastructure such as voltages, gas flows, temperatures etc., which amount to about 5,000 channels in total at present, are continuously monitored by 7 VME stations distributed over the electronics huts. All values are compared to their nominal settings, written to a file, and when problems arise, the system notifies the operator and takes automatic corrective actions if required. These stations are always operational and also interface to the LEP wide security systems. One station is also connected to the data acquisition system in order to include control data in the physics event record. The software to control the different subdetectors usually runs in the corresponding LSC. The same software frame as used above drives the subdetector specific application programs. The control system can be run both locally at the VME station and centrally via the computer network from a dedicated station in the control room. Here the overall status of the detector is displayed on a Macintosh II personal computer in a graphical way. The operator can also request detailed information and can act on the detector. Another screen shows permanently all warnings and alarms of all parameters monitored by the system.

8.6 Performance of the Online System

The typical trigger rate during the first months of LEP running was about 1 Hz at the Z° with a luminosity of 3×10^{30} cm^{-2}s^{-1}. The average event size was 100 kbyte, and up to 600 kbyte for multi-hadron events. The average readout dead-time was 50 ms per event, which has been reduced to 25 ms in 1990. About 1.5 million events were recorded during the LEP runs in 1989, containing about 30,000 multi-hadronic Z° decays.

At the LEP design luminosity of 1.6×10^{31} cm^{-2}s^{-1} the rate is 0.5 Hz for multi-hadronic events produced by Z° decays, and 1 Hz for forward detector Bhabha events. Including background events, the expected trigger rate will be about 4 Hz, and the data rate to be handled by the event builder will be about 400 kbyte/s, after some improvements in data compression. Online filtering will reduce the amount of data written to tape by about a quarter.

9 Initial Performance

The construction of the OPAL detector was completed in July 1989. The detector has operated very well since the commissioning of LEP. The first hadronic Z^0 event in the one week "pilot" run was seen at 23:15 on August 13 1989. In 1989, physics data were recorded between September and December at centre-of-mass energies between 89.3 and 95 GeV. The data sample collected corresponds to an integrated luminosity of 1.3 pb^{-1} and contains ~30,000 hadronic and ~3,000 leptonic Z^0 decays. Fig. 44 shows a Z^0 decay into hadrons with signals from most of the detector components. The fast turn on of LEP and the experiment led to first physics results [106] already in October 1989.

Acknowledgements

The successful design, construction and commissioning of the OPAL detector would not have been possible without the tremendous efforts of all our technical collaborators in the participating institutes, and we warmly thank them for their dedication and support over the last ten years. The very important contribution of the hired technical manpower to the construction and assembly of the detector at CERN is warmly recognized. Without the outstanding services and support provided by the OPAL secretariat, under Mrs. M. Decamp, work in OPAL would have been much less efficient and pleasant. It is a pleasure for the visiting groups to thank CERN for its hospitality. We gratefully acknowledge the financial support of the following: The Bundesministerium für Forschung und Technologie, FRG, The Department of Energy, USA, The Direction des Sciences de la Matiere (DSM), France, The Israeli Ministry of Science, The Minerva Gesellschaft, The National Science Foundation, USA, The Natural Sciences and Engineering Research Council, Canada, The Japanese Ministry of Education, Science and Culture (the Monbusho) and a grant under the Monbusho International Science Research Program, The Science and Engineering Research Council, UK and The A. P. Sloan Foundation.

References

[1] OPAL Technical Proposal, CERN/LEPC/83-4.

[2] P. Roudeau et al., LEP Note 439, K. M. Potter, LEP Note 441.
For more recent calculations see G. v. Holtey and K. M. Potter, CERN/LEP-BI/87-05.

[3] C. Hauviller, CERN-LEP-IM/88-14, paper presented to the 1988 European Particle Accelerator Conference in Rome.

[4] J.M. Roney et al., Nucl. Instr. and Meth. A279 (1989) 236.

[5] J.M. Roney, Ph.D. Thesis, Carleton University, unpublished.

[6] J.R. Carter et al., Nucl. Instr. and Meth. A286 (1990) 99.

[7] A.A. Carter et al., Nucl. Instr. and Meth. A286 (1990) 107.

[8] H. Drumm et al., Nucl. Instr. and Meth. 176 (1980) 333.

[9] H.M. Fischer et al., Nucl. Instr. and Meth. A252 (1986) 331.

[10] R.-D. Heuer and A. Wagner, Nucl. Instr. and Meth. A265 (1988) 11.

[11] H.M. Fischer et al., Nucl. Instr. and Meth. A283 (1989) 492.

[12] H.J. Burckhart et al., Nucl. Instr. and Meth. A244 (1986) 416.

[13] G. Bar et al., to be submitted to Nucl. Instr. and Meth..

[14] H. Breuker et al., Nucl. Instr. and Meth. A260 (1987) 329.

[15] P. Bock et al., Nucl. Instr. and Meth. A242 (1986) 237.

[16] P. v. Walter and G. Mildner, IEEE Trans. Nucl. Sci. NS-32, 626 (1985).

[17] D. Schaile et al., Nucl. Instr. and Meth. A242 (1986) 247.

[18] P. Bock and G. Tysarczyk, Nucl. Instr. and Meth. A283 (1989) 813.

[19] See, for example, J. Va'vra in Proc. of the Workshop on Radiation Damage to Wire Chambers, April 1986, LBL-21170, UC-34D, CONF-860162; and references herein.

[20] M. Huk et al., Nucl. Instr. and Meth. A252 (1988) 107.

[21] M. Hauschild, Ph.D. Thesis, Physikalisches Institut, Univ. Bonn, Bonn-IR-88-57.

[22] H. Mes et al., Nucl. Instr. and Meth. A265 (1988) 445.

[23] M.S. Dixit et al., technical note in preparation.

[24] DL300 FADC system manufactured by Dr. B. Struck.

[25] E. Neuheimer et al., technical note in preparation.

[26] NE110 scintillator, from Nuclear Enterprises.

[27] XP2262B phototubes, from Philips Components, 5600 MD Eindhoven, Netherlands.

[28] An Ji-Gang et al., Nucl. Instr. and Meth. A267 (1988) 386.

[29] An Ji-Gang et al., Nucl. Instr. and Meth. A267 (1988) 396.

[30] G. Battistoni et al., Nucl. Instr. and Meth. 164 (1979) 57.

[31] Acheson Colloids Company, Electrodag 120, diluted 10:1 in ethanol.

[32] SY127-A232P High voltage system, from CAEN, Viareggio, Italy.

[33] R.L. Chase and I. Corbett, IEEE Trans. Nucl. Sci., NS-32, 645 (1985).

[34] SF57 lead glass, from Schott Glaswerke, Hattenbergstrasse 10, D-6500 Mainz 1, West Germany. This glass has the following properties: 75% by weight PbO, density 5.54 g cm^{-3}, X_o 1.50 cm, and refractive index 1.8467 at $\lambda = 586$ nm.

[35] R2238 phototubes, from Hamamatsu Photonics K.K., Ichino-cho, Hamamatsu, Japan. These phototubes have the following properties: 12-stage mesh dynodes, effective diameter of bialkali photocathode 70 mm, nominal amplification factor $\sim 1.0 \times 10^5$ at a typical high voltage of -1.0 kV.

[36] Cemedine 1565 adhesive, from Cemedine Co., Ltd., 5-9, Higashigotanda 4-chome, Shinagawa-ku, Japan. This adhesive has a refractive index of 1.56 at $\lambda = 586$ nm.

[37] TMB permaloy metal, from Tokin Corporation, 7-1, Kooriyama 6-chome, Sendai, Japan.

[38] C2645 high voltage power supply, and C2646 HV distributor, from Hamamatsu Photonics K.K..

[39] G. Schuler, "96-Channel FASTBUS Charge Integrating ADC CIAFB F683C", CERN/EF/4102H/GS/ed (1988).

[40] "The West Area Beam", D. E. Plane, CERN/SPS/83-22, and CERN/SPSC/83-36.

[41] Mitsui Engineering and Shipbuilding Co. Ltd., 6-4, Tsukiji 5-chome, Chuo-ku, Tokyo, Japan.

[42] L2360 Xenon flash lamp, from Hamamatsu Photonics K.K..

[43] Optical fibres, from Fujikura Ltd., 11-20, Nishi-gotanda 2-chome, Shinagawa-ku, Tokyo, Japan.

[44] S1722-02 PIN photodiodes, from Hamamatsu Photonics K.K..

[45] C. Beard et al., Nucl. Instr. and Meth. A286 (1990) 117.

[46] M. Akrawy et al., Nucl. Instr. and Meth. A290 (1990) 76.

[47] M. Akrawy et al., to be submitted to Nucl. Instr. and Meth..

[48] M.D. Rousseau et al., IEEE Trans. Nucl. Sci., NS-30, 479 (1983).

[49] CEREN-25 lead glass, from Corning France, 44 Avenue de Valvins, Avon, Cedex 77210, France. This glass has the following properties: 55% by weight PbO, density 4.06 g cm^{-3}, X_o 2.51 cm, and refractive index 1.708 at $\lambda = 400$ nm.

[50] R.M. Brown et al., IEEE Trans. Nucl. Sci., NS-32, 736 (1985).

[51] XP1501/FL VPTs, from Philips-RTC, 130 Avenue Ledru-Rollin, Paris XIe, France. These VPTs have the following properties: nominal diameter of D-type photocathode 3", average gain at 0.4 (0.94) T is 13.5 (10.1) at the maximum high voltage of -1.2 kV.

[52] P.W. Jeffreys et al., Proceedings of the International Europhysics Conference on High Energy Physics, Bari, Italy, (1985) 590, and Rutherford Appleton Laboratory report RAL 85-058 (1985).

[53] Bisphenol A and trimethyl hexamethylene diamene, from CIBA Geigy Ltd.

[54] R. Stephenson, Rutherford Appleton Laboratory reports RL 82-082 (1982), RL 83-075 (1983), RAL 87-019 (1987).

[55] G. Battistoni et al., Nucl. Instr. and Meth. 152 (1978) 423; 176 (1980) 297; 202 (1982) 459.

[56] G. Battistoni et al., Nucl. Instr. and Meth. 217 (1983) 433.

[57] E. Iarocci, Nucl. Instr. and Meth. 217 (1983) 30.

[58] BREOX-B35, registered product of British Petroleum Corporation.

[59] F. Fabbri et al., OPAL internal report OPAL/O129n/1986; CERN-EP/87-134.

[60] A.H. Ball et al., IEEE Trans. Nucl. Sci. Vol.37, No. 2, April 1990, and University of Maryland Physics Publication MD/89-055.

[61] G. Artusi et al., University of Bologna Preprint, DFUB, 87/10, July 1987.

[62] G. Artusi et al., Nucl. Instr. and Meth. A279 (1989) 523.

[63] C.Y. Chang et al., Nucl. Instr. and Meth. A264 (1988) 194.

[64] S. Majewski et al., Nucl. Instr. and Meth. 217 (1983) 265.

[65] G. Bella et al., Nucl. Instr. and Meth. A252 (1986) 503.

[66] S. Dado et al., Nucl. Instr. and Meth. A252 (1986) 511.

[67] G. Mikenberg et al., Nucl. Instr. and Meth. A265 (1988) 223.

[68] "Simulation of the OPAL Hadron Calorimeter", CERN LEPC/85-8.

[69] J. Allison et al., Nucl. Instr. and Meth. A238 (1985) 220.

[70] J. Allison et al., to be submitted to Nucl. Instr. and Meth..

[71] J. Allison et al., Nucl. Instr. and Meth. A236 (1985) 284.

[72] B. Lofstedt, "TPD Time Projection Digitiser F6821", CERN-EP-EL, 89.04.13.

[73] J. Allison et al., Nucl. Instr. and Meth. 201 (1982) 341.

[74] G.T.J. Arnison et al., accepted by Nucl. Instr. and Meth. (1990).

[75] Noryl: modified polyphenylene oxide developed by General Electric Plastics Co. Profile extrusions by Copely Developments Ltd., Leicester, UK.

[76] V-10 carbon suspension produced by Tech-Chem Ltd., Newcastle, UK.

[77] Noryl boards extruded by BMB SA, Belgium.

[78] D.C. Imrie et al., Nucl. Instr. and Meth. A238 (1989) 515.

[79] B.E. Anderson et al., Nucl. Instr. and Meth. A238 (1989) 650.

[80] J.E. Crawford et al., Nucl. Instr. and Meth. 127 (1975) 17.

[81] OPAL Collaboration, M.Z. Akrawy et al., Phys. Lett. B240 (1990) 497.

[82] N.C. Wood, Ph.D. Thesis, University of London, 1990.

[83] MC68020, MC68030 32-bit Microprocessors; Motorola Inc..

[84] OS9 is a single processor, multi-tasking Operating System for the 68000 processor family; Microware Systems corporation, 1900 N.W. 114th Street, Des Moines, Iowa 50322.

[85] IEEE 1014/D1.0.

[86] "The OPAL Trigger System"; OPAL Collaboration, to be submitted to Nucl. Instr. and Meth..

[87] A.A. Carter et al., Nucl. Instr. and Meth. A250 (1986) 503.

[88] G.Schuler, "ANAMAT FASTBUS Linear Summing Module"; CERN/EF/ in preparation.

[89] "The OPAL Data Acquisition System"; OPAL Collaboration, to be submitted to Nucl. Instr. and Meth..

[90] FIC8230 Option 4, Fast Intelligent Controller; CES, Route du Pont-Butin 70, CH-1213 Petit-Lancy.

[91] MVME147, MC68030 based VMEbus processor board; Motorola Inc..

[92] Dual Port Memory VME/VSB, and FIC8231 with Motorola MC68030 processor and 68882 co-processor, running at 24 MHz. CES, Route du Pont-Butin 70, CH-1213 Petit-Lancy.

[93] VME DR11-W Emulator (IKON Corporation, 2617 Western Avenue, Seattle, Washington 98121) to DRB32-W (Digital Equipment Corporation, Maynard, Massachusetts) on the VAX BI bus.

[94] RTF/68k manual, H.v.d. Schmitt, Phys. Institut, Univ. Heidelberg.

[95] Microware Systems Corporation, 1900 N.W. 114th Street, Des Moines, Iowa 50322.

[96] TCP/IP; Microware Systems Corporation, 1900 N.W. 114th Street, Des Moines, Iowa 50322.

[97] CATS is a CERN defined interface to OSI transport service protocols.

[98] "OS-9 Network Disk Server", ALEPH internal note 88-52, DATACQ 88-9.

[99] SCSI Interface for FIC8230; CES, Route du Pont-Butin 70, CH-1213 Petit-Lancy, VME/SCSI Interface CC-74; COMPCONTROL, Eindhoven, Holland.

[100] ZEBRA Data Structure Management System; CERN Computer Centre Library.

[101] MODEL Vax online data acquisition system, CERN Data Division: Model Buffer Manager (MBM), Recorder (MRS), Error Message Utility (EMU), Model Process Control (MPC), Model Human Interface (MHI).

[102] "The OPAL Run Control", presented at: International Workshop on Software Engineering, Artificial Intelligence and Expert Systems for High Energy and Nuclear Physics; March 1990, Lyon Villeurbanne (France).

[103] ORACLE database, ORACLE Corporation, California, USA.

[104] OPCAL database, based on the CERN Zebra direct access package RZ (OPAL internal notes OPAL/OFFL/36/0003 and OPAL/OFFL/36/0005).

[105] "The Control System of the OPAL Detector at LEP". Paper presented at the International Conference on Accelerator and Large Experimental Physics Control Systems; Vancouver, British Columbia, Canada, October 30 - November 3, 1989, Proceedings to be published in Nucl. Instr. and Meth..

[106] OPAL Collaboration, M.Z. Akrawy et al., Phys. Lett. B231 (1989) 530.

Table 1

Magnet Parameters

Central field	0.435 T
Mean coil diameter	4.36 m
Distance between pole faces	6.3 m
Solenoid thickness	96 mm of Al + 54 mm of glass-epoxy (~1.7 radiation lengths, including pressure vessel)
Maximum current	7000 A
Maximum power	5 MW
Cooling water flow	40 l/s
Pressure drop	15 bar
Barrel iron thickness	0.8–1.0 m
Coil weight	25 t
Overall magnet weight	2800 t

Table 2

Properties of the Tracking Chambers

Tracking Device	Vertex Detector	Jet Chamber	Z-Chambers
Wire organisation	36 sectors axial 12 wires/sector, 36 sectors stereo (4°) 6 wires/sector	24 sectors 159 wires/sector	24 chambers 8 cells/chamber 6 wires/cell
Wire spacing (mm) Wire stagger (μm)	5.3 and 5.0 ± 41	10.0 ± 100	4.0 ± 250
Maximum drift distance Maximum drift time	1.4 cm 0.5 μs	25 cm 5 μs	25 cm 5 μs
Gas	argon(88.2%), methane(9.8%), isobutane(2.0%) at 4 bar		
Gas gain	2×10^4	10^4	$2\text{–}5 \times 10^4$
Angular coverage	$23° \leq \theta \leq 157°$ (92% of 4π) for axial + stereo wires, $18° \leq \theta \leq 162°$ (95% of 4π) for axial wires	$43° \leq \theta \leq 137°$ (73% of 4π) for 159 wires $11° \leq \theta \leq 169°$ (98% of 4π) for ≥ 8 wires	$44° \leq \theta \leq 136°$ 94% in ϕ 67% of 4π
Coordinate determination ϕ z	drift time ΔT and stereo wires	drift time charge division	charge division drift time
Spatial resolution ϕ z	55 μm 4 cm(ΔT), 700 μm(stereo)	135 μm 6 cm	15 mm 100–350 μm
Double hit resolution	2.0 mm	2.5 mm	2.5 mm
Energy loss dE/dx		3.8% (159 samples)	
Trigger z/r	all axial wires	3 groups of 12 wires per sector	

Table 3

Properties of the Electromagnetic Calorimeter

Detector	Property	Barrel	Endcap
Presampler	Angular coverage, $\|\cos\theta\|$	< 0.81	0.83–0.95
	Active detector	Limited streamer tubes	Thin high gain MWPCs
	Number of anode (cathode) layers	2 (4)	1 (2)
	Wire diameter and type	75μm stainless steel	55μm gold plated tungsten
	Wire spacing	9.6 mm	4 × 2.0 mm
	Cathode strip pitch	11 mm	18 mm
	Typical high voltage	4.1 kV	3.5 kV
	Gas	n-pentane(32%), CO_2(68%)	n-pentane(45%), CO_2(55%)
	Number of readout channels	21,504	6,080
	Intrinsic spatial resolution for mip	~2 mm	2–4 mm
Lead glass	Angular coverage, $\|\cos\theta\|$	< 0.82	0.81–0.98
	Material	SF57, $X_o = 1.50$ cm	CEREN 25, $X_o = 2.51$ cm
	Block geometry	Quasi-pointing	Coaxial with beam line
	Typical block dimensions	~10 × ~10 × 37.0 cm^3	9.2 × 9.2 × 52.0 cm^3
	Depth (for photons from origin)	24.6 X_o	~22 X_o
	Number of blocks	9,440	2,264
	Čerenkov light detector	Field tolerant phototubes	Vacuum photo triodes
	Typical magnetic field at detector	0.002 T	0.45 T
	Detector gain (PMT or VPT)	~ 1.0×10^5	~12.3
	Detector high voltage	−1.0 kV	−1.0 kV
	Channel equivalent noise	~2 MeV	~14 MeV
	Intrinsic energy resolution	$\sigma_E/E \simeq 0.2\% + 6.3\%/\sqrt{E}$	$\sigma_E/E \simeq 5\%/\sqrt{E}$ at low energy
	Intrinsic spatial resolution (at 6 GeV)	~11 mm	~11 mm
	Trigger E>1 GeV	24 ϕ bins × 5 θ bins	24 ϕ bins × 2 θ bins
Combined	Typical material in front of lead glass	~2 X_o	~2 X_o
	Typical material to back of lead glass	~26.5 X_o	~23.5 X_o
	Typical λ_{Int} to back of lead glass	~2	~2
	Spatial resolution for em shower	~5 mm	2–5 mm
	Electron-hadron separation	~10^{-3}	~10^{-3}

Table 4

Properties of the Hadron Calorimeter

	Barrel	Endcap	Pole Tip
Angular coverage, $\|\cos\theta\|$	< 0.81	$0.81 - 0.91$	$0.91 - 0.99$
Active detector	Limited streamer tubes, cells 9 mm×9 mm every 10 mm. 1.4 to 10 m long.		Thin high gain multiwire chambers.
No. of layers of detector	9	8	10
High voltage	4.65-4.85 kV		3.5 kV
Gas	isobutane(75%), argon(25%)		n-pentane(45%), CO_2(55%)
Wire spacing	10 mm		2 mm
Wire diameter	100 μm		50 μm
Readout: towers	pulse height		pulse height
strips	digital		digital
Absorber (between layers)	100 mm iron		80 mm iron
Gap in iron, for detector	25 mm	35 mm	10 mm
Dimensions: radius	3.4–4.4 m	1.9–3.3 m	0.6–1.8 m
length	10 m	1.0 m	0.81 m
thickness of iron	0.8 m	0.7 m	0.72 m
Energy resolution	$120\%/\sqrt{E}$		
Strips (10 mm) Towers (pointing to vertex)	axial $\Delta\phi \sim 7.5°$ $\Delta\theta \sim 5°$	horizontal $\Delta\phi \sim 7.5°$ $\Delta\theta \sim 5°$	radial $\Delta\phi \sim 11°$ $\Delta\theta \sim 4°$
Trigger	92 analogue signals from groups of 4 × 4 towers		

Table 5

Properties of the Muon Detector

	Barrel	Endcap
Angular coverage, $\|\cos\theta\|$	0.72 for ≥ 1 layer 0.68 for 4 layers	0.67 – 0.98
Absorber; λ_{Int}	$\sim$8	8 – 14
Active detector	110 drift chambers, 1.2 m wide, with 2 wires per chamber. drift distance: 0.3 m lengths: 10.4, 8.4, 6.0 m	Limited streamer tubes, with 9 mm × 9 mm cells every 10 mm. lengths: 6, 3 m
Wire direction	along z	along x and y
Wire diameter	50 μm	100 μm
Number of layers Spacing	4 equally spaced over 0.6 m	4 19, 670, 19 mm
Area covered	cylinder: 10 m long, 5 m radius	12 m × 12 m at each end
Resolution position direction	$\sim$1.5 mm by drift time (ϕ) $\sim$2 mm by cathode pads (z) 5 mrad	$\sim$1 mm $x(y)$ by $\perp$ strips $\sim$3 mm $y(x)$ by $\|\|$ strips 5 mrad
High voltage	drift: 4.0 kV drift + signal: 5.85 kV	4.3 kV
Gas	ethane(10%), argon(90%)	isobutane(75%), argon(25%)
Readout	6 FADCs per wire: both ends of a wire and 4 cathode pads.	pulse height from orthogonal strips (10 mm repeat) from both sides of 4 layers.
Trigger	24 ϕ sector signals (any 3 of 4 layers)	θ-ϕ bins (any 2 of 4 layers)

Table 6

Theta-Phi Segmentation of the Trigger System

Theta bin	$\cos\theta$ range
1	-0.980 - -0.596
2	-0.823 - -0.213
3	-0.596 - 0.213
4	-0.213 - 0.596
5	0.213 - 0.823
6	0.596 - 0.980

Phi bin	ϕ range, degrees
1	0 - 30
2	15 - 45
3	30 - 60
...	...
23	330 - 360
24	345 - 15

Table 7

Parameters of the Data Acquisition System

Subdetector	Channels	Data size (kB)		Digitiser	Crate/Interface
		Low mult.	Hadron		
Vertex detector	648	2	4	Dedicated TDC	EURO/CAMAC
Jet chamber (compressed)	7680	20	120 50	FADC 100 MHz	EURO-ECL/VME
Z-chambers	2304	2	6	FADC 100 MHz	EURO-ECL/VME
TOF	320	2	2	TDC/ADC/PU16	CAMAC
Presampler barrel	21504	5	5	Multiplexed ADC	EURO/VME
EM barrel	9440	3	5	Charge Int. ADC	FASTBUS
Hadron towers	1472	2	2	Charge Int. ADC	CAMAC
Hadron strips	56146	1	2	Bit pattern	VME
Muon barrel	1320	6	6	TPD	FASTBUS
Presampler endcap	6080	1	2	Multiplexed ADC	EURO/VME
EM endcap	2264	12	12	Charge Int. ADC	FASTBUS
Hadron pole tip	336 10240	1	2	Charge Int. ADC Bit pattern	CAMAC VME
Muon endcap	42496	2	2	Multiplexed ADC	EURO/VME
Forward detector	1400	5	5	TDC/ADC/MuxADC FADC 50 MHz	CAMAC/EURO-ECL /VME
Track trigger	1296	7	7		FASTBUS
Trigger	640	1	1		EURO 12U/VME

Figure Captions

Fig. 1: General layout of the OPAL Detector.

Fig. 2: Cross section of a quadrant of the detector (a) perpendicular to the LEP beam axis, and (b) parallel to the beam axis.

Fig. 3: Isometric view of the magnet in its open position.

Fig. 4: Schematic view of the vertex detector.

Fig. 5: End-plate wire layout for a section of the vertex detector.

Fig. 6: Spatial resolution in r-ϕ as a function of drift distance for the axial drift cells of the vertex detector (drift field = 2.5 kV/cm, anode surface field = 360 kV/cm).

Fig. 7: Cut away view showing the anode wire support of the jet chamber on the outside of the conical end plates and the structure on the inside serving as support for the cathode wires and as field shaping electrode. The front part of this structure consists of the wire suspension, the wire positioning comb, one PC board holding the wires and the resistor chain and another PC board with the field electrodes. The back part consists of the field degrader and an aluminium profile.

Fig. 8: Schematic drawing of the electronic readout system from the jet chamber up to the processors. The data flow and the reduction taking place at each level are also indicated.

Fig. 9: Spatial resolution in r-ϕ as a function of drift distance for the jet chamber.

Fig. 10: Distribution of $1/p$ for tracks in events of the type $e^+e^- \rightarrow \mu^+\mu^-$ for the jet chamber.

Fig. 11: (a) Measured energy loss (truncated mean) in the jet chamber as function of momentum for tracks in multihadronic events and in events of the type $e^+e^- \rightarrow \mu^+\mu^-$. (b) Truncated mean for muons with momentum of ~45 GeV.

Fig. 12: Longitudinal section of a bidirectional z-chamber cell. The numbered elements are: (1) cathode; (2) drift field electrodes; (3) grid wires; (4) guard wires; (5) anode wires (the stagger has been exaggerated for graphic purposes); (6) inner electrode for wire 1 and 6 gain control; (7) Lexan box and cover; (8) G10 (glass epoxy composite) anode module; (9) HV distribution board; (10) space for the HV resistor chain, HV bridging board and anode module cabling. All dimensions are in mm.

Fig. 13: Mean z resolution as a function of drift distance and track angle for the z-chambers.

Fig. 14: Measurement of the primary vertex position in the 1989 physics run using all three subdetectors of the central tracking system. In the vertical direction the width of the distribution is dominated by the detector resolution, in the horizontal direction by the beam dimension.

Fig. 15: Impact parameter resolution for the tracking chambers measured with events of the type $e^+e^- \rightarrow \mu^+\mu^-$; (a) in the r-ϕ plane (σ=75 μm), (b) in the r-z plane (σ=2 mm with and σ=2.7 cm without the stereo wire information of the vertex detector).

Fig. 16: Invariant mass distribution for $\pi^+\pi^-$ pairs emerging from a secondary vertex.

Fig. 17: Residual distributions of (a) the time-of-flight as measured by the TOF system, and (b) the difference in z as measured by the TOF system and the barrel electromagnetic calorimeter. The distributions are for muons in dimuon events satisfying $|\cos\theta_\mu|<0.7$.

Fig. 18: Radiation lengths (a) in front of and (b) inside the active material of the electromagnetic calorimeter as a function of $|\cos\theta|$ at a typical angle in ϕ. The peaks in the material in front of the calorimeter at $|\cos\theta| \sim 0.8$ and ~ 0.96 arise from the structure of the pressure bell of the central tracking system. The structure in the active material of the calorimeter arises, for $|\cos\theta| < 0.8$ from the quasi-pointing block geometry, at $|\cos\theta| = 0.8$ from the barrel/endcap overlap and transition, and at $|\cos\theta| \sim 0.975$ from the endcap/gamma-catcher/forward calorimeter overlap and transition.

Fig. 19: Mechanical structure of the barrel electromagnetic presampler.

Fig. 20: Spatial resolution of the barrel electromagnetic presampler as a function of beam energy, from test beam data. The resolution from the lead glass alone is also shown for comparison. The data are for electrons at $\theta = 43°$.

Fig. 21: Barrel lead glass counter, showing optical and electrical connections.

Fig. 22: 3-D view and cross section of the endcap calorimeter. In (a) an artist's view of the endcap lead glass covered by the umbrella of presampler chambers is shown. The cross section in (b) shows the setup behind the profile of the pressure bell, which represents $\geq 50\%$ of the radiator material in front of the lead glass.

Fig. 23: Endcap lead glass counter, showing optical and electrical connections.

Fig. 24: Energy resolution of a prototype barrel section of the electromagnetic calorimeter, with and without a presampler, as a function of incident e^- energy. The material in front of the presampler is $2.08 X_0$ thick. Also shown is the resolution obtained without any material in front.

Fig. 25: Measured π^- misidentification probability as a function of e^- detection efficiency for isolated 20 GeV particles incident into 1.6 X_0 of aluminium in front of a production endcap section of the electromagnetic calorimeter. The curves represent the effect of various cuts on the data: cut on presampler output only (black squares), on lead glass output only (open circles), on correlated presampler and lead glass outputs (open squares), and finally on the correlated data together with an additional minimum presampler charge cut (black circles and shaded area). Some further improvement may be obtained by exploiting the lateral shower width in the lead glass.

Fig. 26: Components of a multi-cell plastic limited streamer chamber of the barrel and endcap hadron calorimeter.

Fig. 27: Barrel and endcap chamber assemblies of the hadron calorimeter.

Fig. 28: Average response of a 3×3 tower, 9 layer prototype of the hadron calorimeter to single particle pion beams for various angles of incidence. The dashed line is the prediction of a Monte Carlo simulation for normal incidence.

Fig. 29: Relative muon track finding efficiency for 5 GeV muons normally incident upon the 3×3 tower, 9 layer, prototype of the barrel hadron calorimeter, as a function of the minimum number of layers required to register a cluster of 5 or less strip hits, compared with the relative efficiency for finding fake muons in a 6 GeV hadron sample.

Fig. 30: (a) Cross section and (b) layout of the chambers of the poletip hadron calorimeter.

Fig. 31: (a) Energy deposited in the endcap electromagnetic calorimeter plotted against the energy deposited in the pole tip hadron calorimeter and (b) weighted energy sum for a 10 GeV incident beam.

Fig. 32: Total amount of material (in absorption lengths) that a particle has to penetrate in order to reach the muon chambers, as a function of $\cos\theta$, and averaged over the indicated ϕ ranges, as determined from the Monte Carlo simulation [68].

Fig. 33: Geometrical acceptance of the muon detector (requiring 3 layers) as a function of $\cos\theta$, averaging over ϕ.

Fig. 34: Cross section of a drift chamber of the barrel muon detector.

Fig. 35: Schematic layout of the diamond shaped cathode pads of the barrel muon drift chambers.

Fig. 36: (a) End-view and (b) side-view of the endcap muon detector.

Fig. 37: Chamber layout and orientation of the endcap muon detector.

Fig. 38: Cross section through the forward detector between 2 and 3 m from the intersection region.

Fig. 39: Simplified view of the forward detector, without cables and readout electronics, supported from the end of the cantilever which carries the superconducting low-beta quadrupole. The tubes for the laser beams used for the jet chamber calibration are dotted.

Fig. 40: Energy response of the forward calorimeter to Bhabha electrons near the Z^0 peak. A collinearity cut, using the tube chambers, removes most of the radiative tail in the energy spectrum. The fitted Gaussian curve corresponds to $\sigma_E/E = 17\%/\sqrt{E}$.

Fig. 41: Fine luminosity monitor counters and their honeycomb support plate. The cutaway shows one of the larger "coincidence" counters mounted behind the plate. The others shown are all "acceptance" counters.

Fig. 42: Overall scheme of event triggering, readout, monitoring and data handling.

Fig. 43: Overview of trigger generation by the θ-ϕ matrix. The track trigger (TT), the time-of-flight system (TOF), the electromagnetic calorimeter (EM), the hadron calorimeter (HA) and the muon detector (MU) send signals to the θ-ϕ matrix, the outputs of which, together with up to 64 additional NIM signals, are logically combined to form the final trigger decision. Crosses on the vertical lines representing different particle types passing through the detector indicate the sensitivity at the trigger level.

Fig. 44: Event display of a Z^0 decay into hadrons with signals from most of the detector components. This event shows a two jet structure with one penetrating track which is probably a muon.

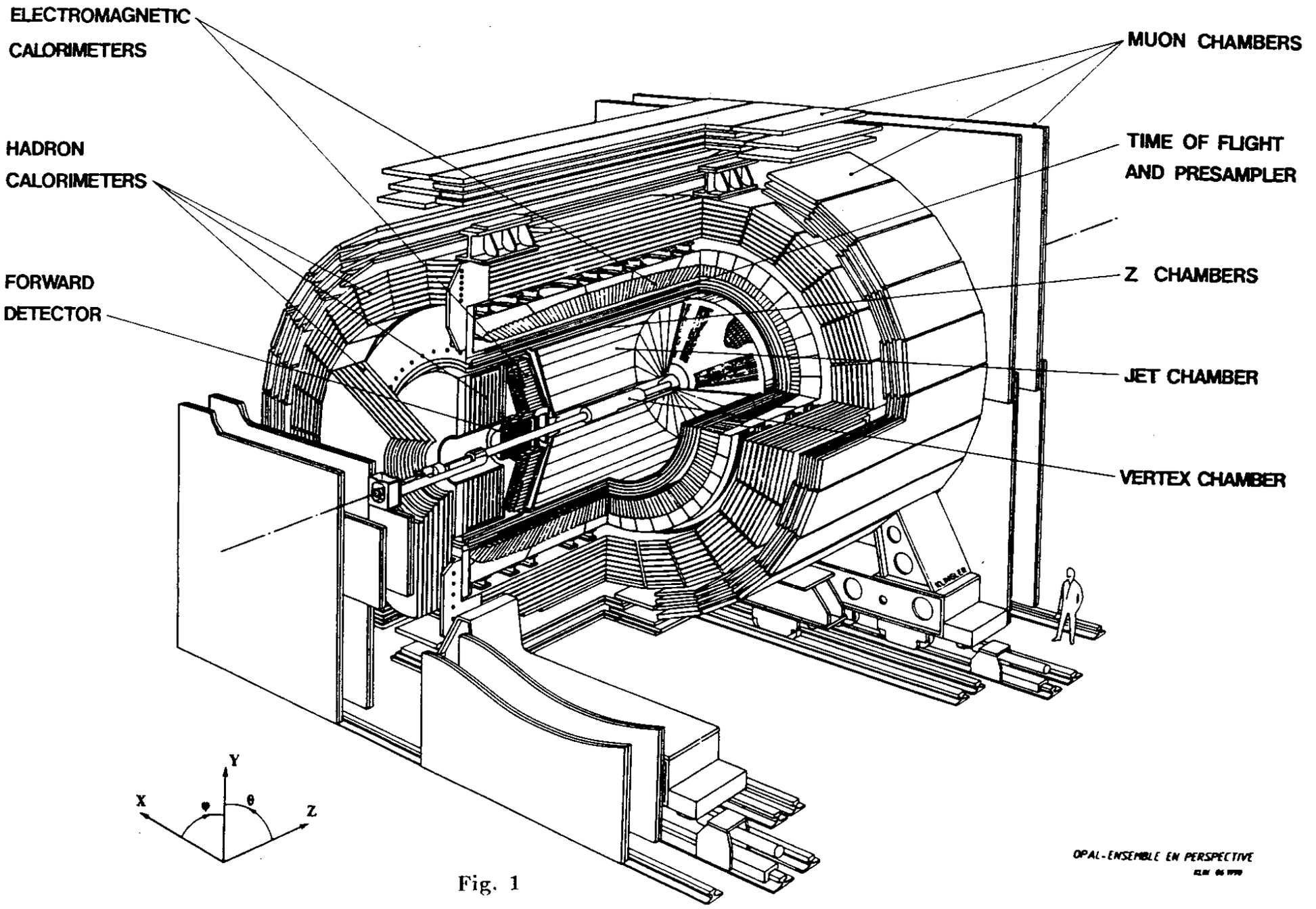
ELECTROMAGNETIC
CALORIMETERS
HADRON
CALORIMETERS
FORWARD
DETECTOR
MUON CHAMBERS
TIME OF FLIGHT
AND PRESAMPLER
Z CHAMBERS
JET CHAMBER
VERTEX CHAMBER
Y
X
Z
φ
θ
OPAL - ENSEMBLE EN PERSPECTIVE

Fig. 1

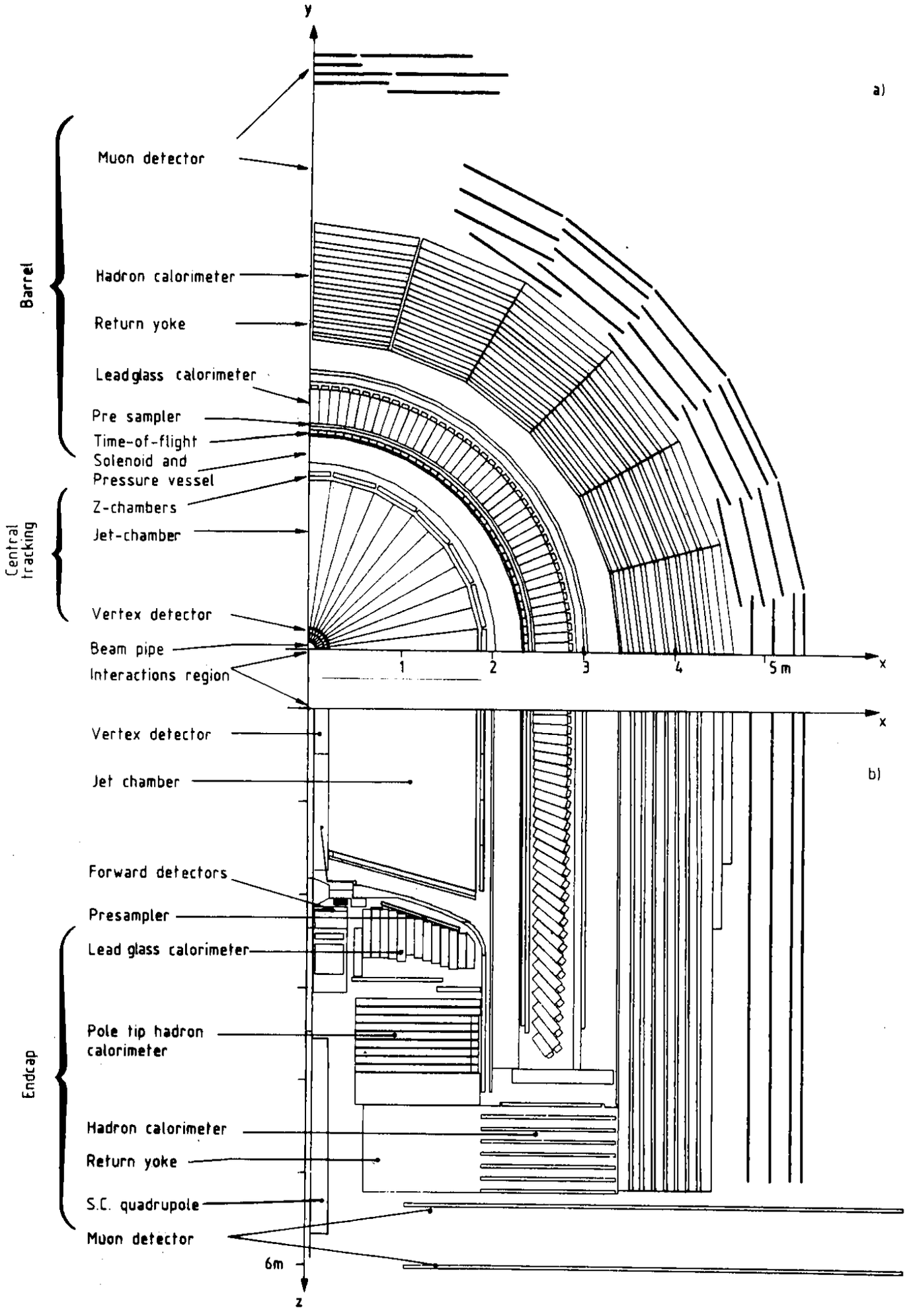
a)
b)
Barrel
Endcap
Central tracking
Muon detector
Hadron calorimeter
Return yoke
Leadglass calorimeter
Pre sampler
Time-of-flight
Solenoid and
Pressure vessel
Z-chambers
Jet-chamber
Vertex detector
Beam pipe
Interactions region
Vertex detector
Jet chamber
Forward detectors
Presampler
Lead glass calorimeter
Pole tip hadron calorimeter
Hadron calorimeter
Return yoke
S.C. quadrupole
Muon detector
1
2
3
4
5 m
6m
x
y
z

Fig. 2

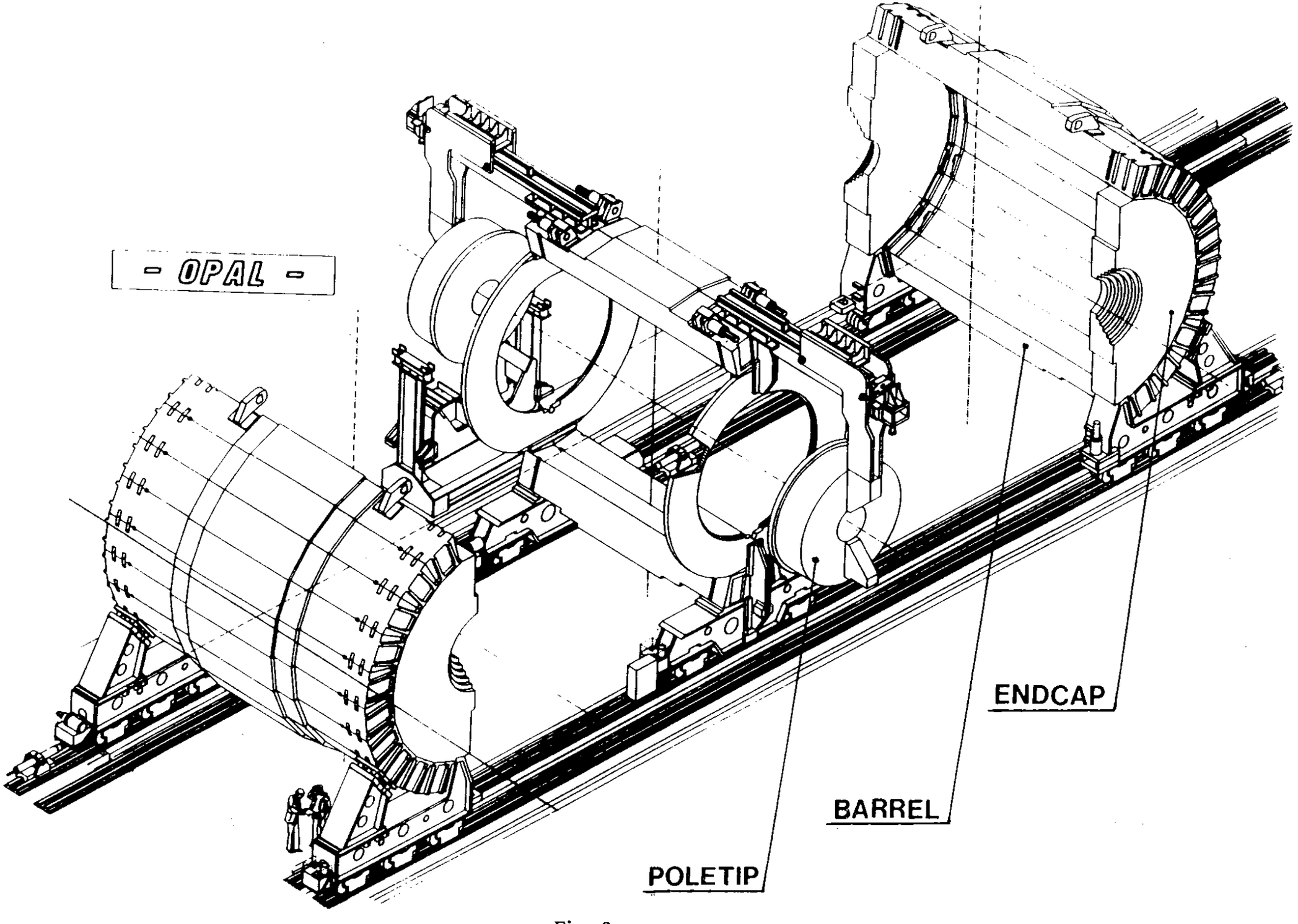

Fig. 3

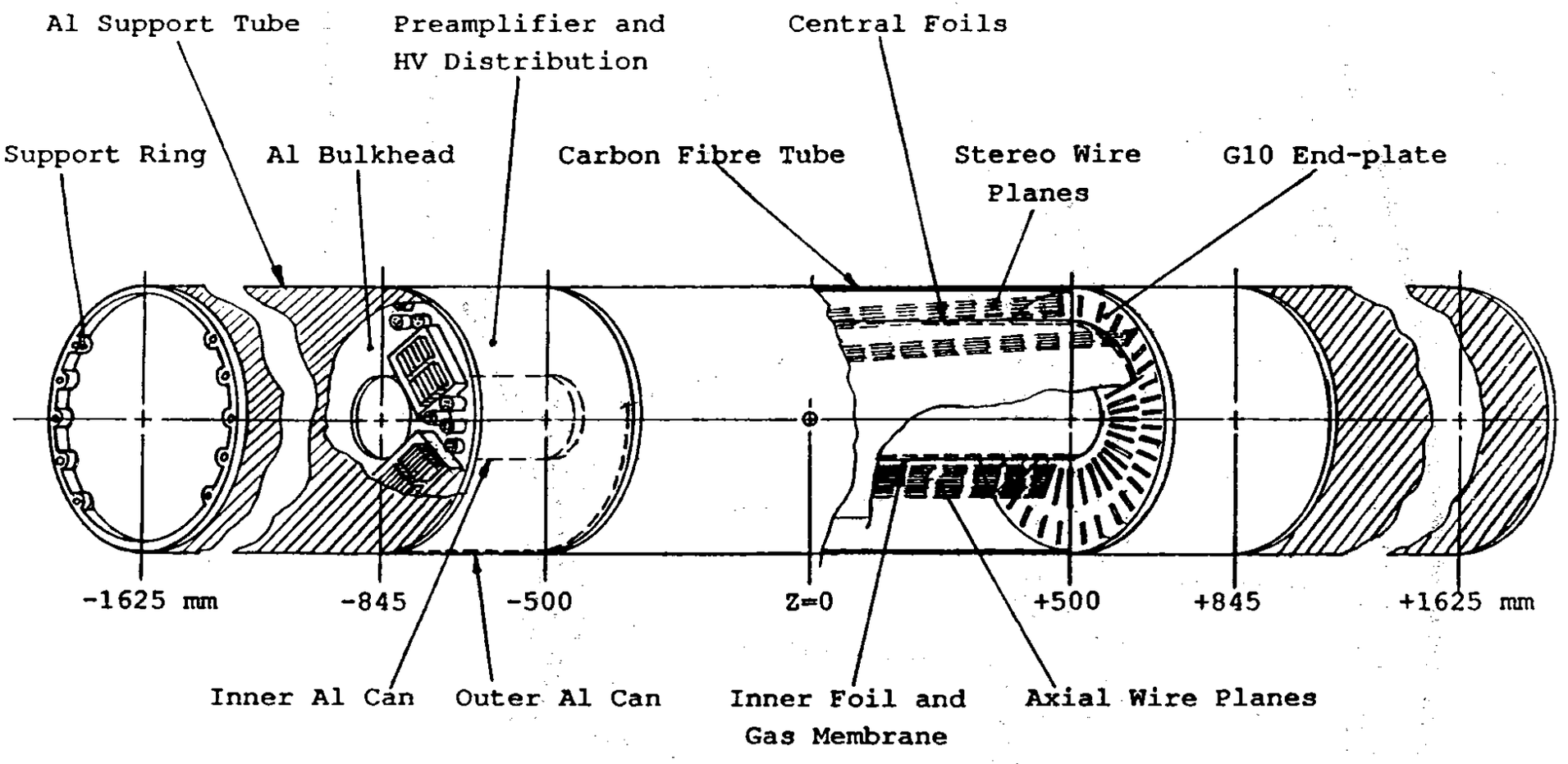
Al Support Tube
Preamplifier and
HV Distribution
Central Foils
Support Ring
Al Bulkhead
Carbon Fibre Tube
Stereo Wire
Planes
G10 End-plate
-1625 mm
-845
-500
Z=0
+500
+845
+1625 mm
Inner Al Can
Outer Al Can
Inner Foil and
Gas Membrane
Axial Wire Planes

Fig. 4

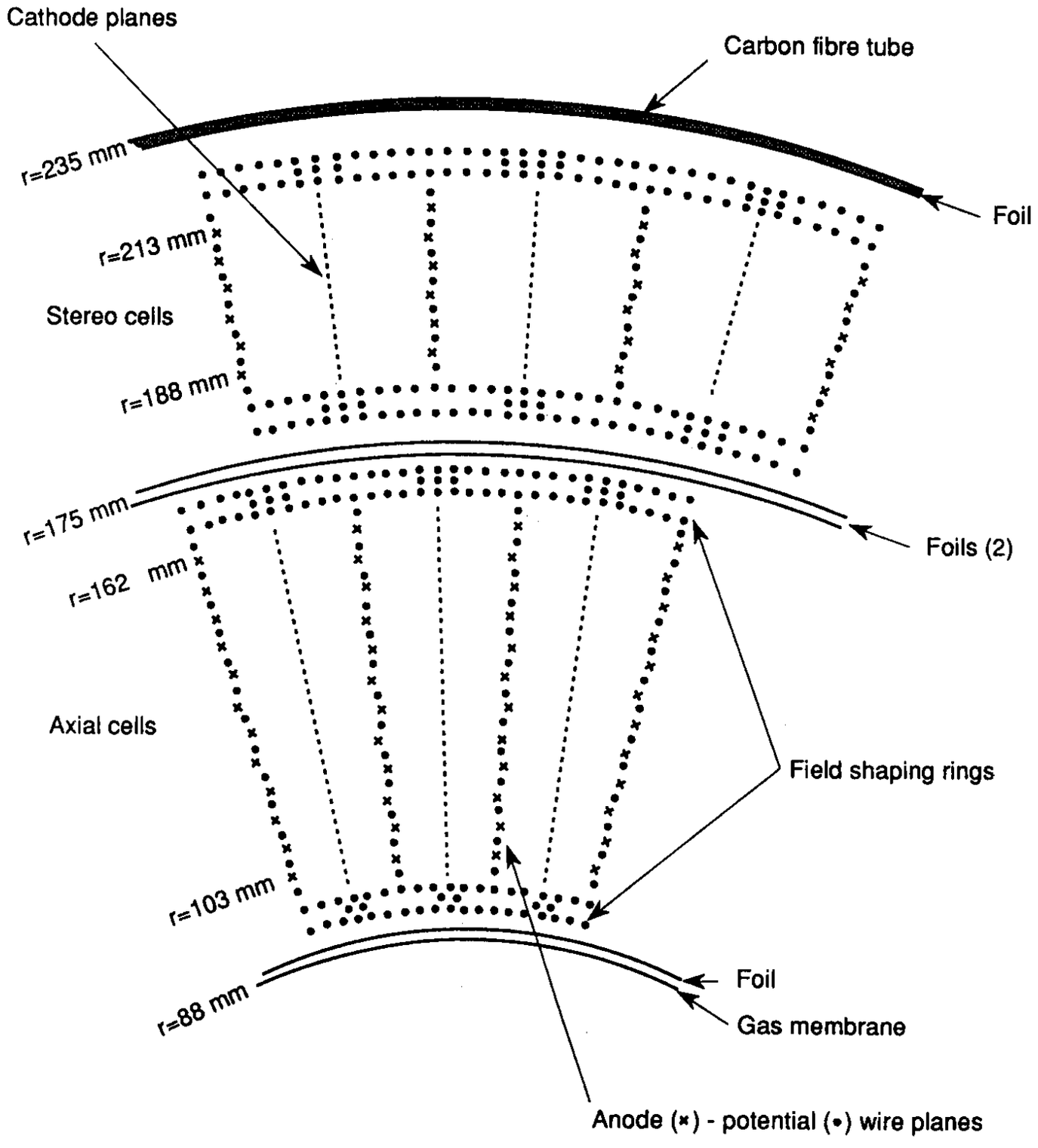
Cathode planes
Carbon fibre tube
r=235 mm
Foil
r=213 mm
Stereo cells
r=188 mm
r=175 mm
Foils (2)
r=162 mm
Axial cells
Field shaping rings
r=103 mm
Foil
r=88 mm
Gas membrane
Anode (×) - potential (•) wire planes

Fig. 5

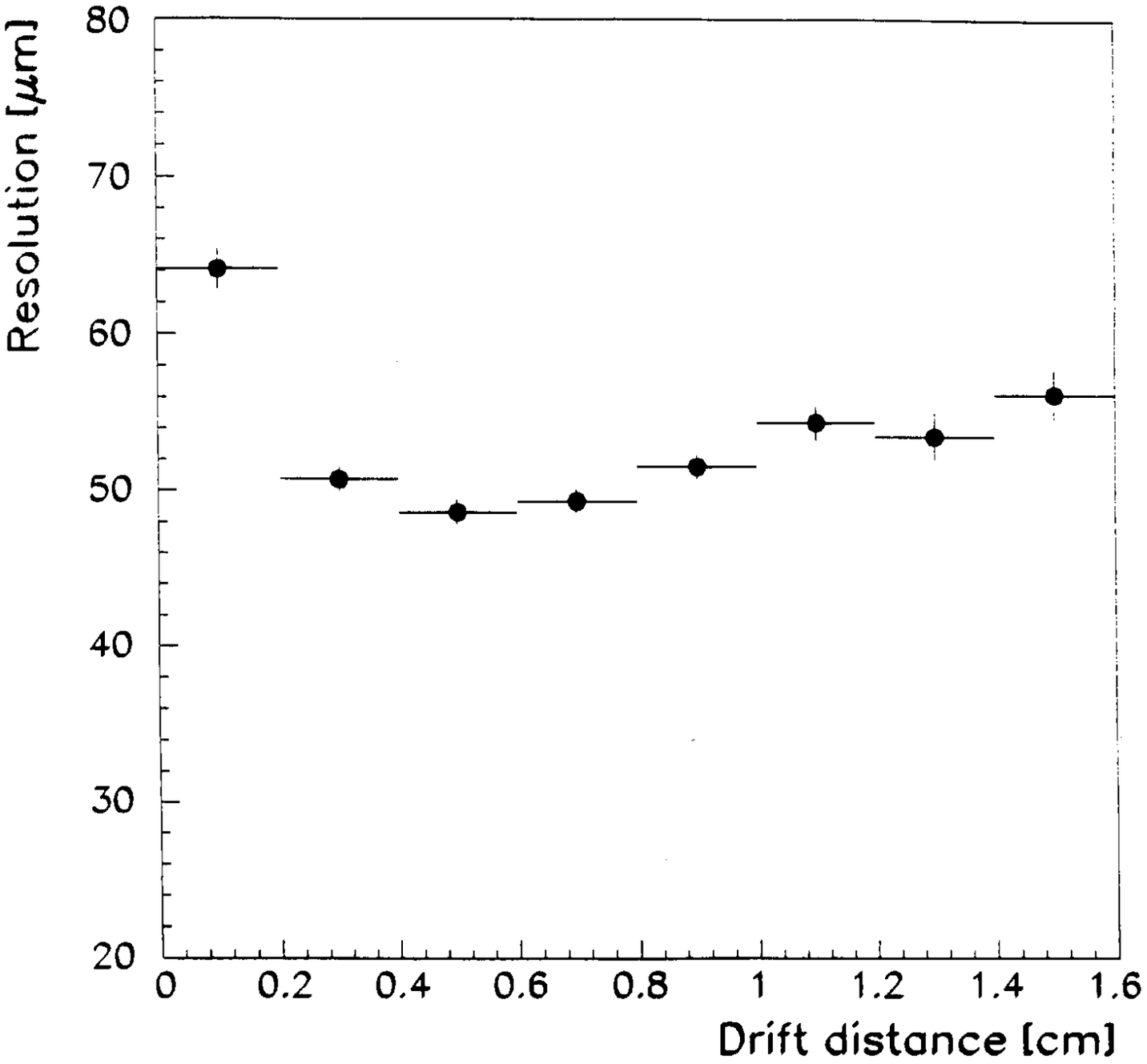
Resolution [μm]
80
70
60
50
40
30
20
0
0.2
0.4
0.6
0.8
1
1.2
1.4
1.6
Drift distance [cm]

Fig. 6

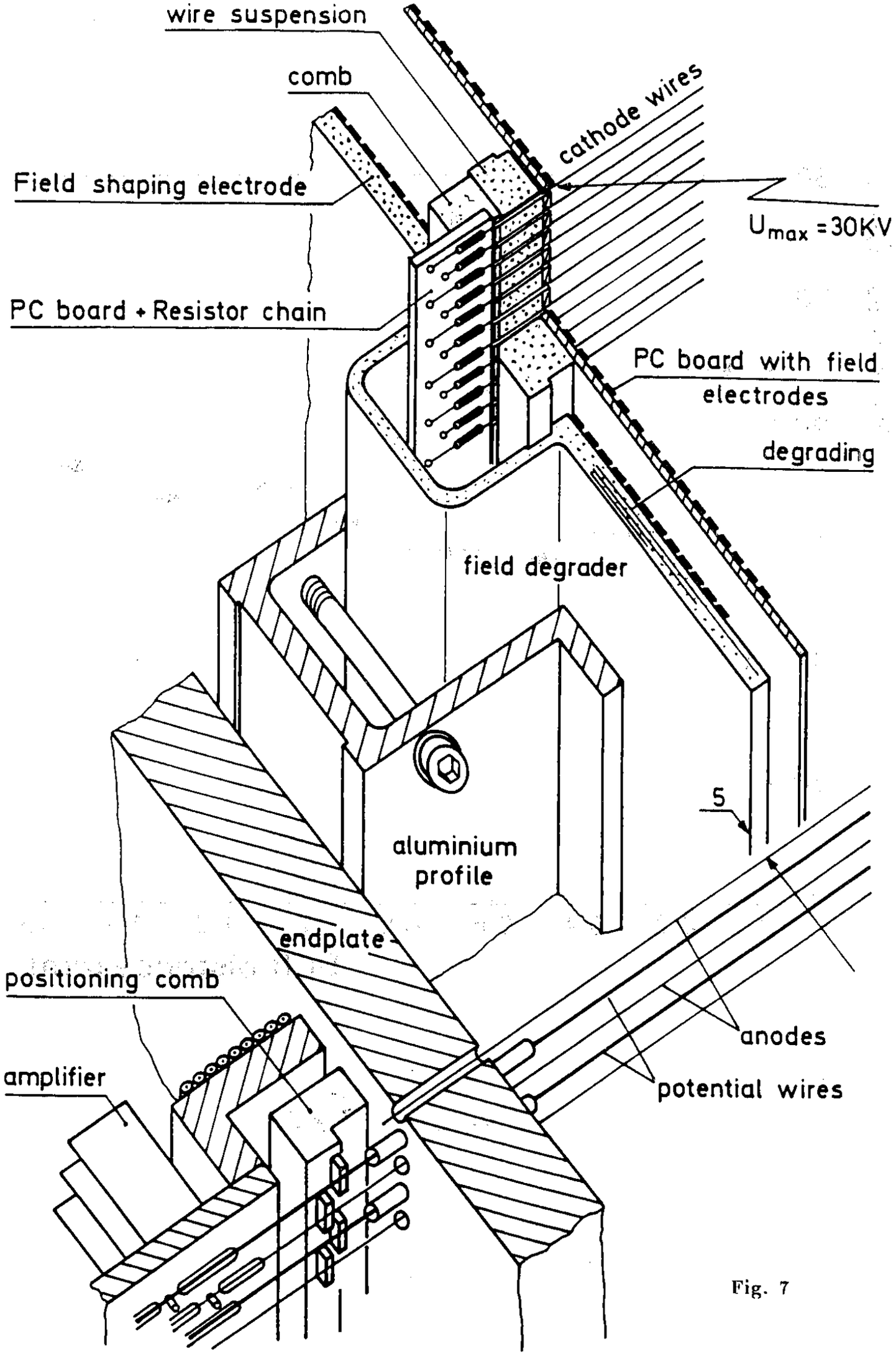
wire suspension
comb
cathode wires
Field shaping electrode
U_{max} = 30KV
PC board + Resistor chain
PC board with field electrodes
degrading
field degrader
5
aluminium profile
endplate
positioning comb
amplifier
anodes
potential wires

Fig. 7

JET Chamber Data Flow:

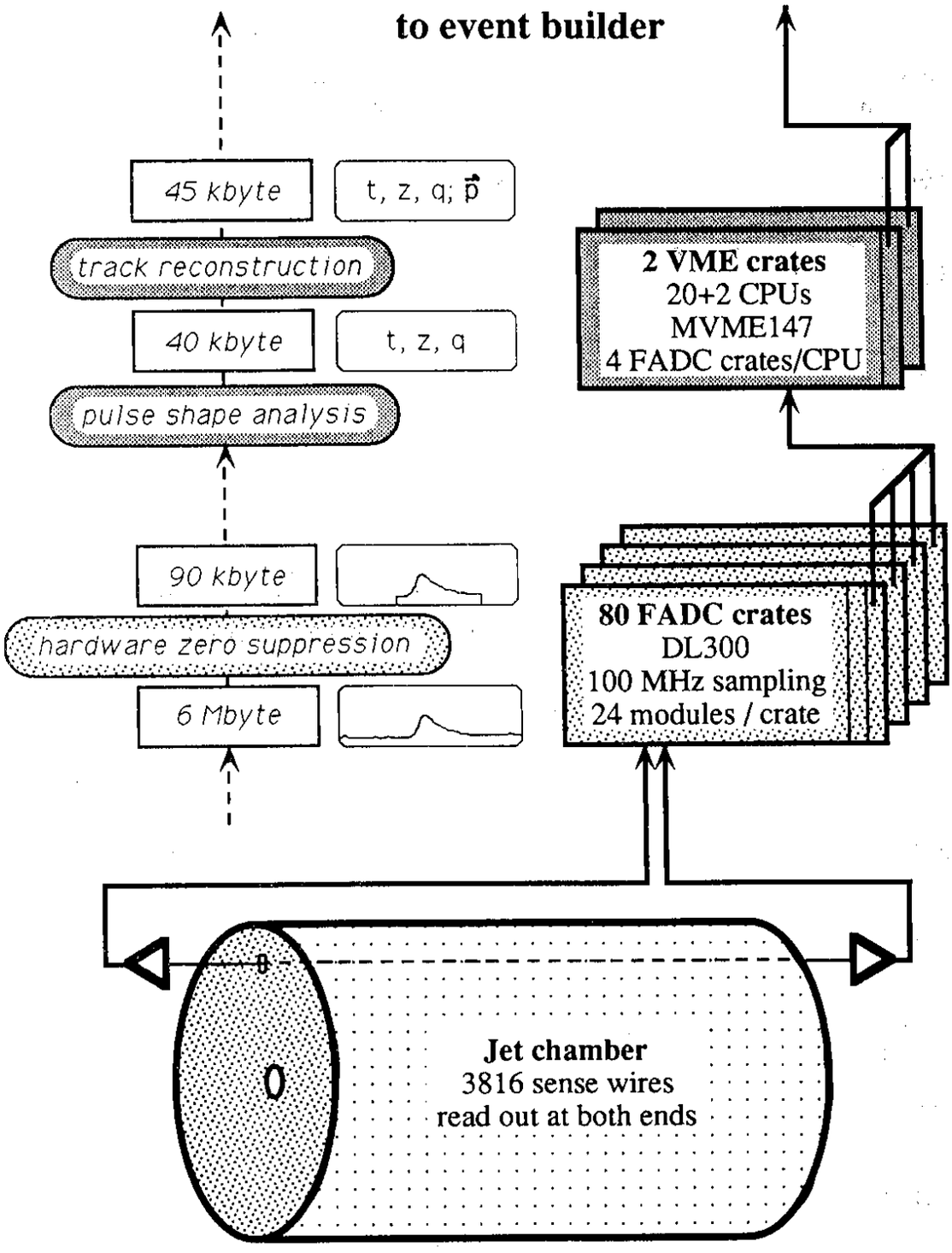

Fig. 8

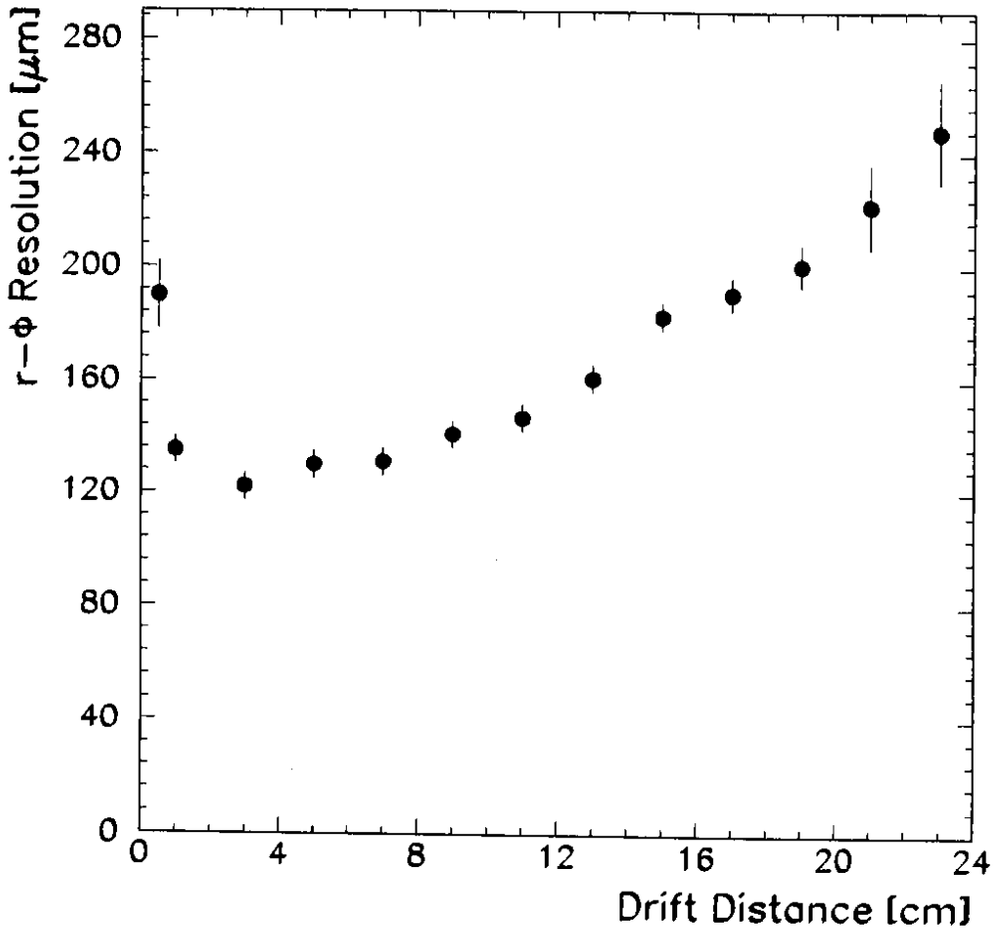
r−Φ Resolution [μm]
280
240
200
160
120
80
40
0
0
4
8
12
16
20
24
Drift Distance [cm]

Fig. 9

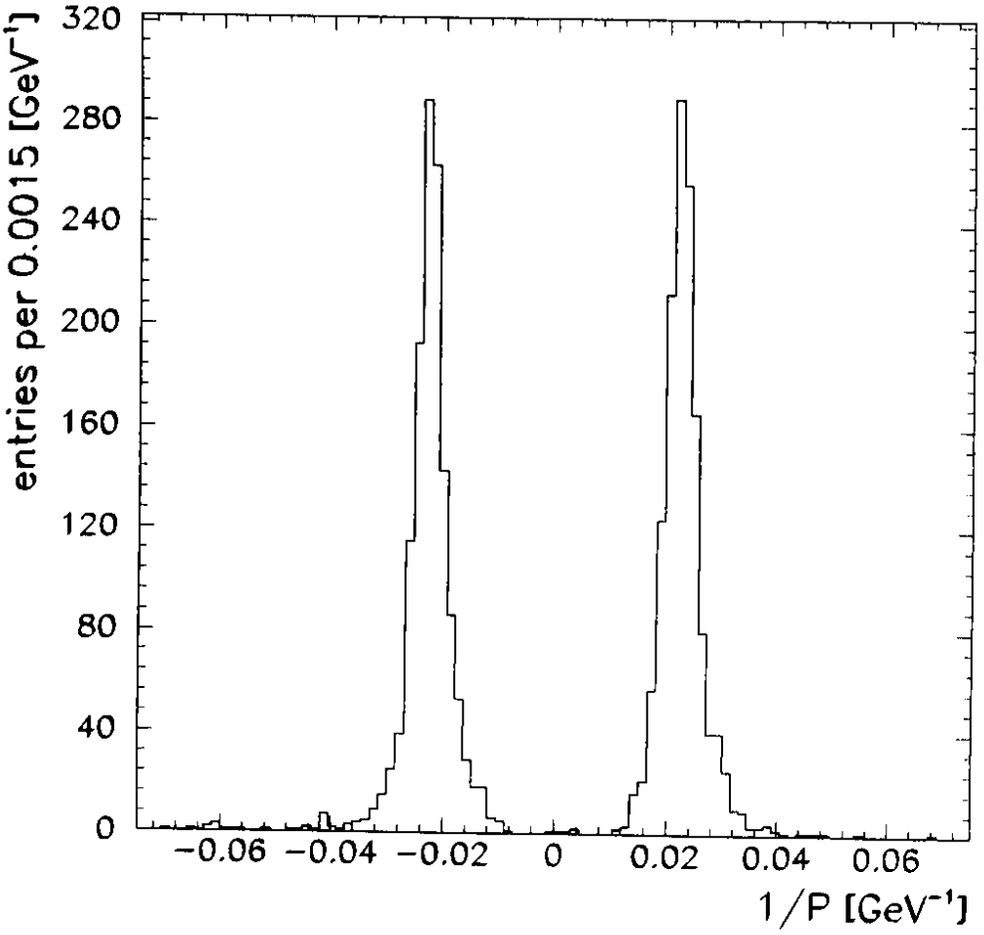
entries per 0.0015 [GeV⁻¹]
320
280
240
200
160
120
80
40
0
−0.06
−0.04
−0.02
0
0.02
0.04
0.06
1/P [GeV⁻¹]

Fig. 10

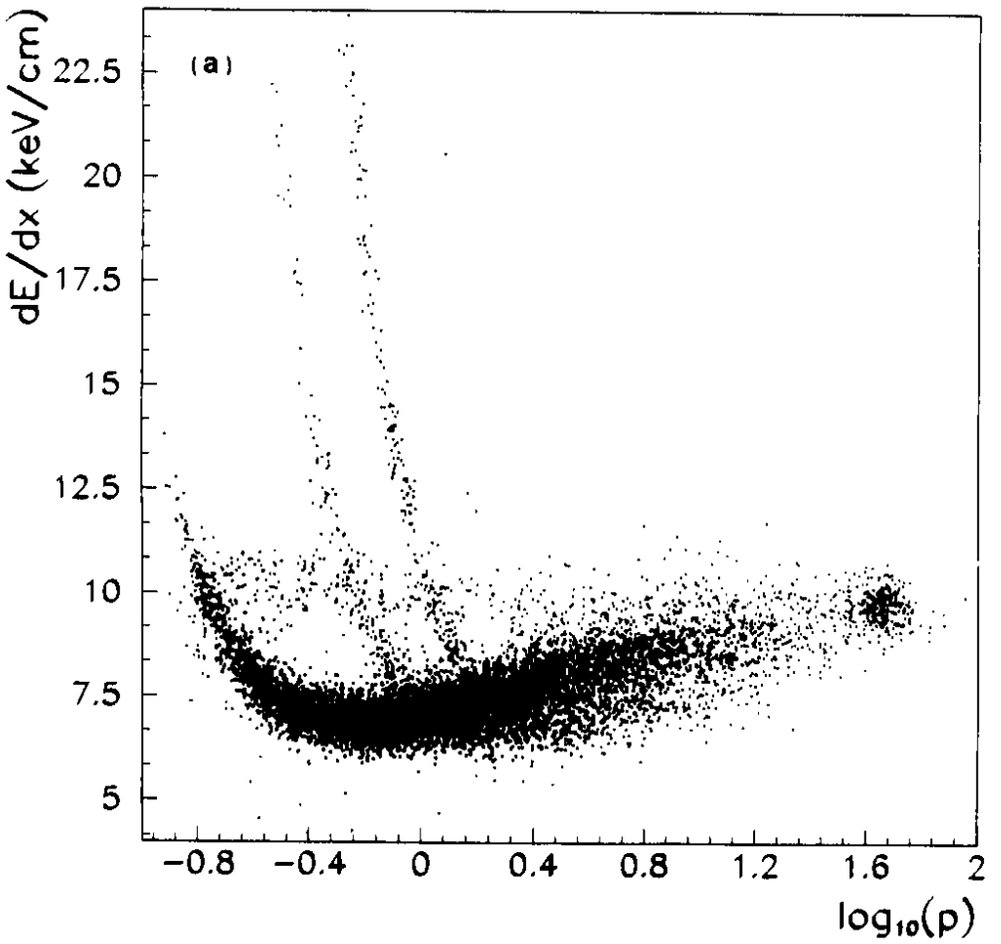
(a)
dE/dx (keV/cm)
22.5
20
17.5
15
12.5
10
7.5
5
−0.8
−0.4
0
0.4
0.8
1.2
1.6
2
log10(p)

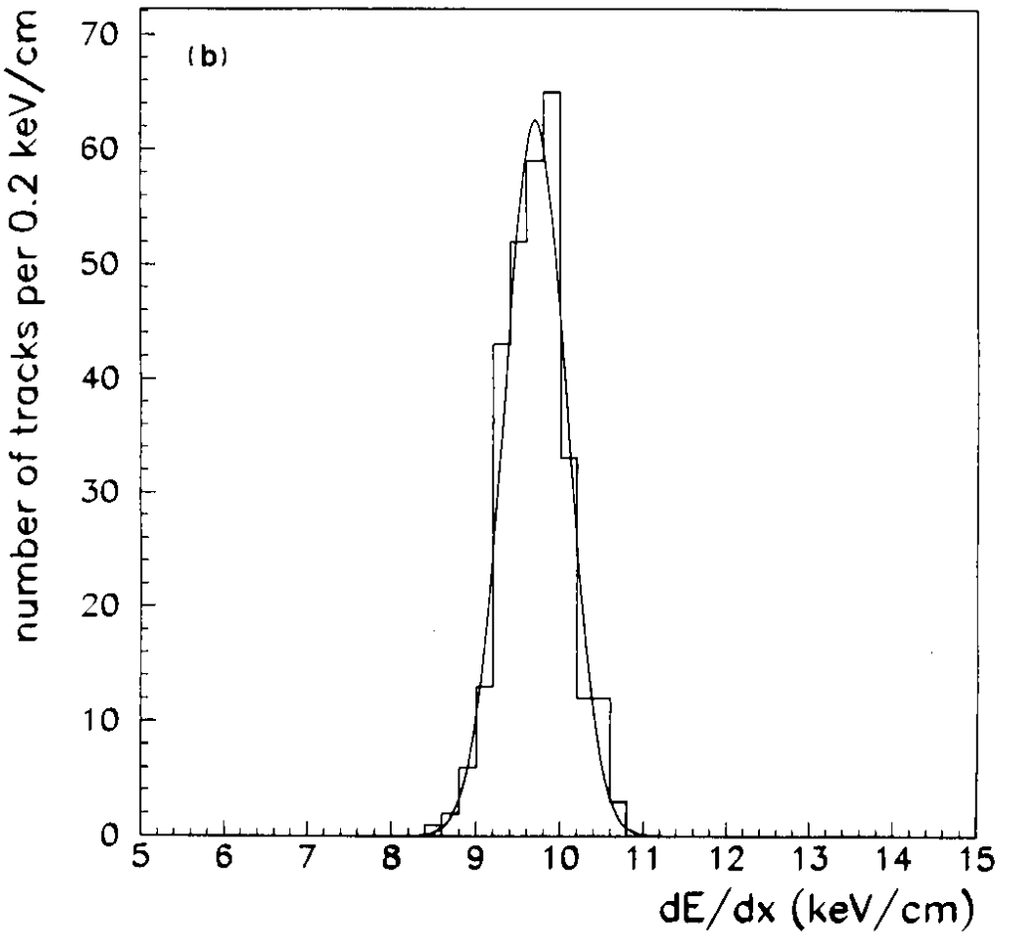
(b)
number of tracks per 0.2 keV/cm
70
60
50
40
30
20
10
0
5
6
7
8
9
10
11
12
13
14
15
dE/dx (keV/cm)

Fig. 11

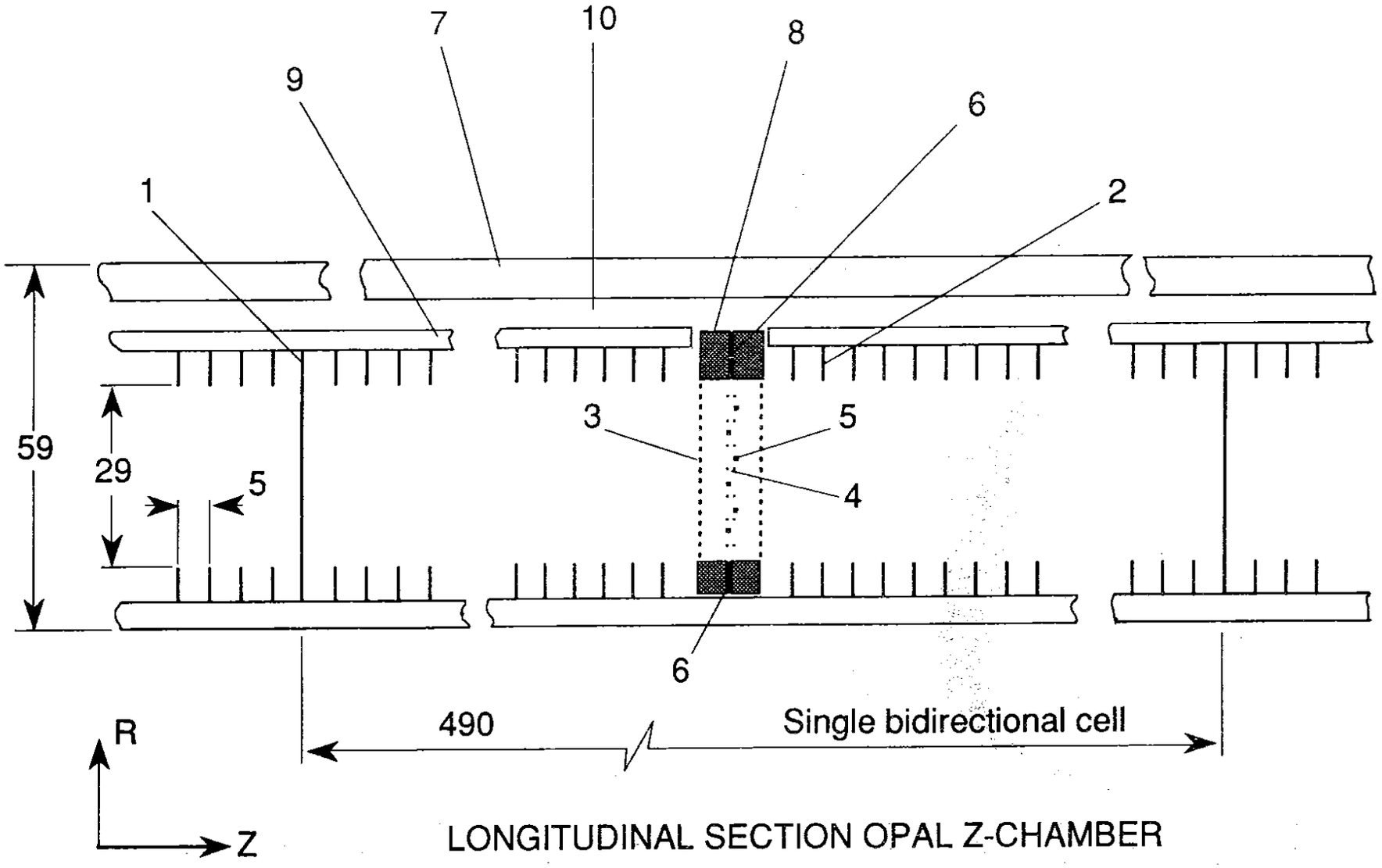
7
10
8
9
6
1
2
59
29
5
3
5
4
6
490
Single bidirectional cell
R
Z
LONGITUDINAL SECTION OPAL Z-CHAMBER

Fig. 12

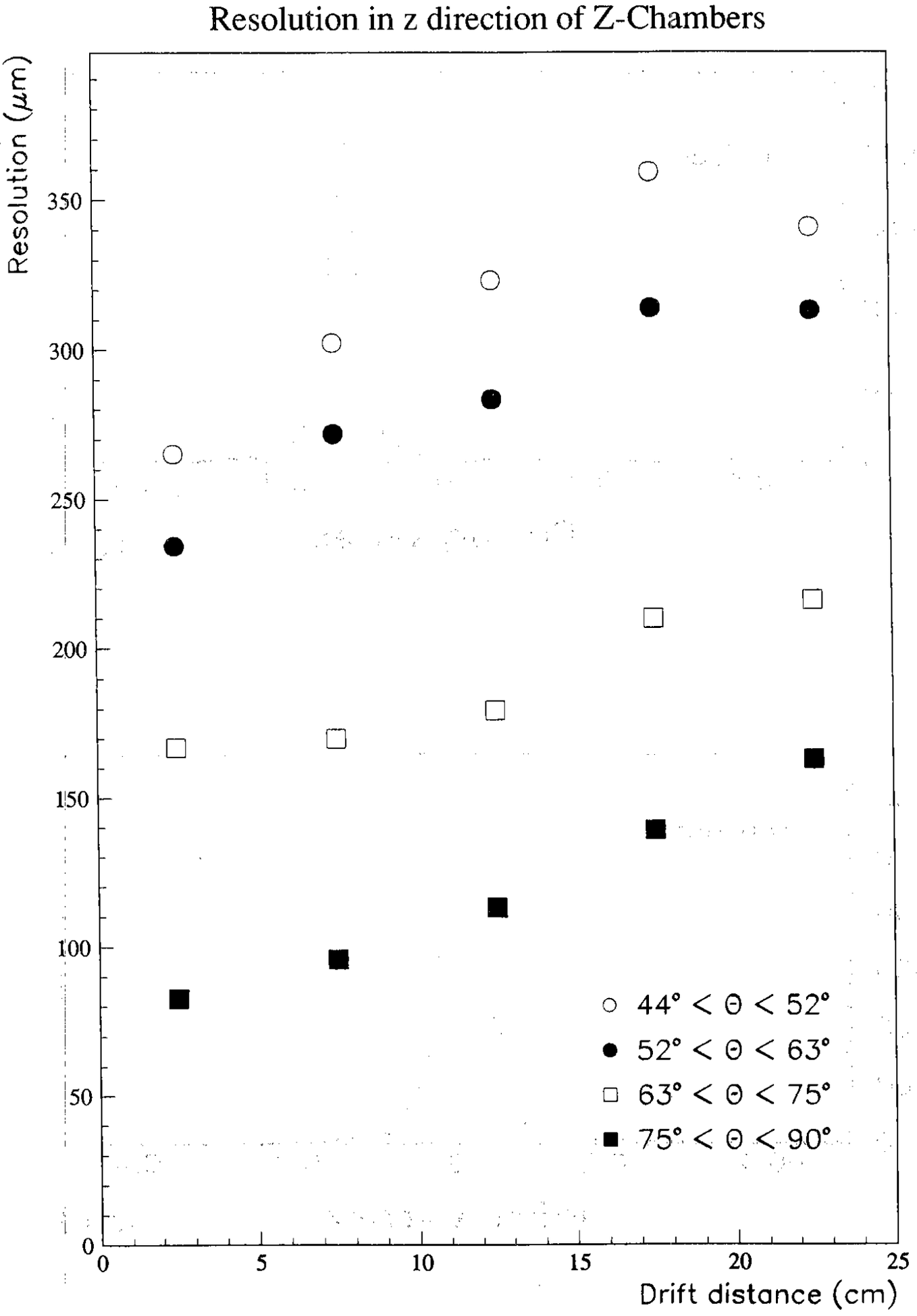
Resolution in z direction of Z-Chambers
Resolution (μm)
350
300
250
200
150
100
50
0
0
5
10
15
20
25
Drift distance (cm)
44° < Θ < 52°
52° < Θ < 63°
63° < Θ < 75°
75° < Θ < 90°

Fig. 13

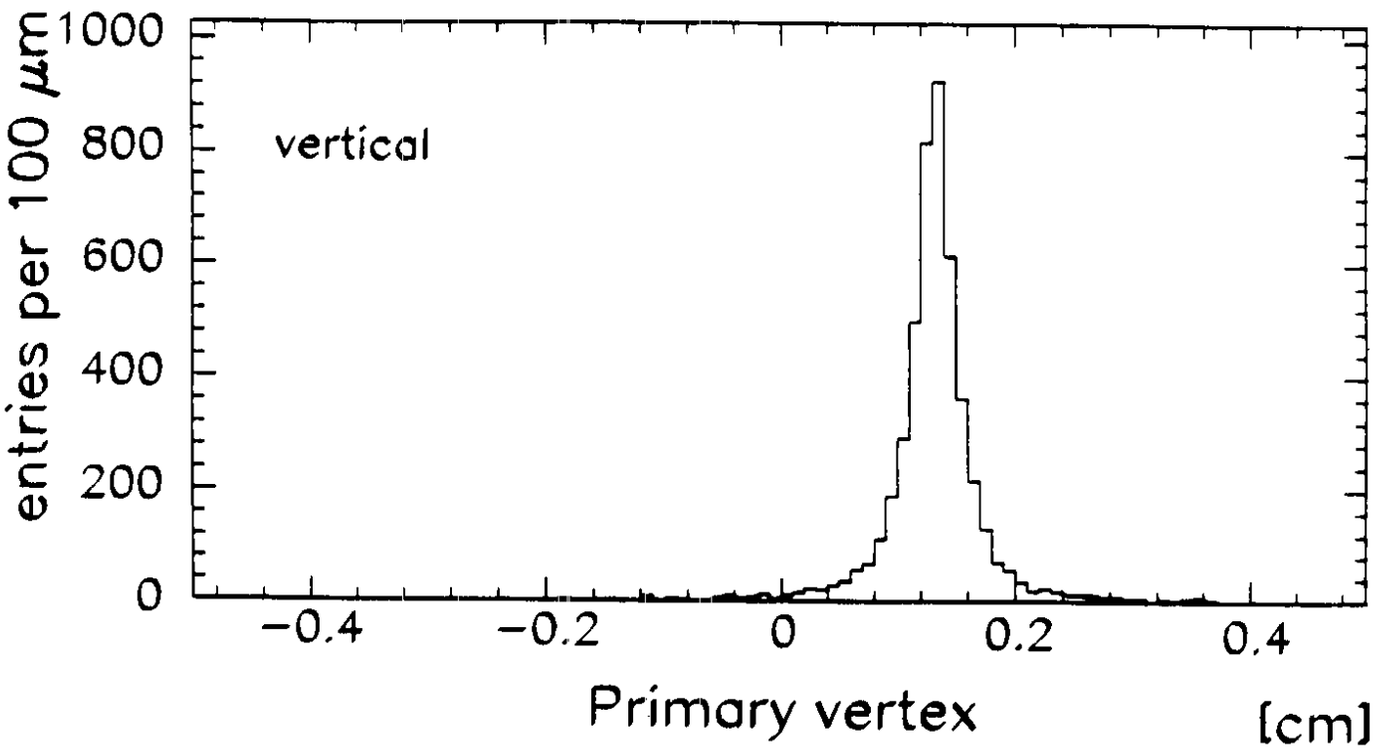
vertical
entries per 100 μm
1000
800
600
400
200
0
−0.4
−0.2
0
0.2
0.4
Primary vertex
[cm]

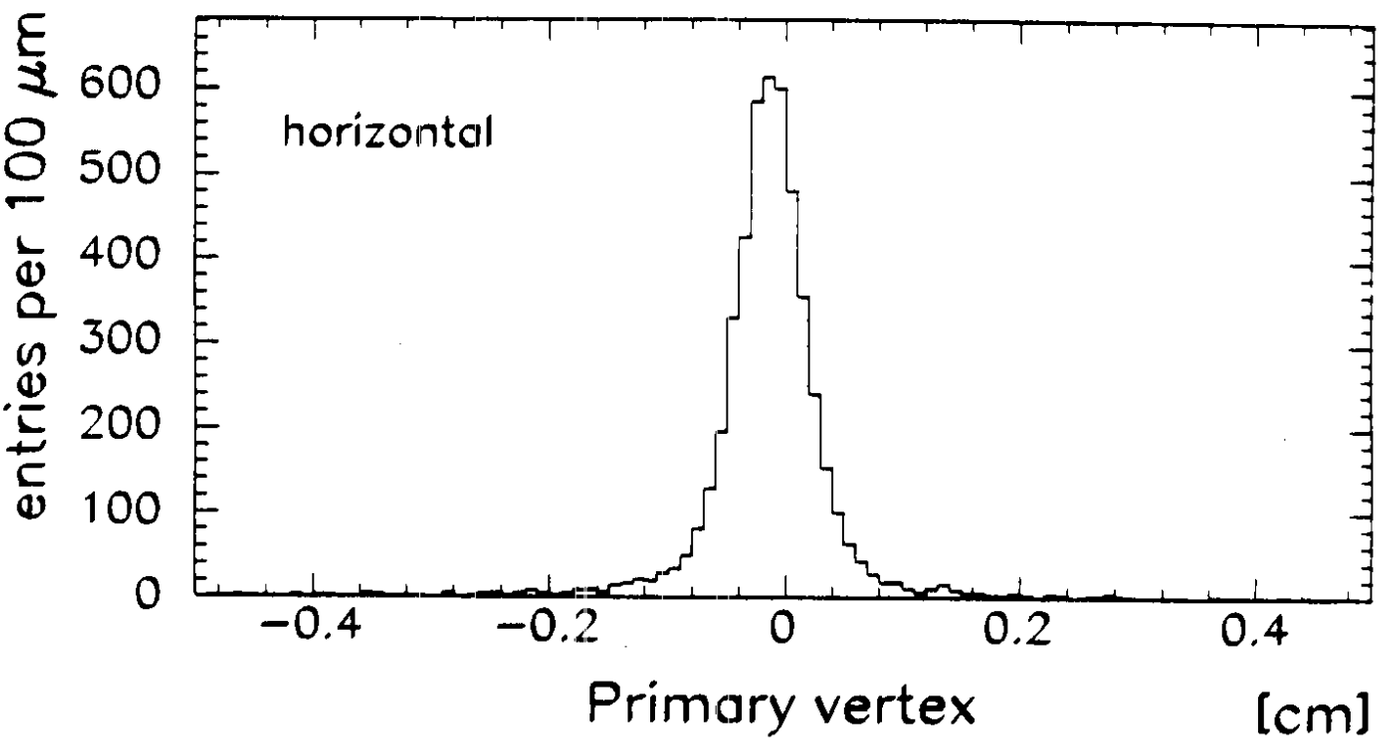
horizontal
entries per 100 μm
600
500
400
300
200
100
0
−0.4
−0.2
0
0.2
0.4
Primary vertex
[cm]

Fig. 14

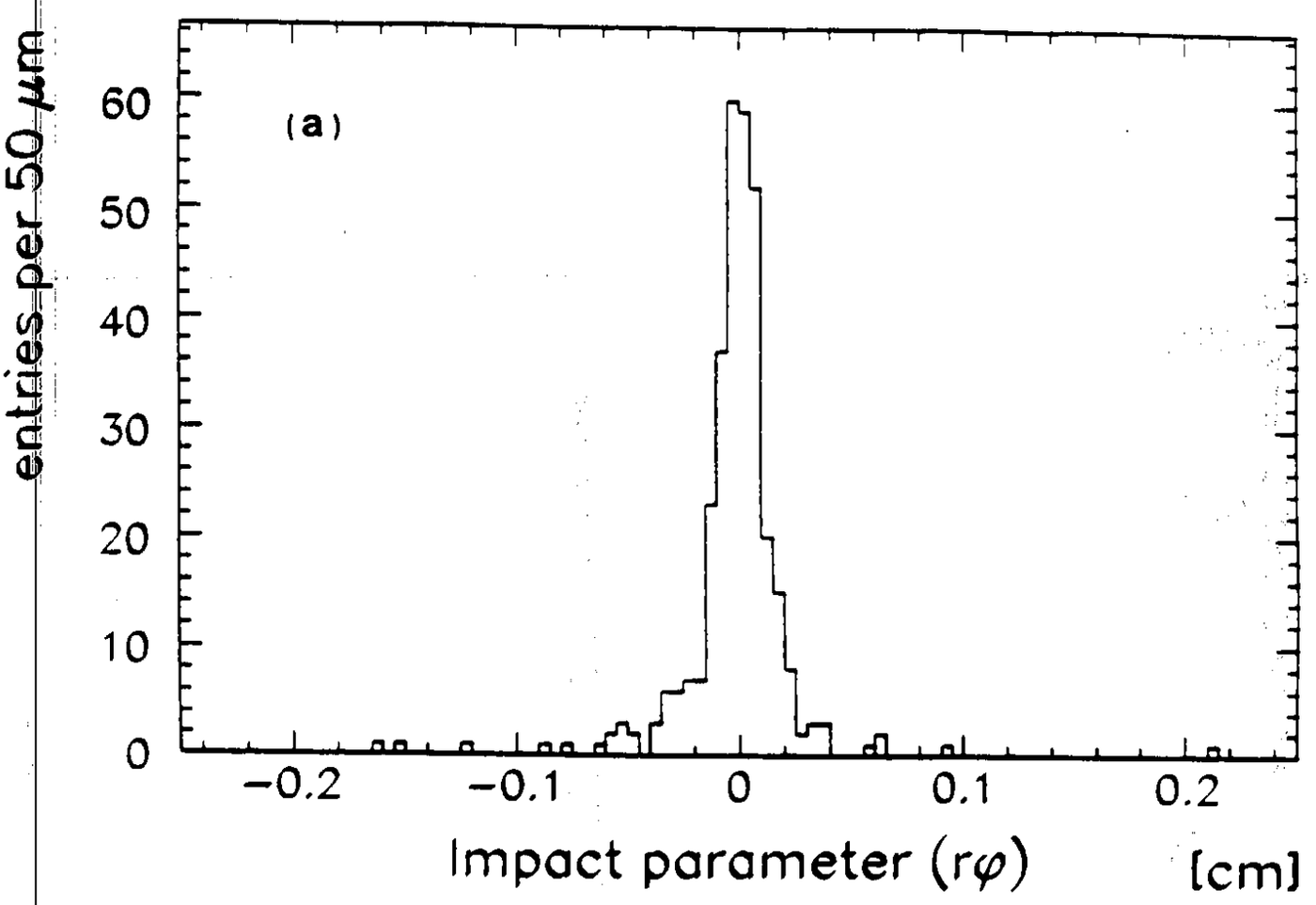
(a)
entries per 50 μm
60
50
40
30
20
10
0
−0.2
−0.1
0
0.1
0.2
Impact parameter (rφ)
[cm]

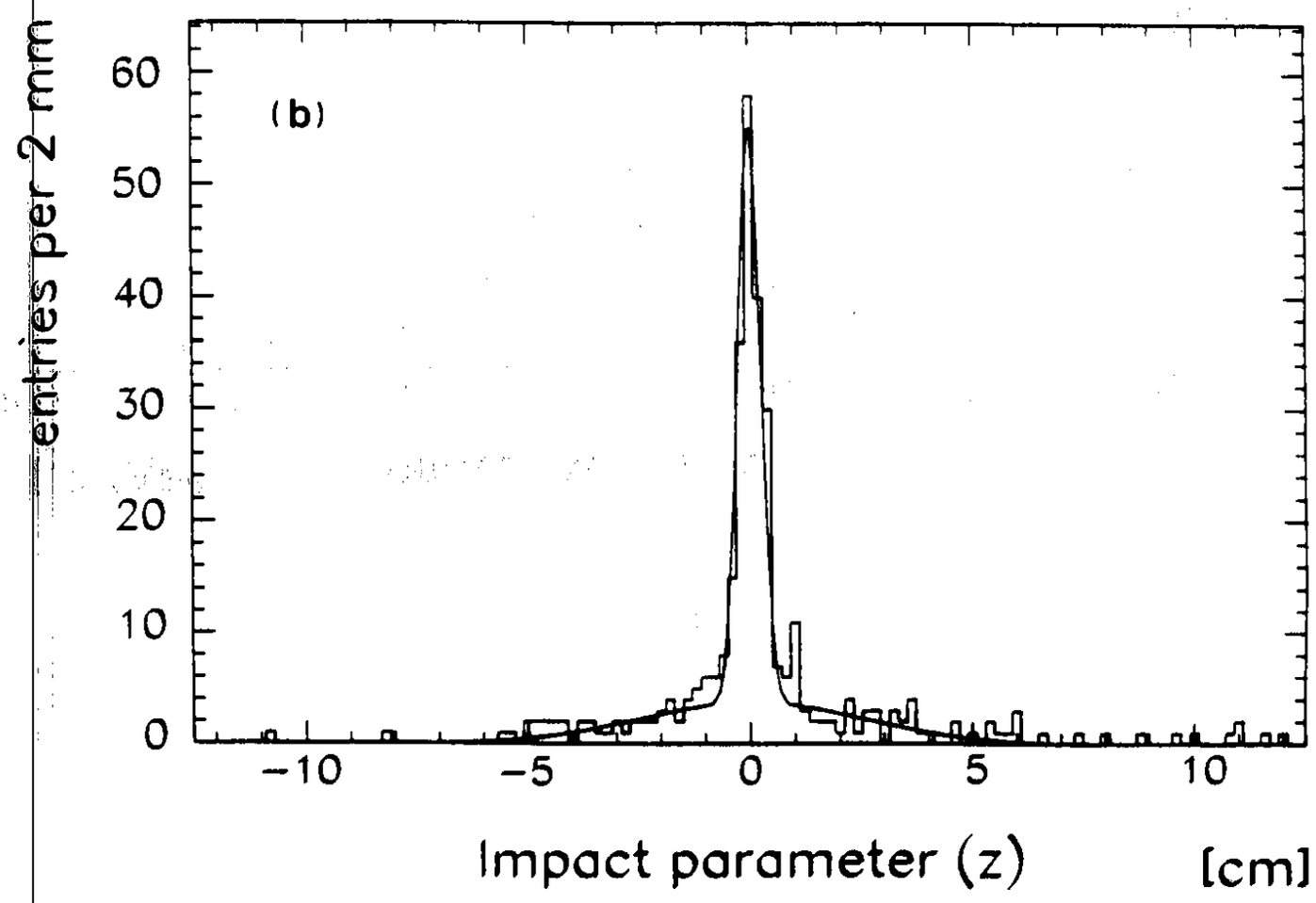
(b)
entries per 2 mm
60
50
40
30
20
10
0
−10
−5
0
5
10
Impact parameter (z)
[cm]

Fig. 15

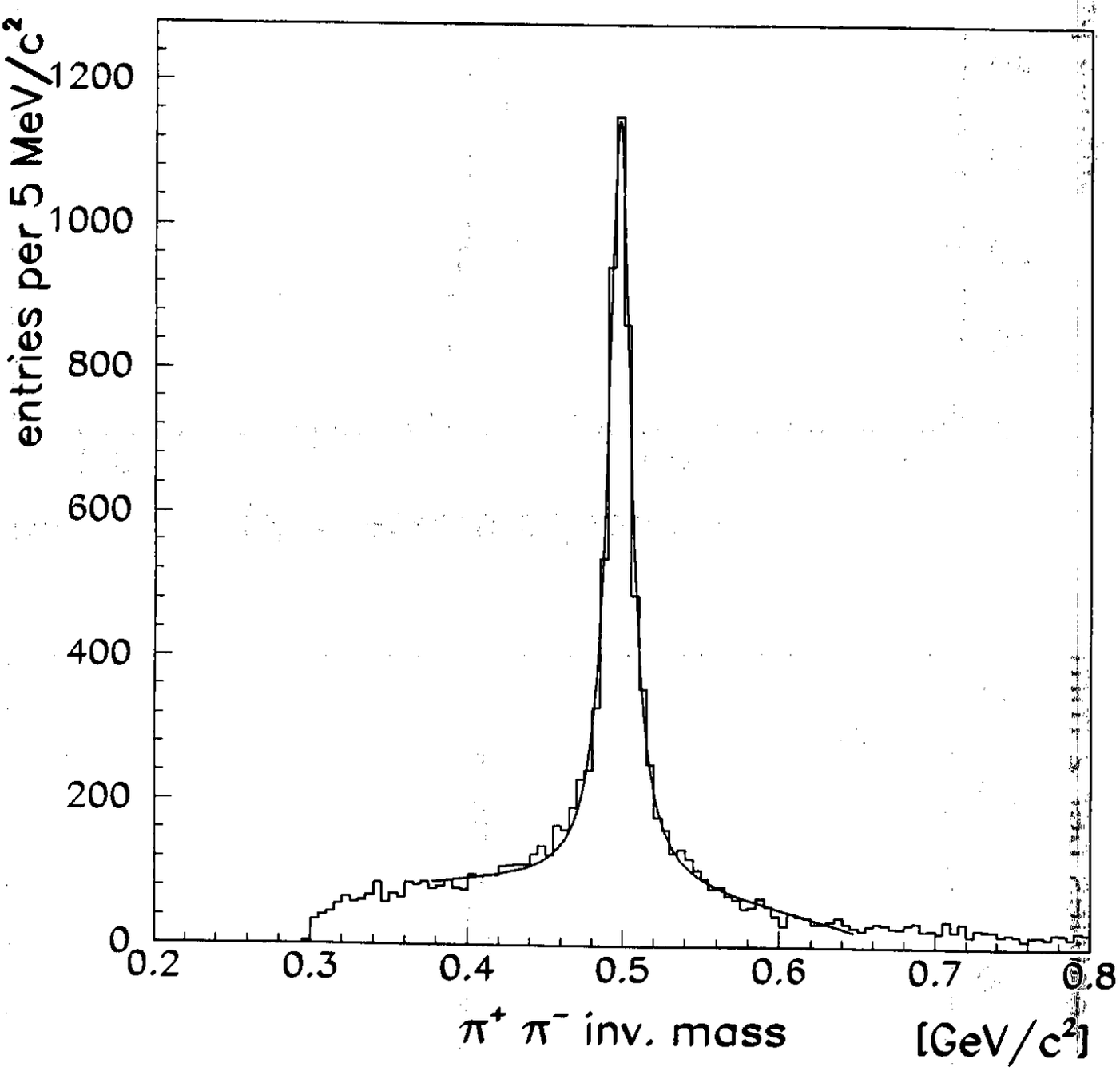
entries per 5 MeV/c²
1200
1000
800
600
400
200
0
0.2
0.3
0.4
0.5
0.6
0.7
0.8
π⁺ π⁻ inv. mass
[GeV/c²]

Fig. 16

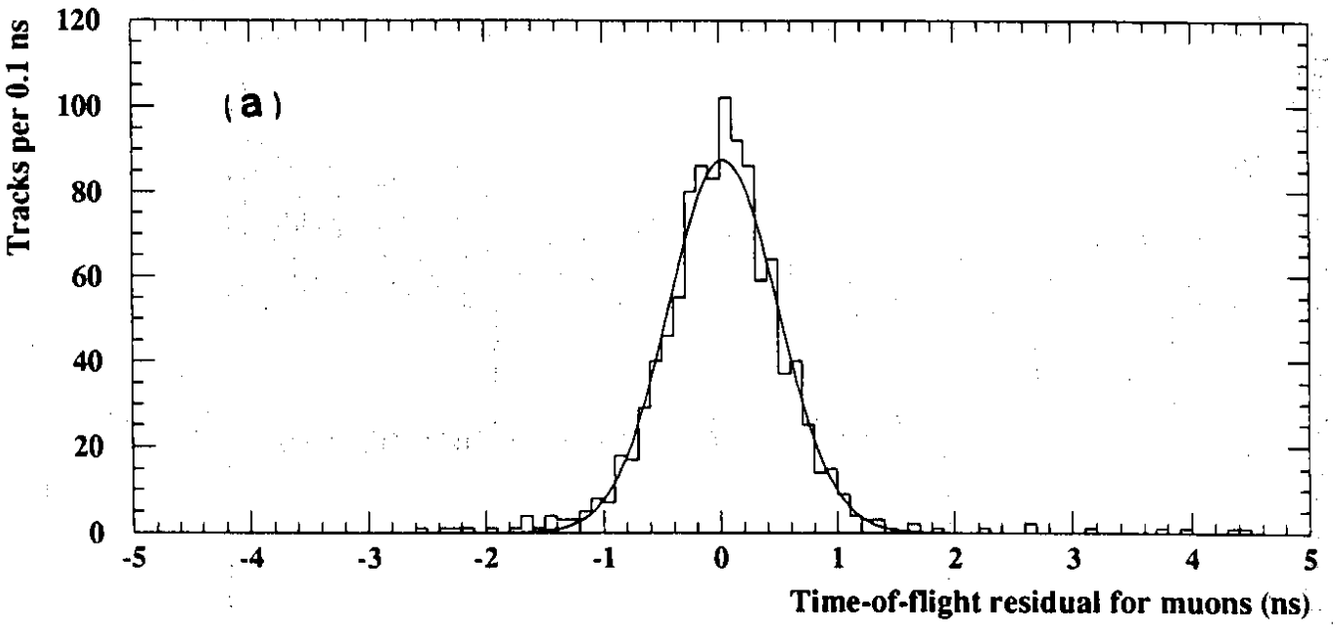
(a)
Tracks per 0.1 ns
120
100
80
60
40
20
0
-5
-4
-3
-2
-1
0
1
2
3
4
5
Time-of-flight residual for muons (ns)

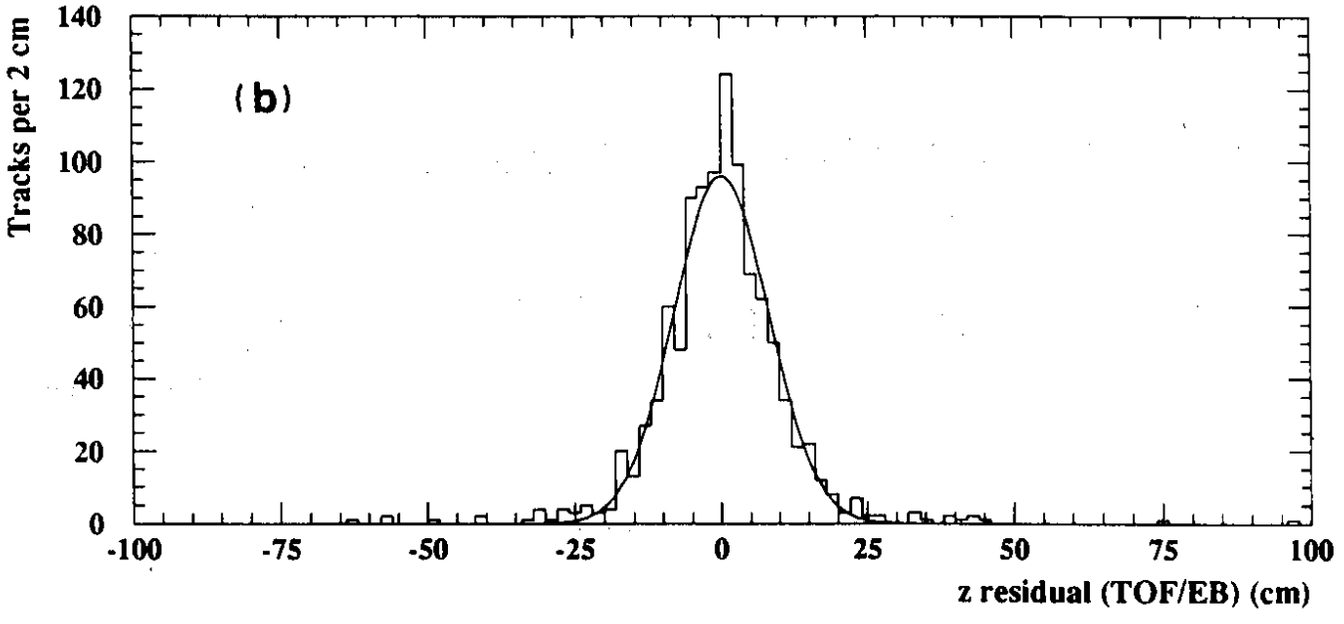
(b)
Tracks per 2 cm
140
120
100
80
60
40
20
0
-100
-75
-50
-25
0
25
50
75
100
z residual (TOF/EB) (cm)

Fig. 17

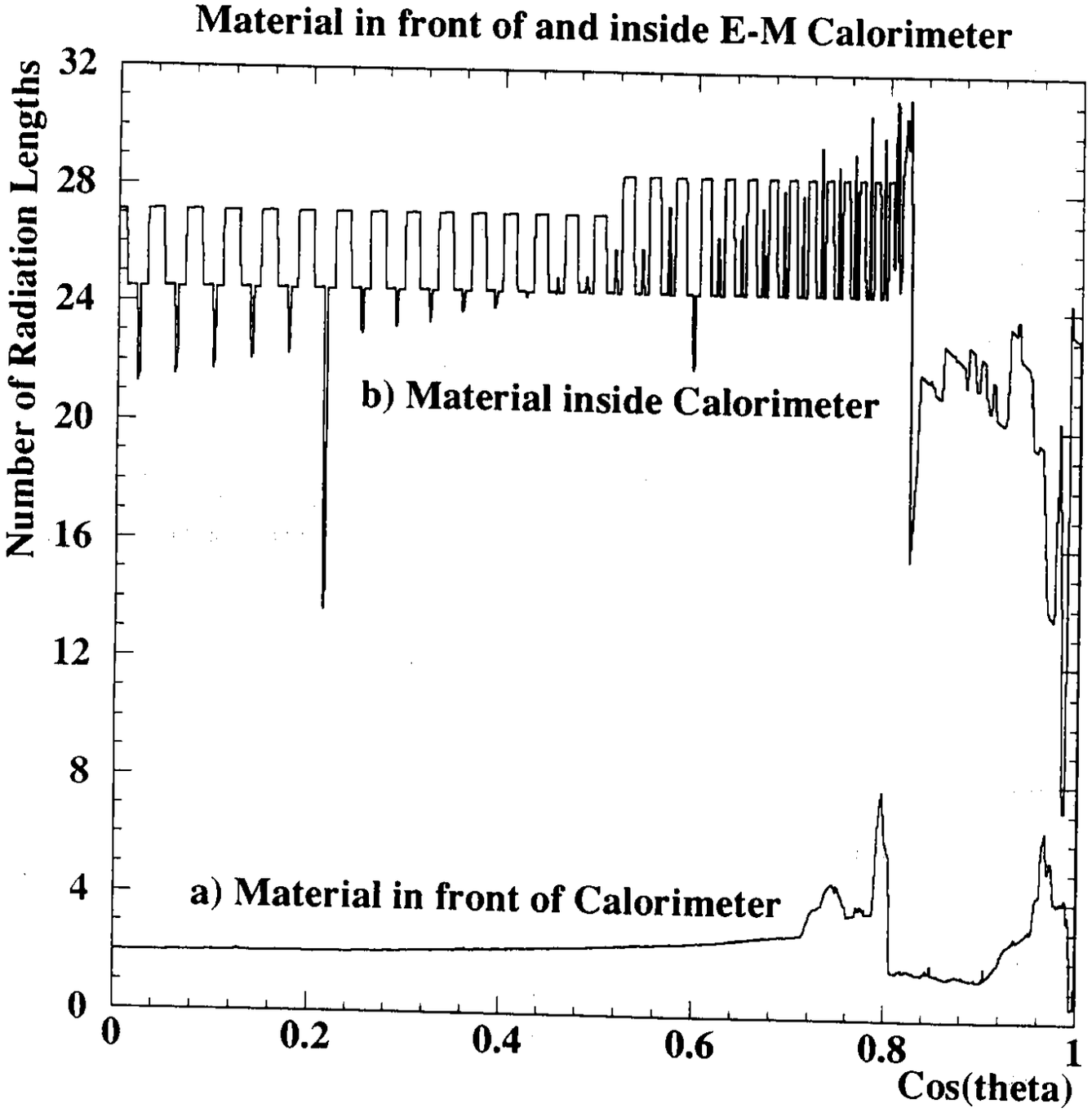
Material in front of and inside E-M Calorimeter
Number of Radiation Lengths
32
28
24
20
16
12
8
4
0
b) Material inside Calorimeter
a) Material in front of Calorimeter
0
0.2
0.4
0.6
0.8
1
Cos(theta)

Fig. 18

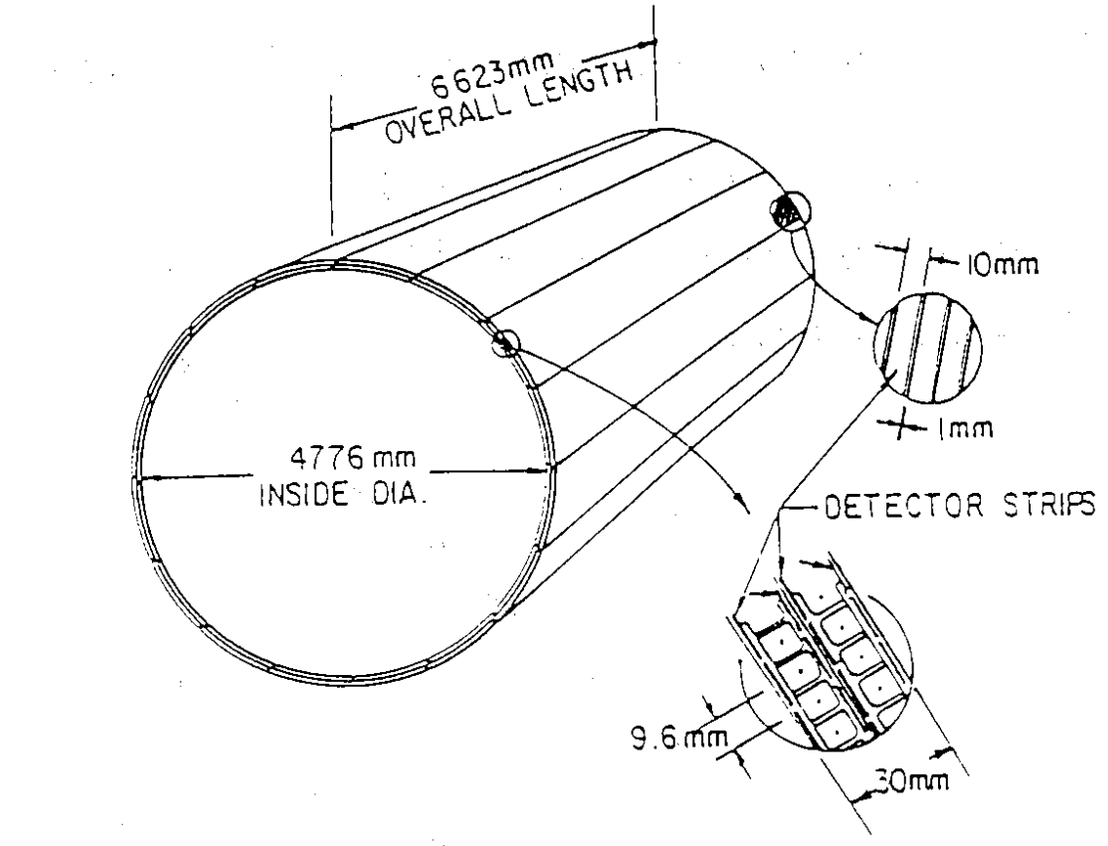
6623mm
OVERALL LENGTH
10mm
1mm
4776 mm
INSIDE DIA.
DETECTOR STRIPS
9.6 mm
30mm

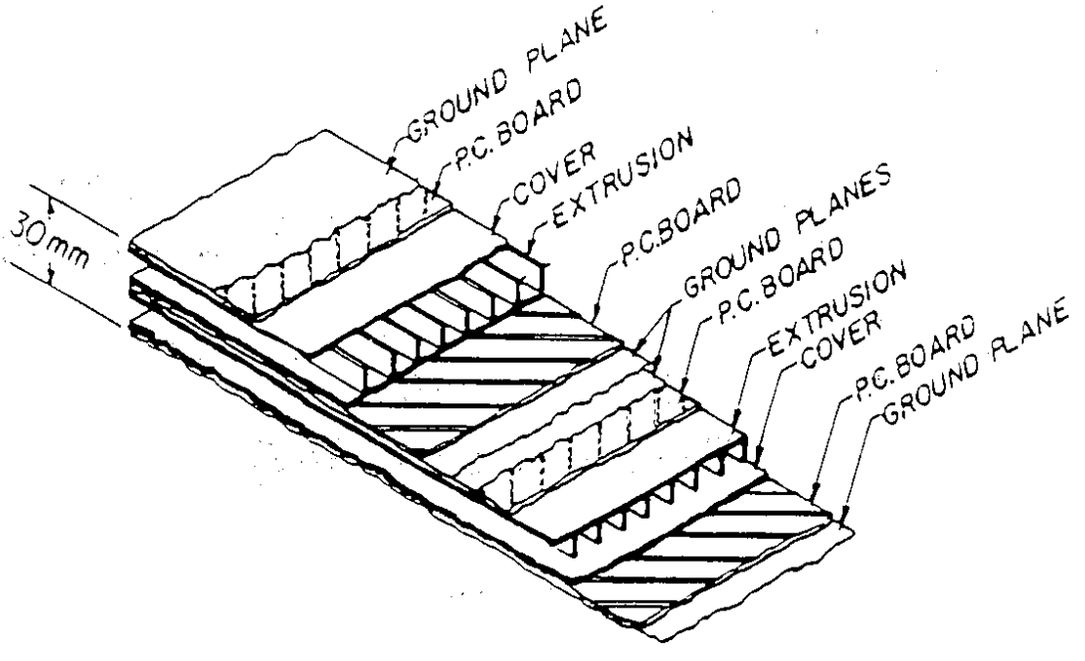
GROUND PLANE
P.C. BOARD
COVER
EXTRUSION
P.C.BOARD
GROUND PLANES
P.C. BOARD
EXTRUSION
COVER
P.C. BOARD
GROUND PLANE
30mm

Fig. 19

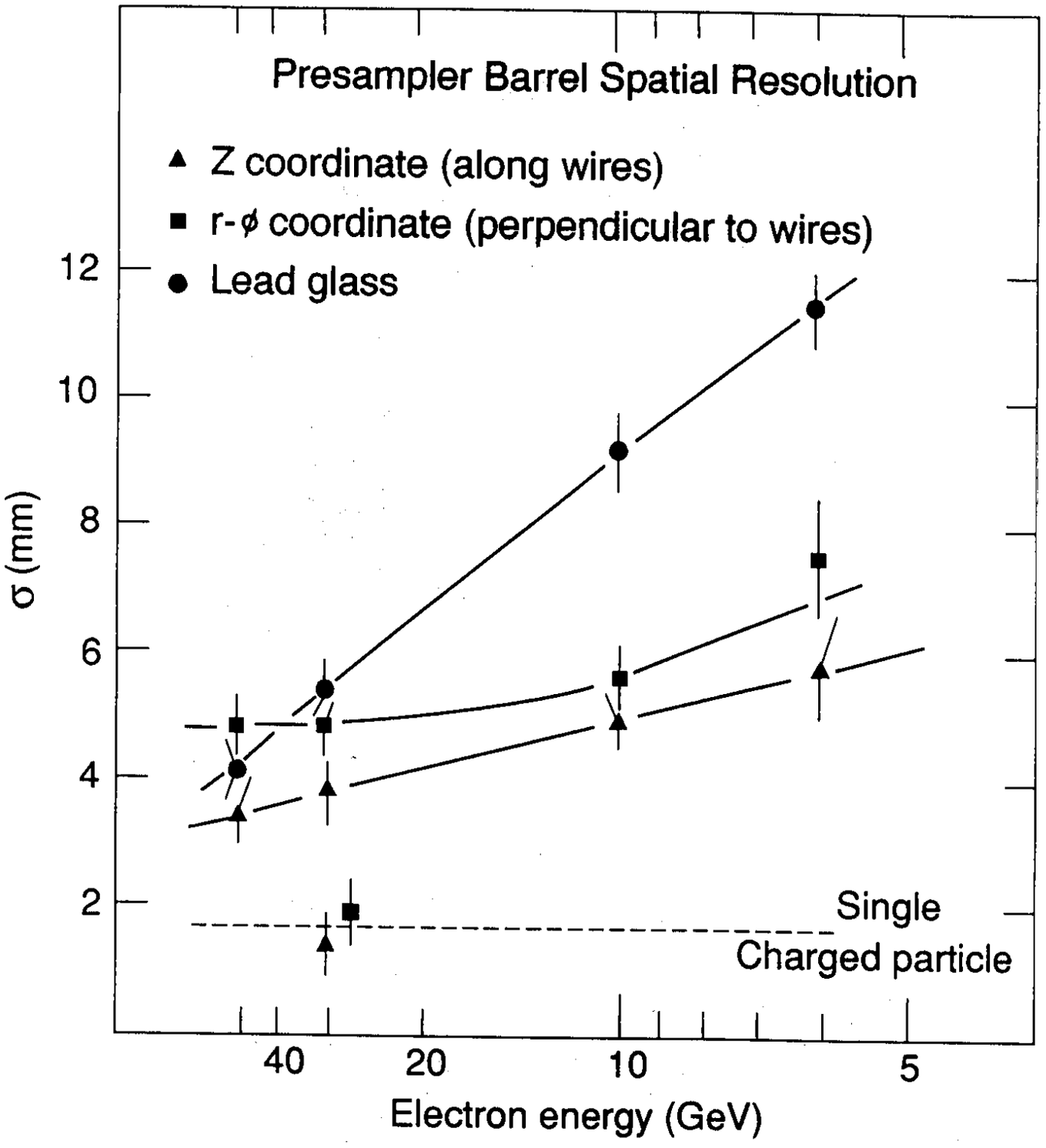
Presampler Barrel Spatial Resolution
Z coordinate (along wires)
r-ϕ coordinate (perpendicular to wires)
Lead glass
σ (mm)
12
10
8
6
4
2
Single
Charged particle
40
20
10
5
Electron energy (GeV)

Fig. 20

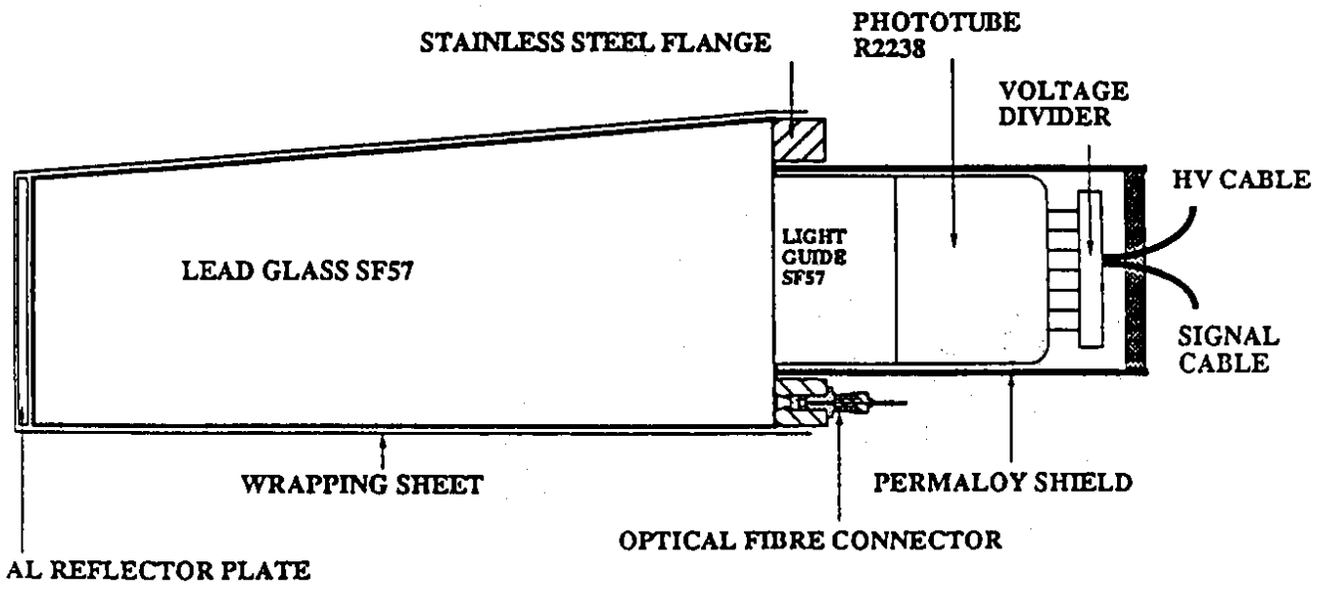

LEADGLASS ASSEMBLY OF BARREL ELECTROMAGNETIC CALORIMETER

Fig. 21

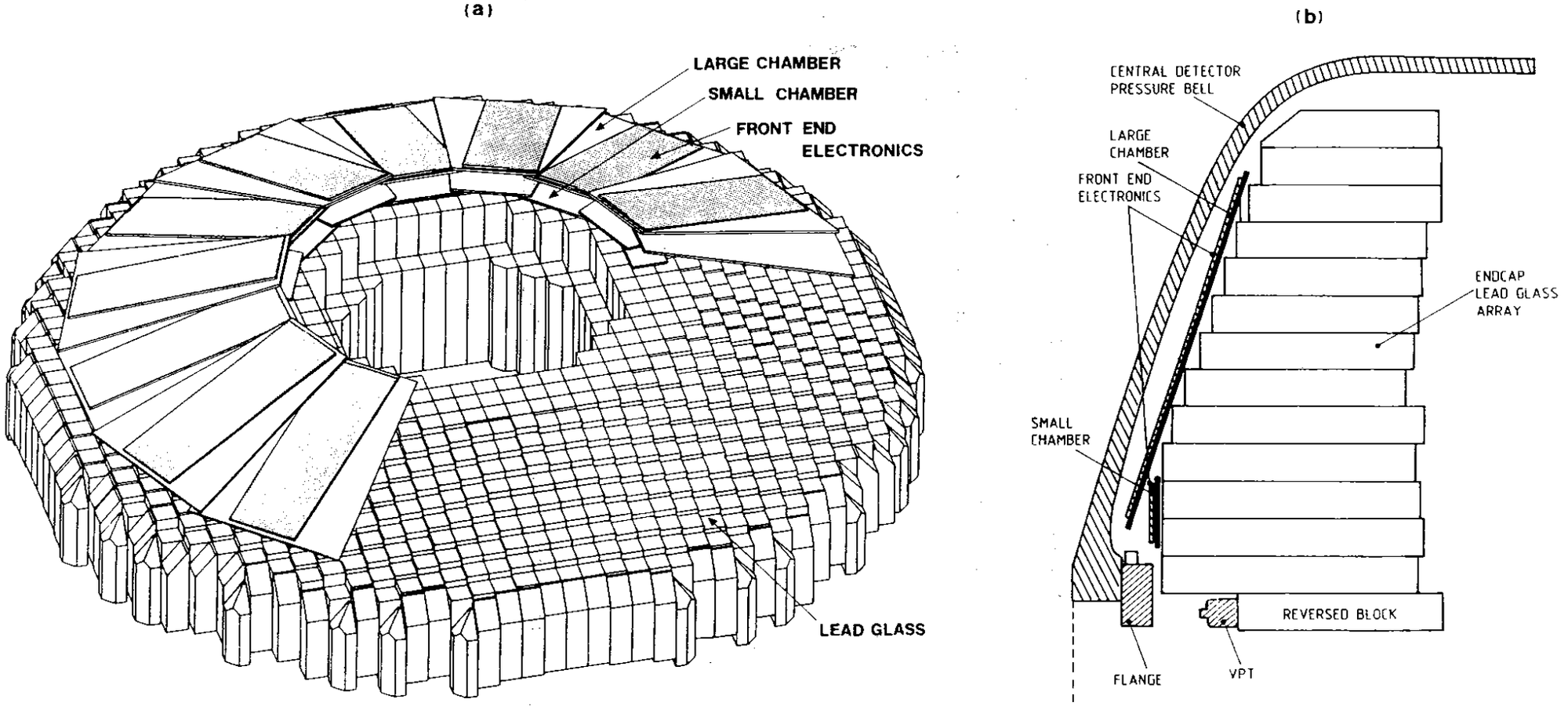
(a)
LARGE CHAMBER
SMALL CHAMBER
FRONT END
ELECTRONICS
LEAD GLASS
(b)
CENTRAL DETECTOR
PRESSURE BELL
LARGE
CHAMBER
FRONT END
ELECTRONICS
ENDCAP
LEAD GLASS
ARRAY
SMALL
CHAMBER
REVERSED BLOCK
FLANGE
VPT

Fig. 22

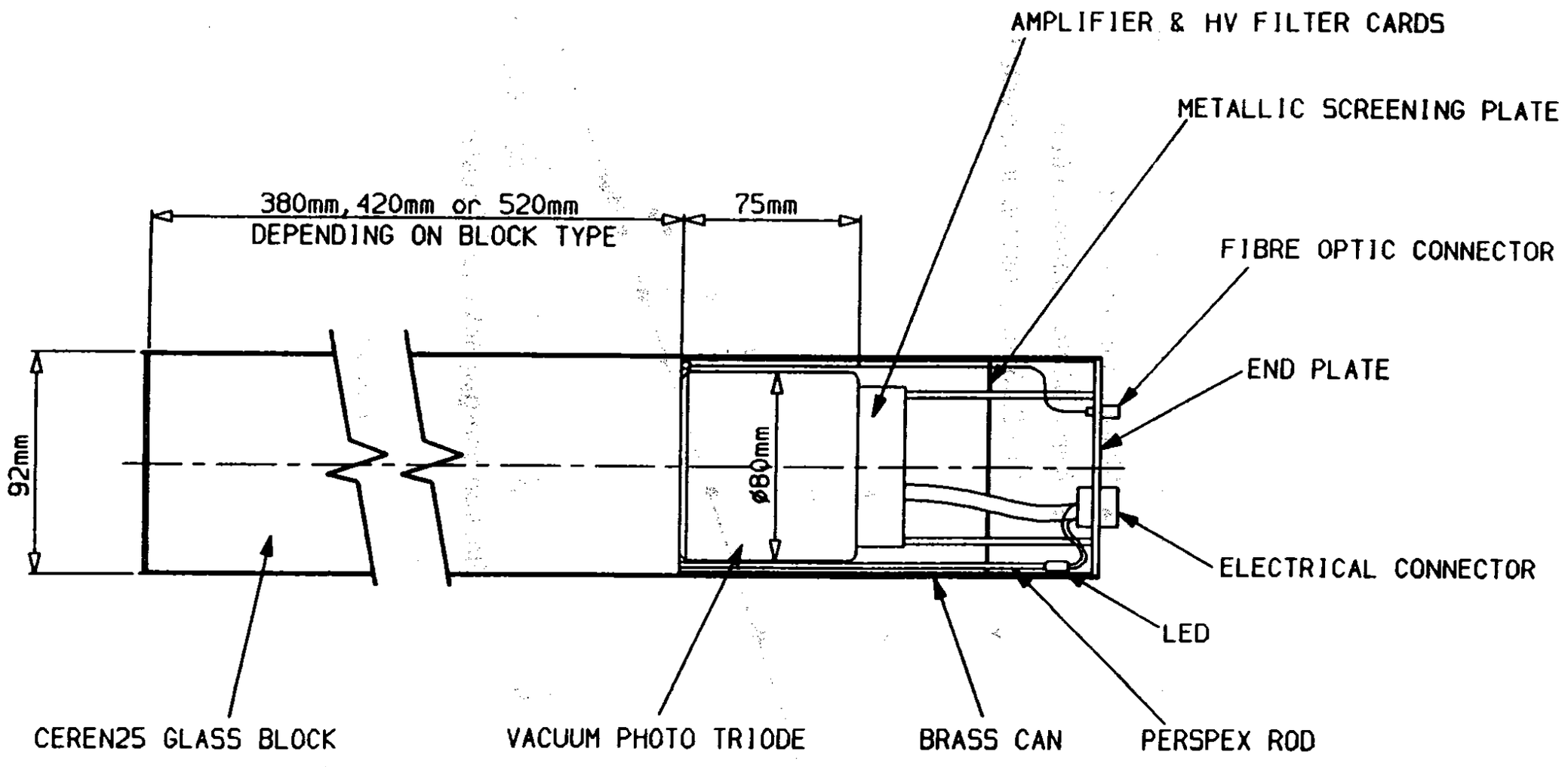

LEADGLASS ASSEMBLY OF ENDCAP ELECTROMAGNETIC CALORIMETER

Fig. 23

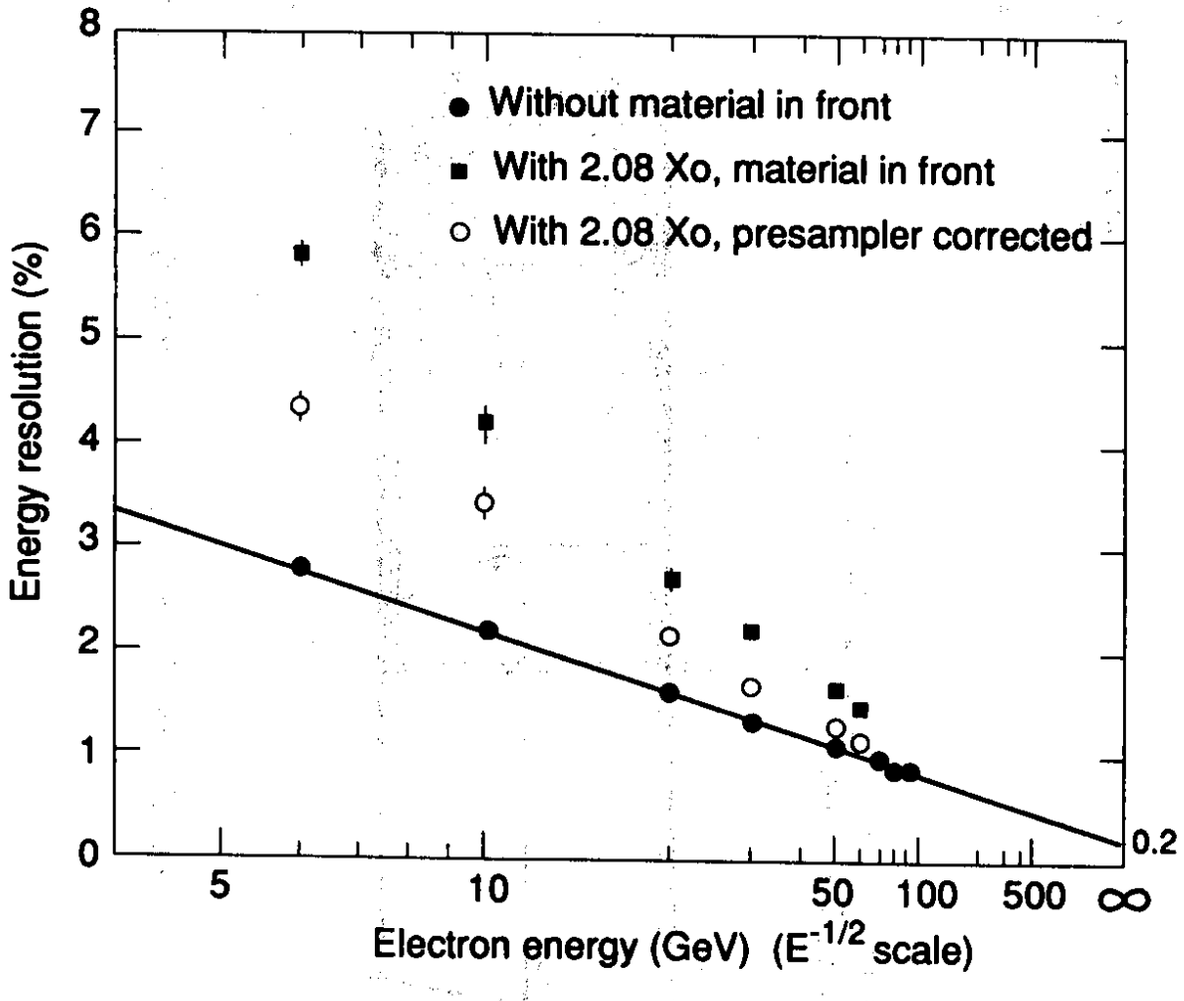
Without material in front
With 2.08 Xo, material in front
With 2.08 Xo, presampler corrected
Energy resolution (%)
Electron energy (GeV) (E^-1/2 scale)
0
1
2
3
4
5
6
7
8
5
10
50
100
500
∞
0.2

Fig. 24

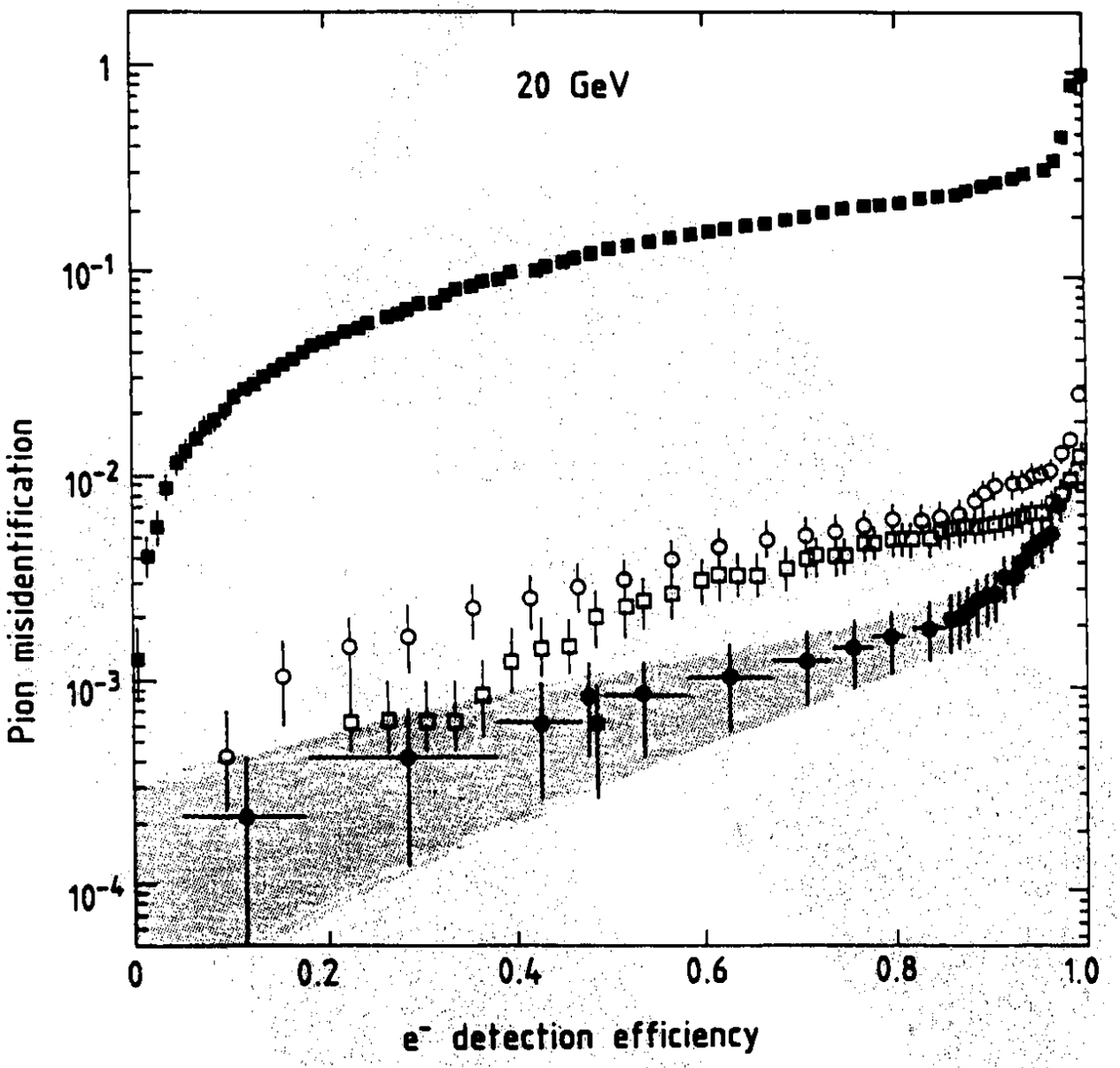
20 GeV
Pion misidentification
1
10^{-1}
10^{-2}
10^{-3}
10^{-4}
0
0.2
0.4
0.6
0.8
1.0
e^- detection efficiency

Fig. 25

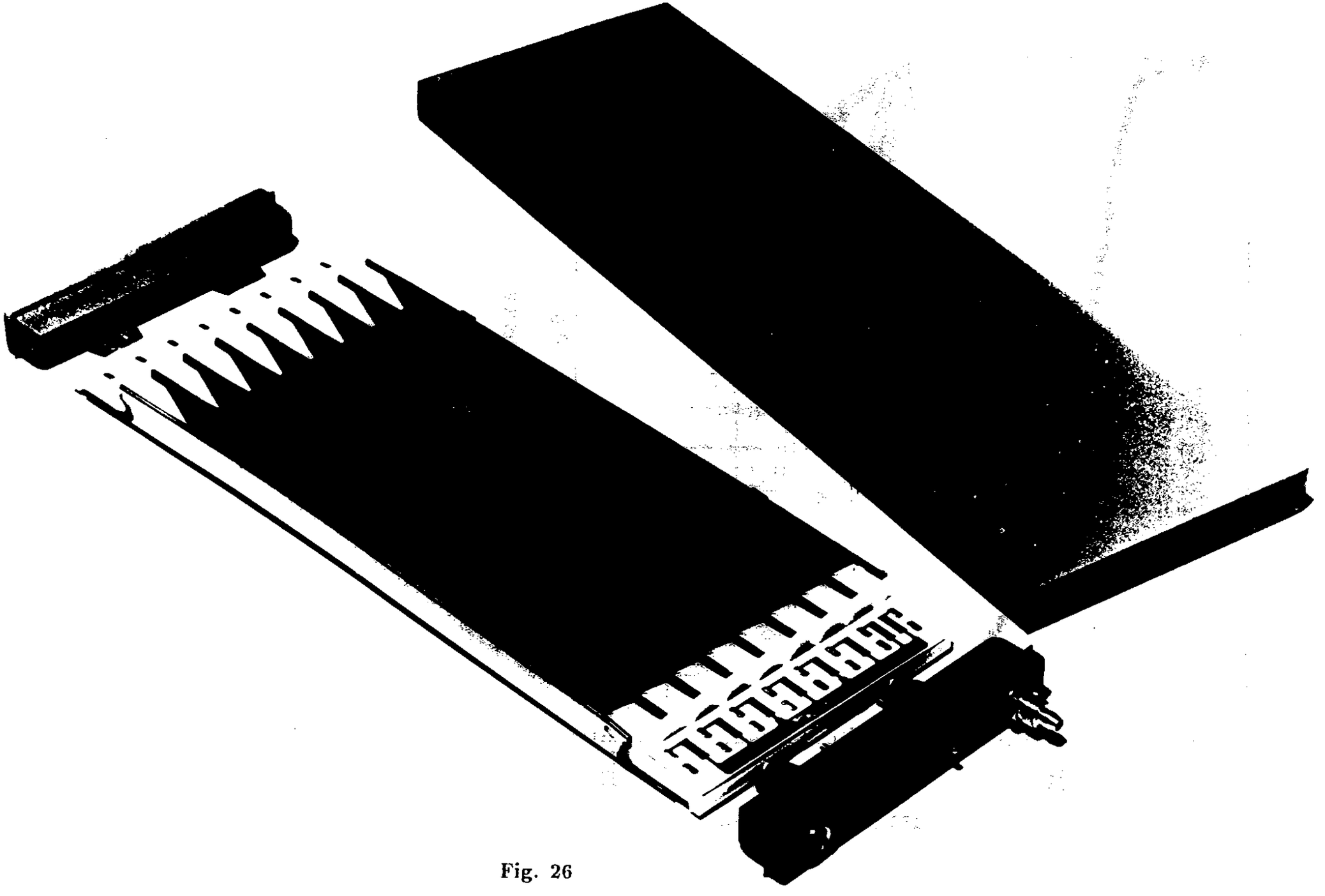

Fig. 26

Layout of barrel and Endcap hadron calorimeter

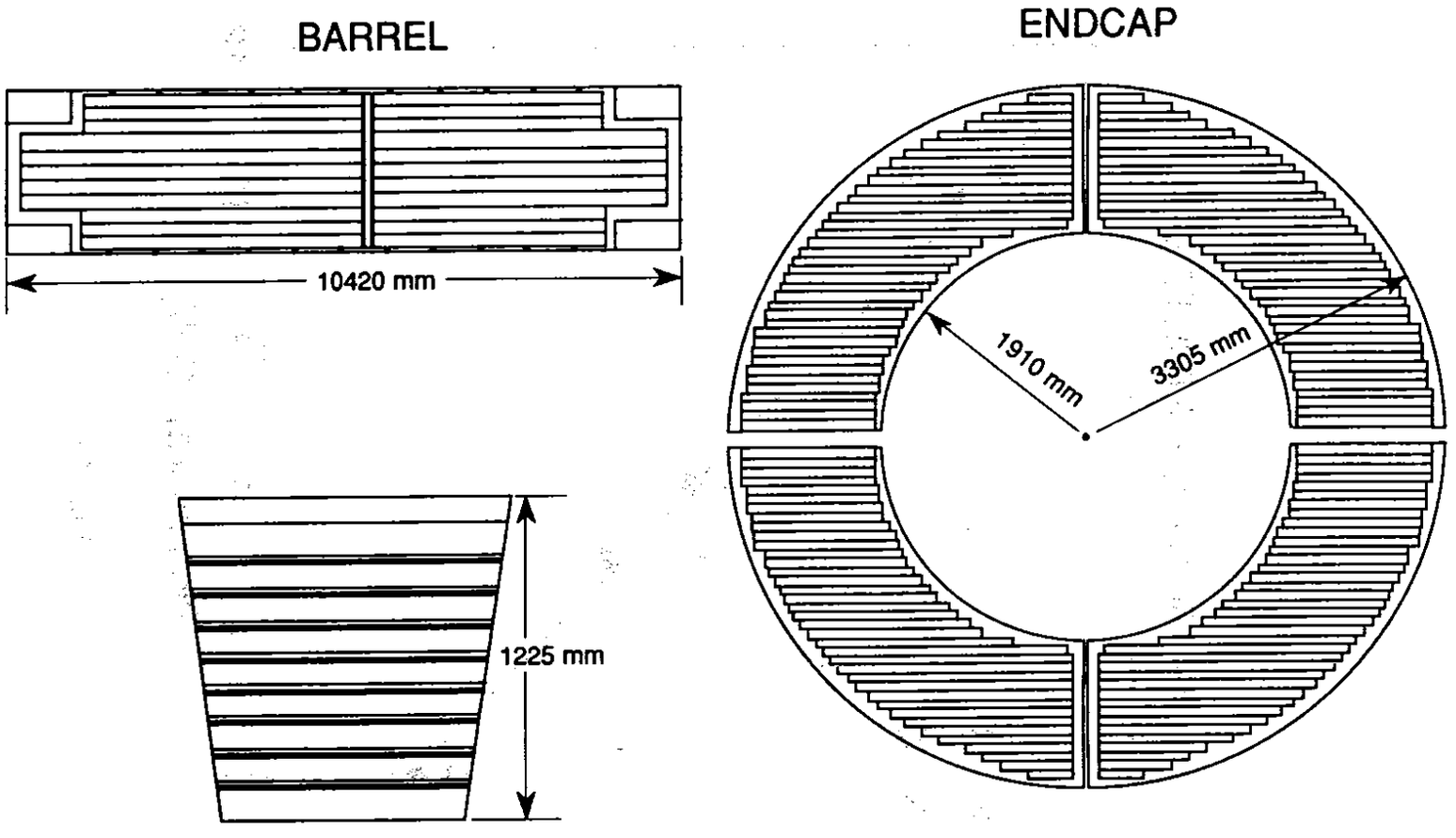

Fig. 27

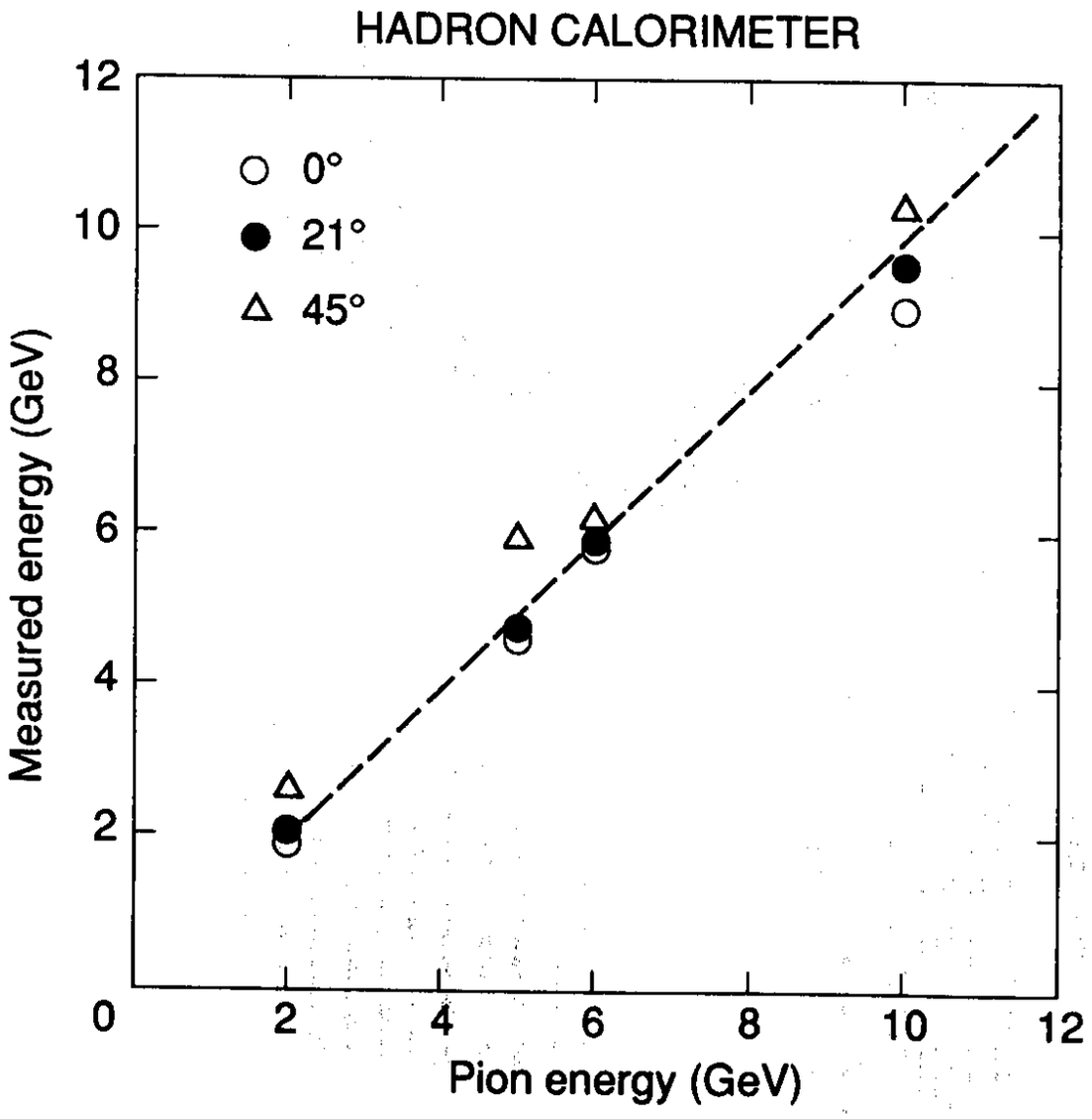
HADRON CALORIMETER
0°
21°
45°
Measured energy (GeV)
Pion energy (GeV)
0
2
4
6
8
10
12

Fig. 28

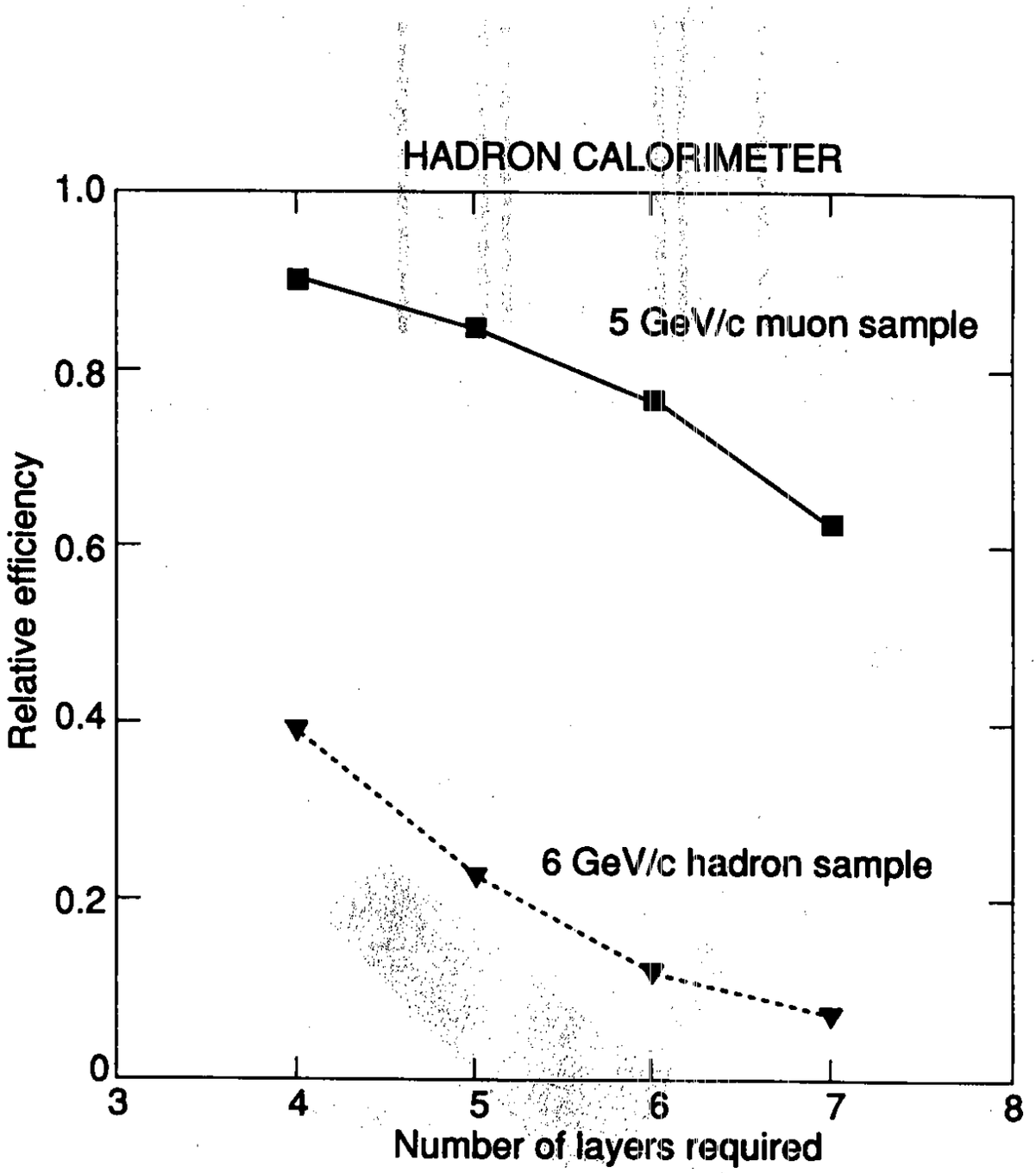
HADRON CALORIMETER
1.0
0.8
0.6
0.4
0.2
0
Relative efficiency
5 GeV/c muon sample
6 GeV/c hadron sample
3
4
5
6
7
8
Number of layers required

Fig. 29

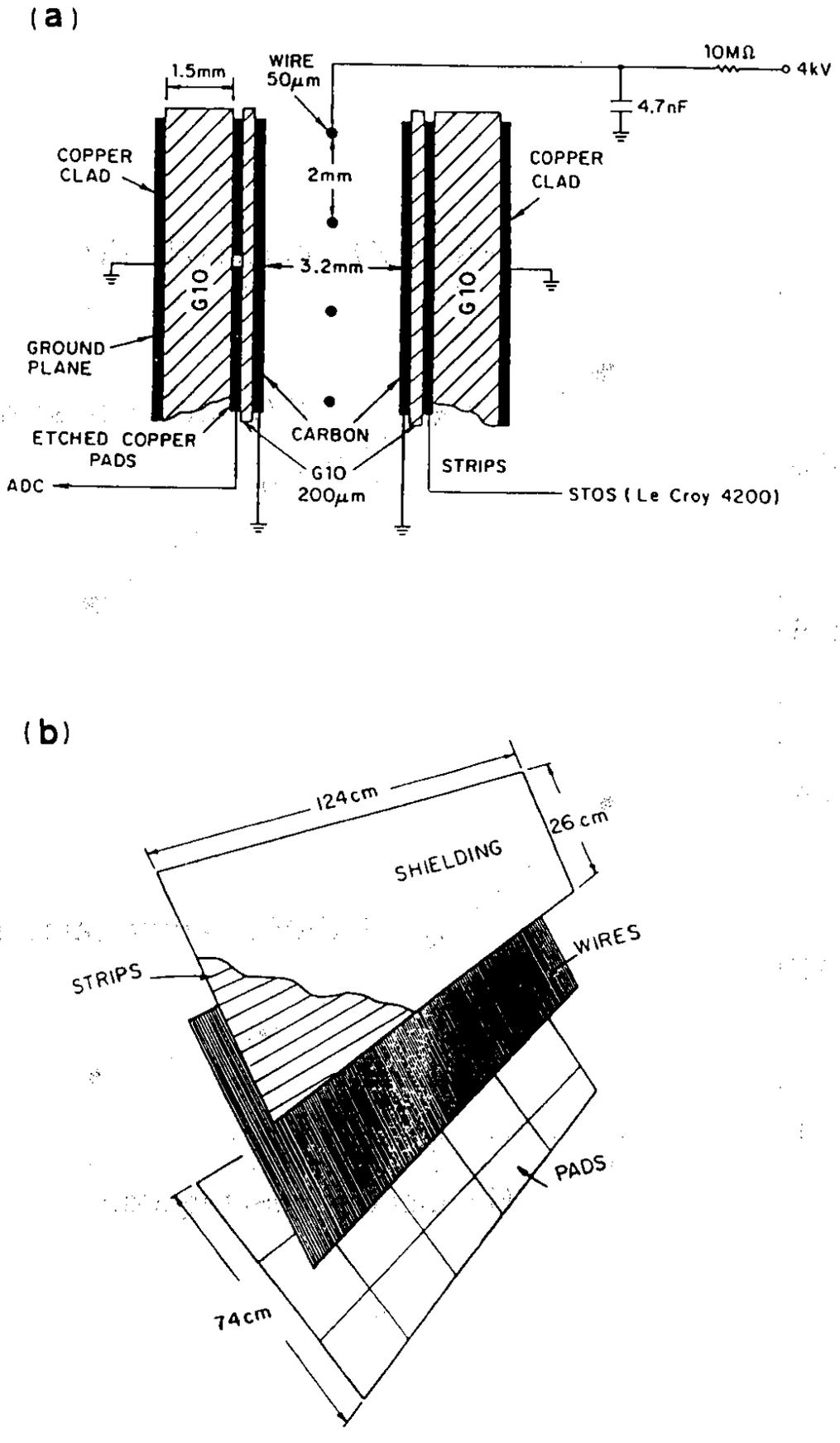
(a)
1.5mm
WIRE
50μm
10MΩ
4kV
4.7nF
COPPER
CLAD
2mm
COPPER
CLAD
3.2mm
G10
G10
GROUND
PLANE
ETCHED COPPER
PADS
CARBON
STRIPS
ADC
G10
200μm
STOS (Le Croy 4200)
(b)
124cm
26 cm
SHIELDING
WIRES
STRIPS
PADS
74cm

Fig. 30

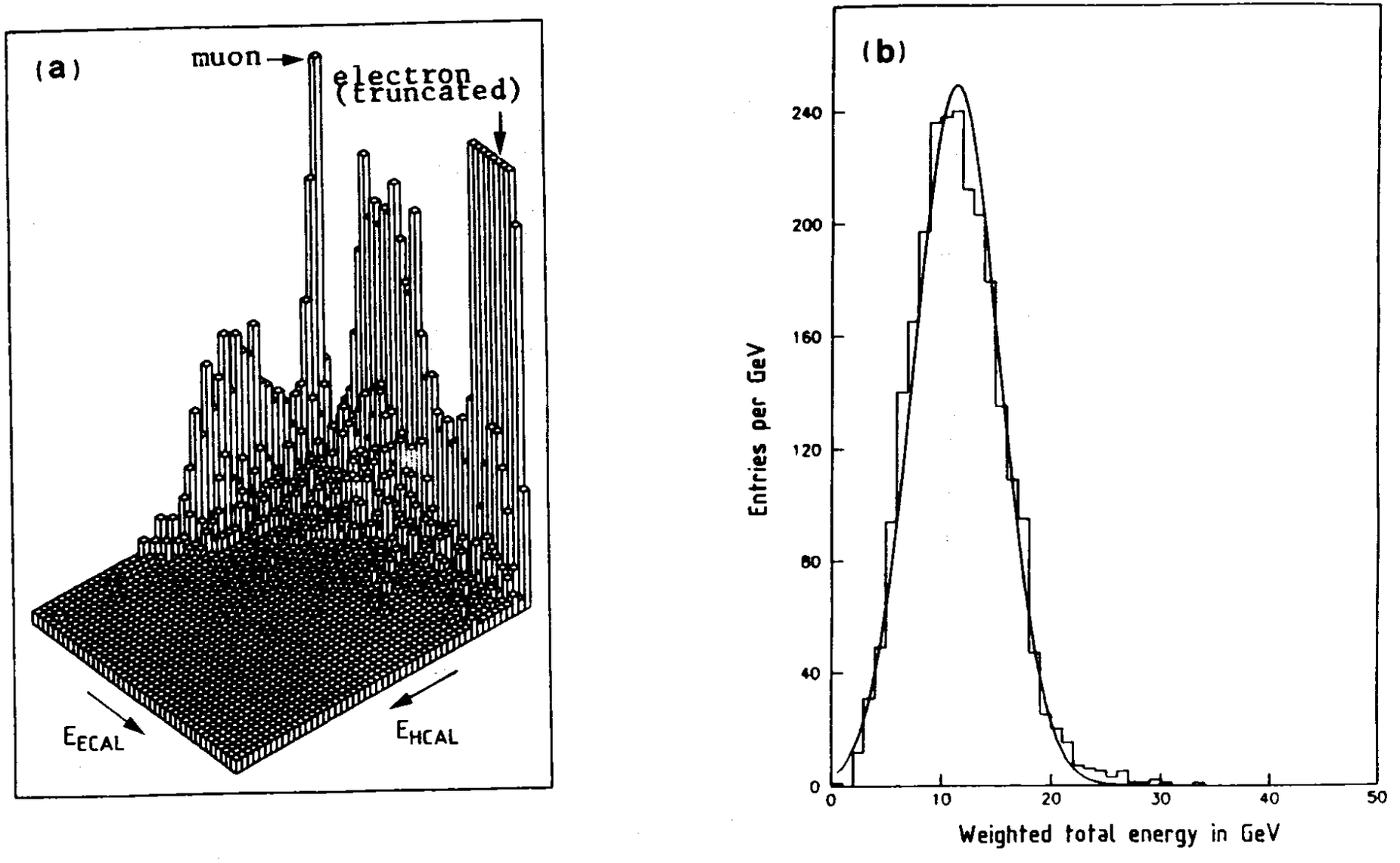
(a)
muon
electron
(truncated)
E_{ECAL}
E_{HCAL}
(b)
Entries per GeV
0
40
80
120
160
200
240
0
10
20
30
40
50
Weighted total energy in GeV

Fig. 31

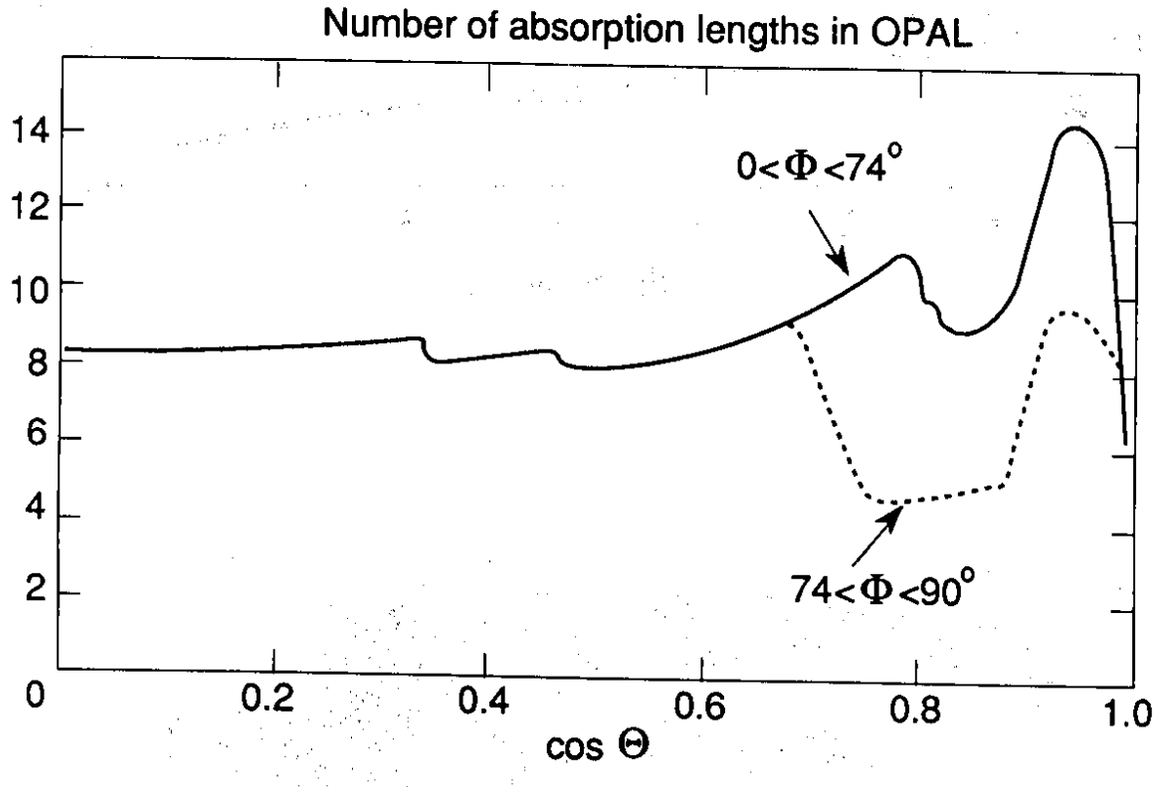
Number of absorption lengths in OPAL
14
12
10
8
6
4
2
0
0.2
0.4
0.6
0.8
1.0
cos Θ
0<Φ<74°
74<Φ<90°

Fig. 32

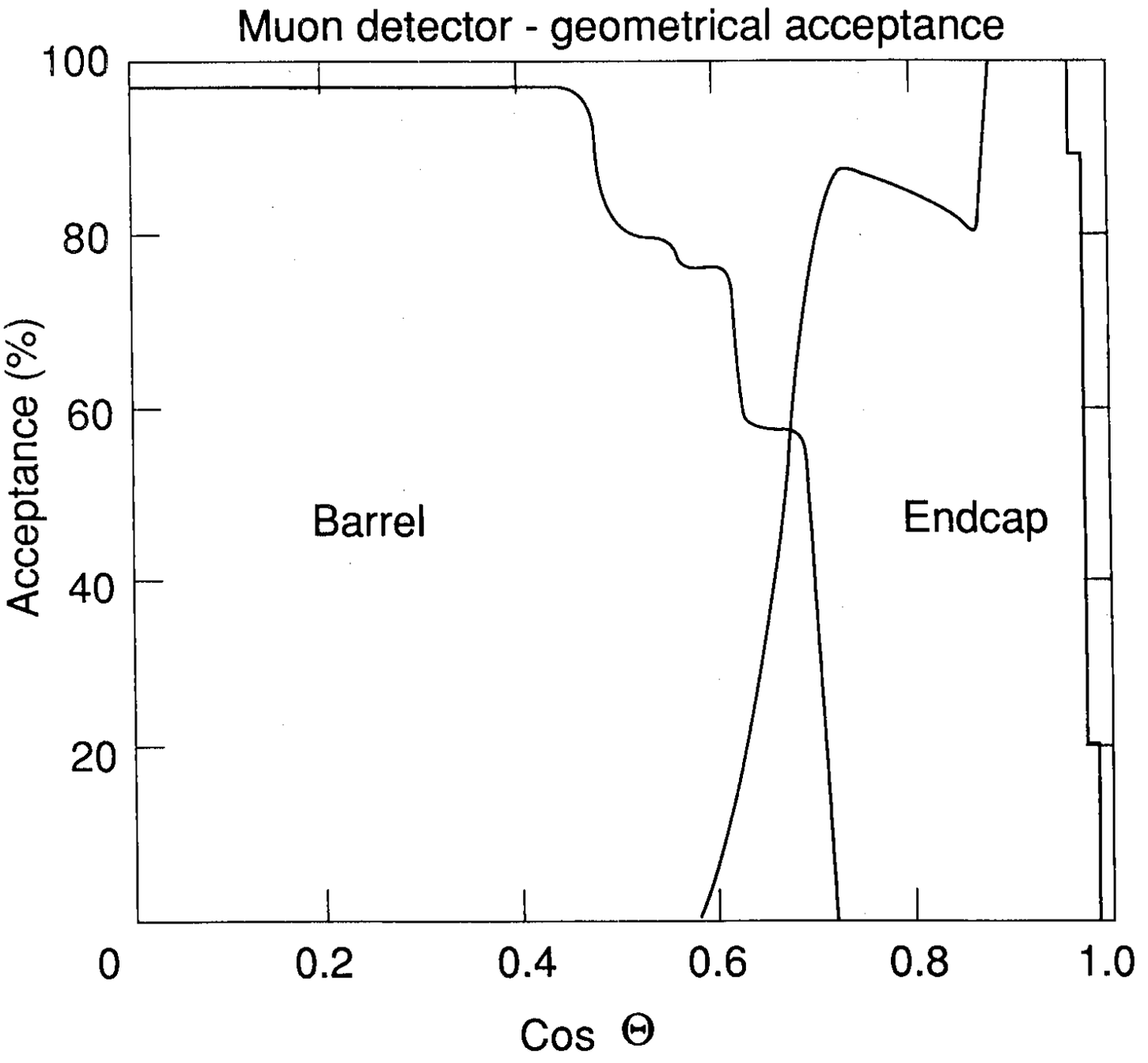
Muon detector - geometrical acceptance
100
80
60
40
20
Acceptance (%)
Barrel
Endcap
0
0.2
0.4
0.6
0.8
1.0
Cos Θ

Fig. 33

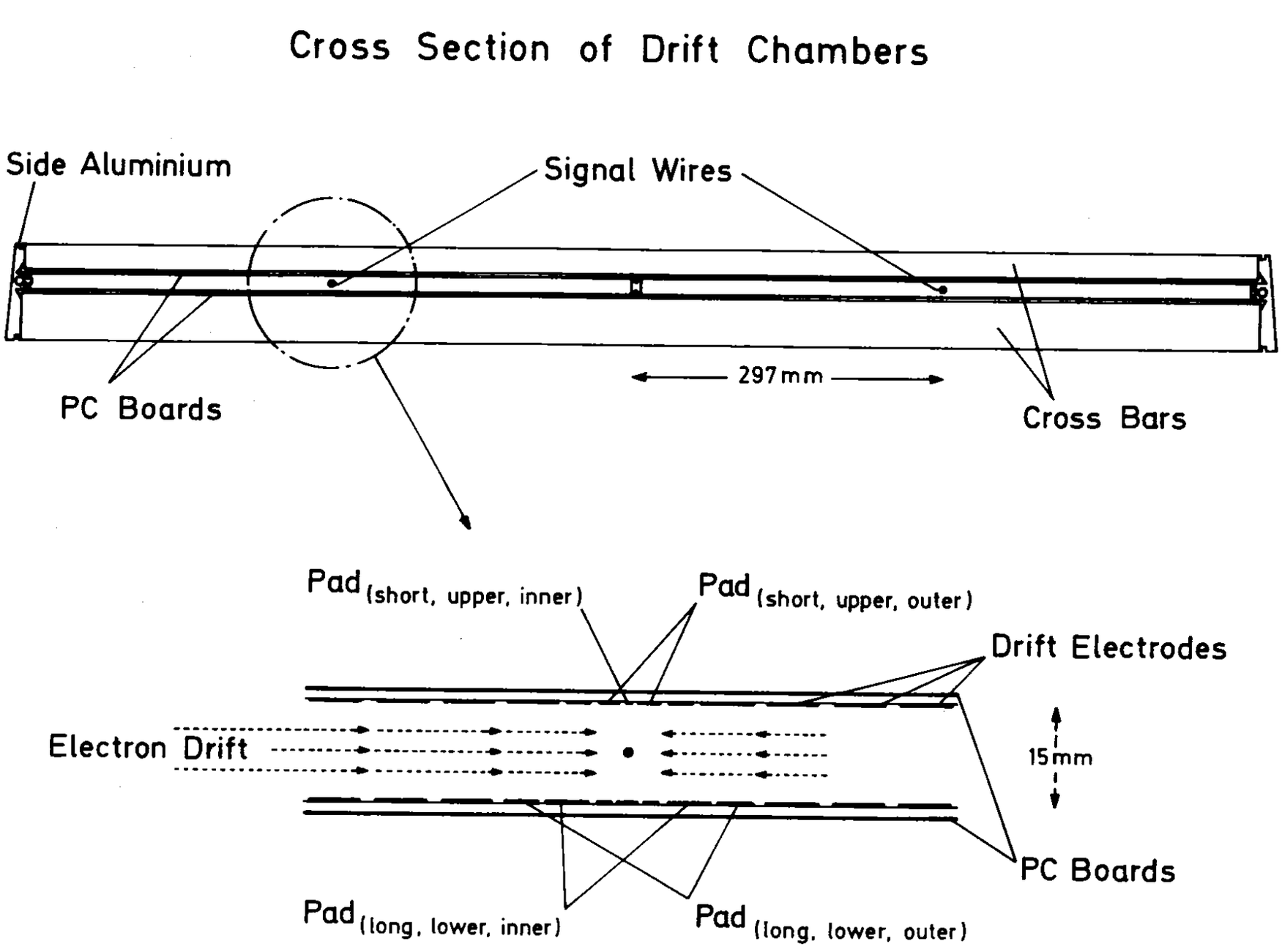
Cross Section of Drift Chambers
Side Aluminium
Signal Wires
297 mm
PC Boards
Cross Bars
Pad (short, upper, inner)
Pad (short, upper, outer)
Drift Electrodes
Electron Drift
15 mm
PC Boards
Pad (long, lower, inner)
Pad (long, lower, outer)

Fig. 34

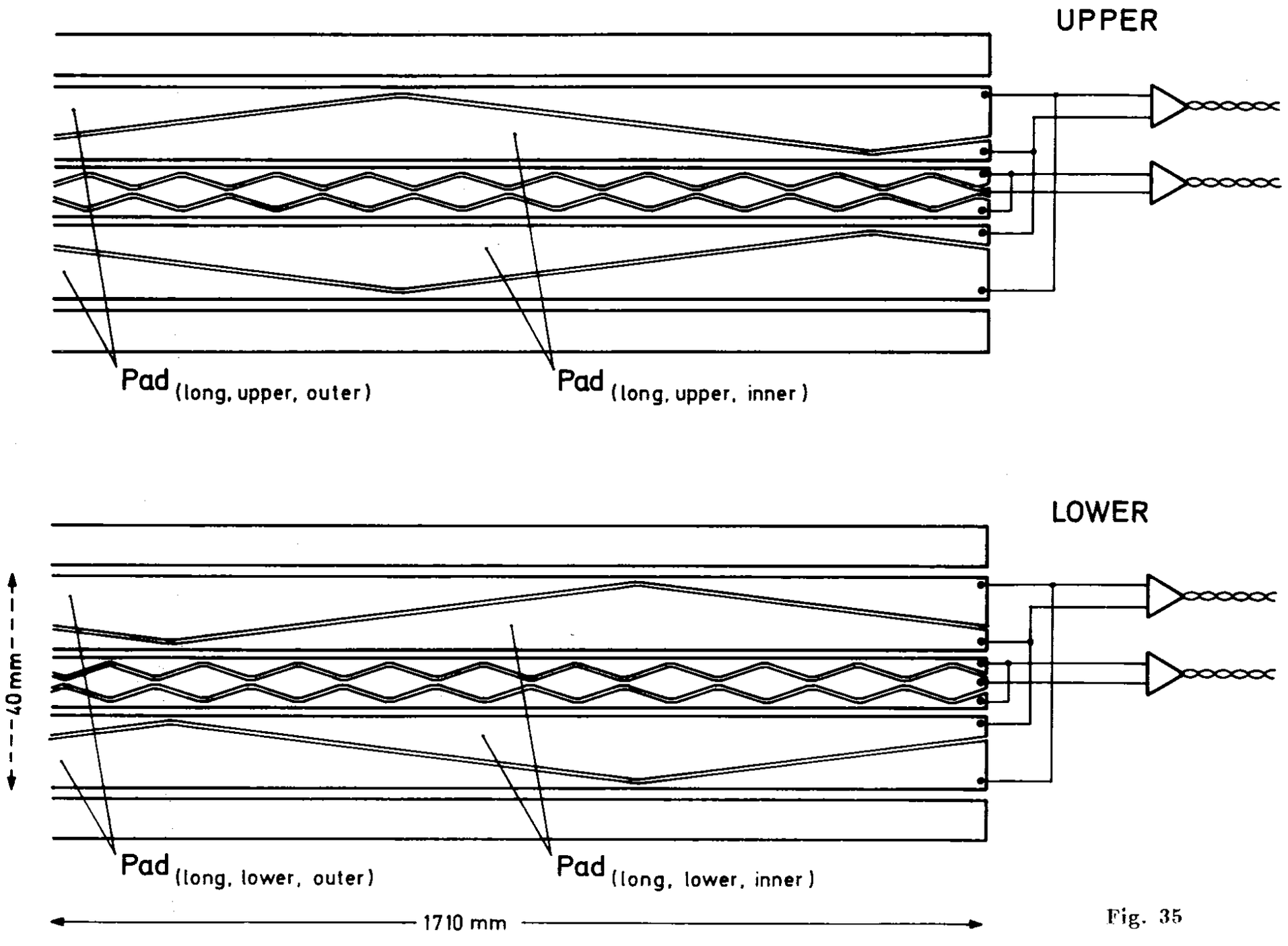
Double Diamond Cathode Pad Structure
UPPER
Pad (long, upper, outer)
Pad (long, upper, inner)
LOWER
40 mm
Pad (long, lower, outer)
Pad (long, lower, inner)
1710 mm

Fig. 35

(a) End view of endcap muon detector.

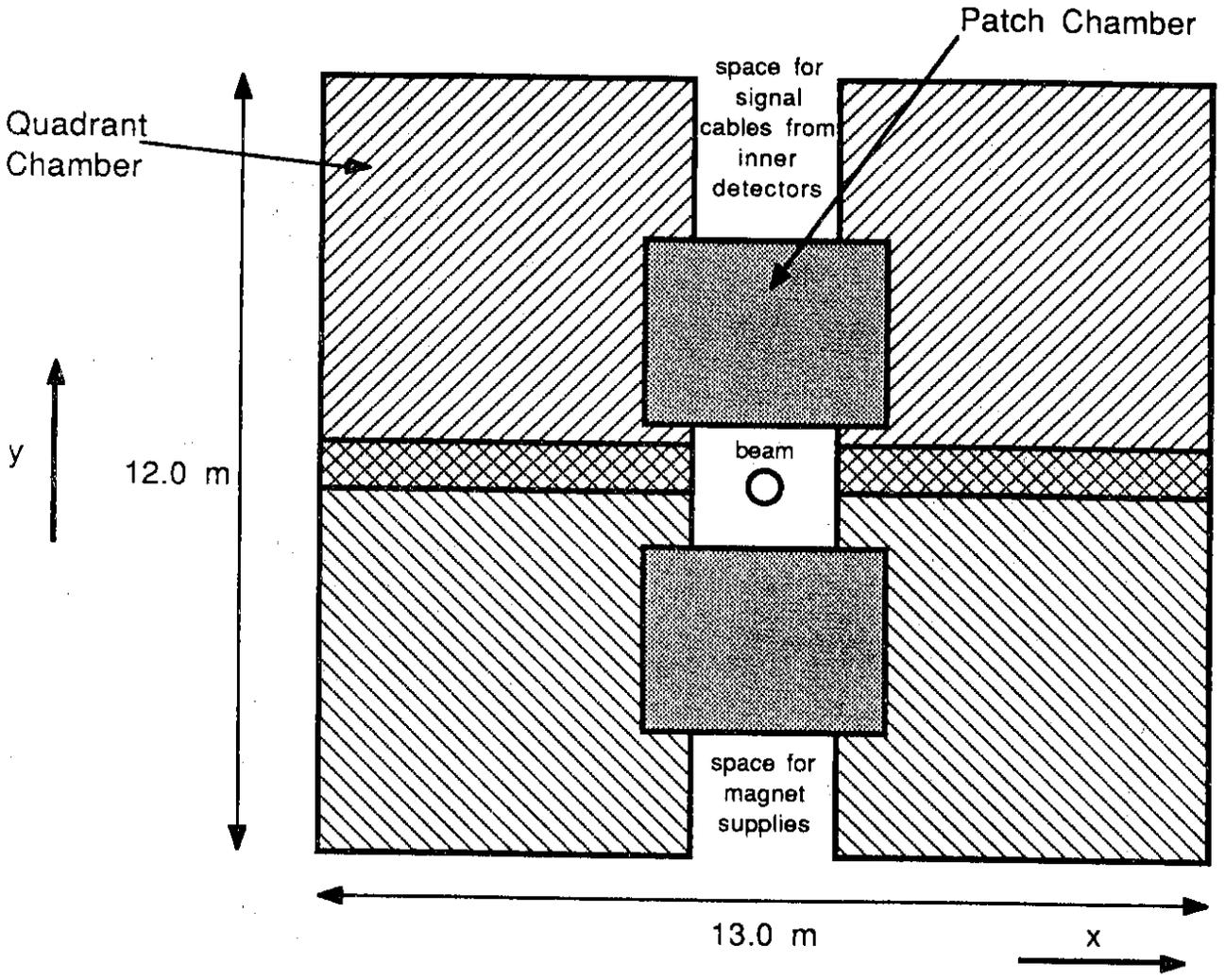

(b) Side view of endcap muon detector.

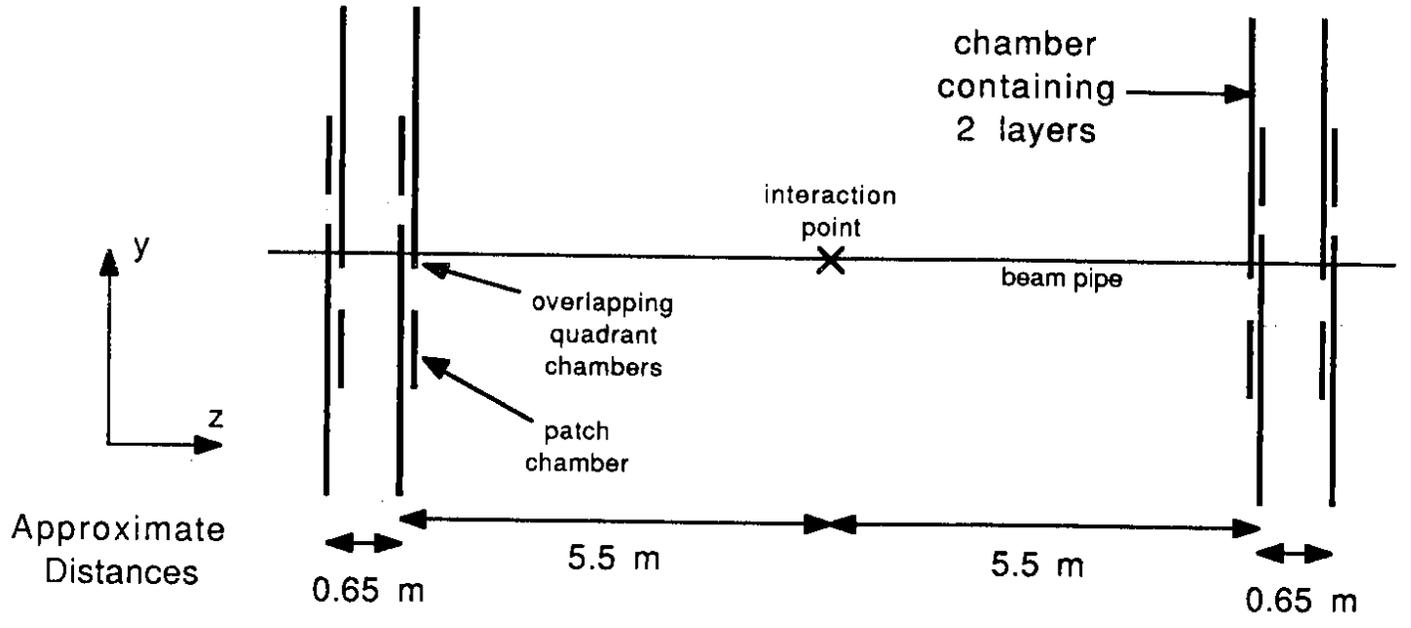

Fig. 36

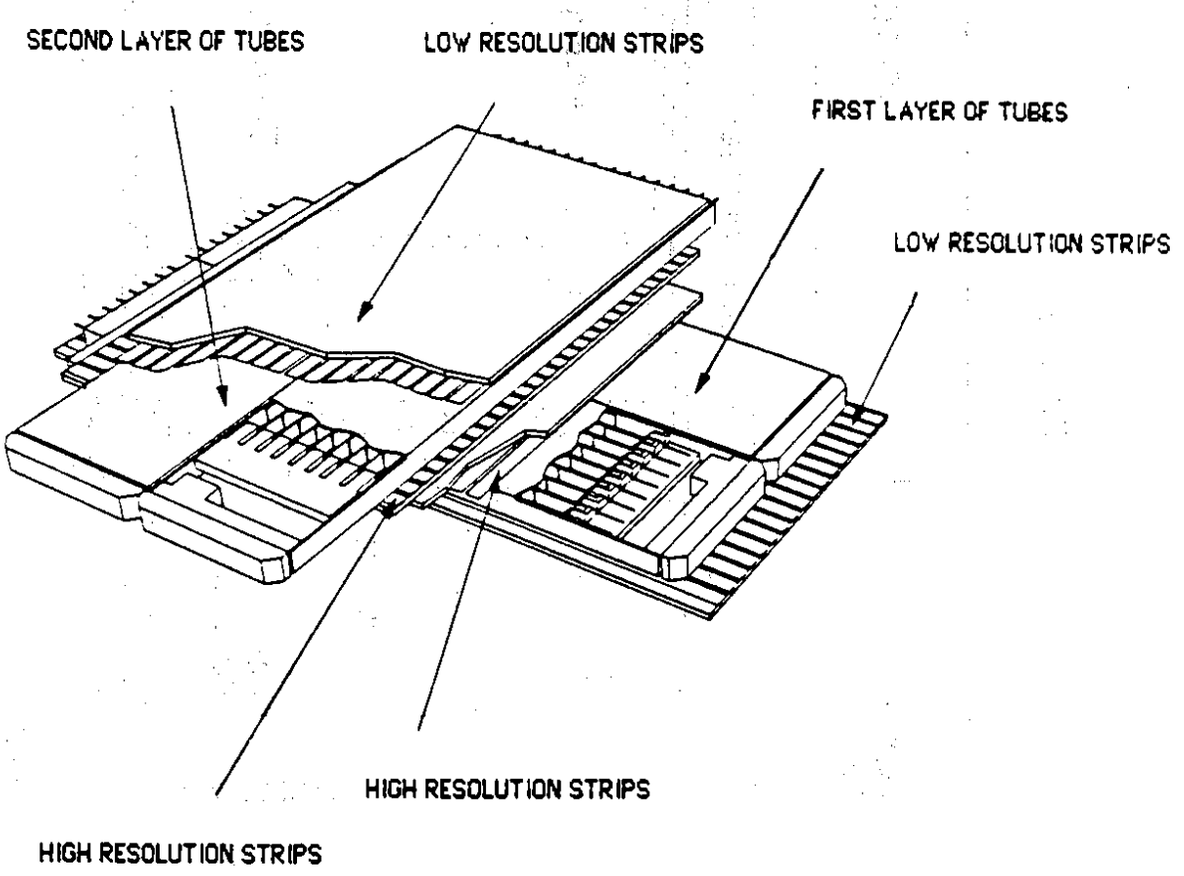
SECOND LAYER OF TUBES
LOW RESOLUTION STRIPS
FIRST LAYER OF TUBES
LOW RESOLUTION STRIPS
HIGH RESOLUTION STRIPS
HIGH RESOLUTION STRIPS

Fig. 37

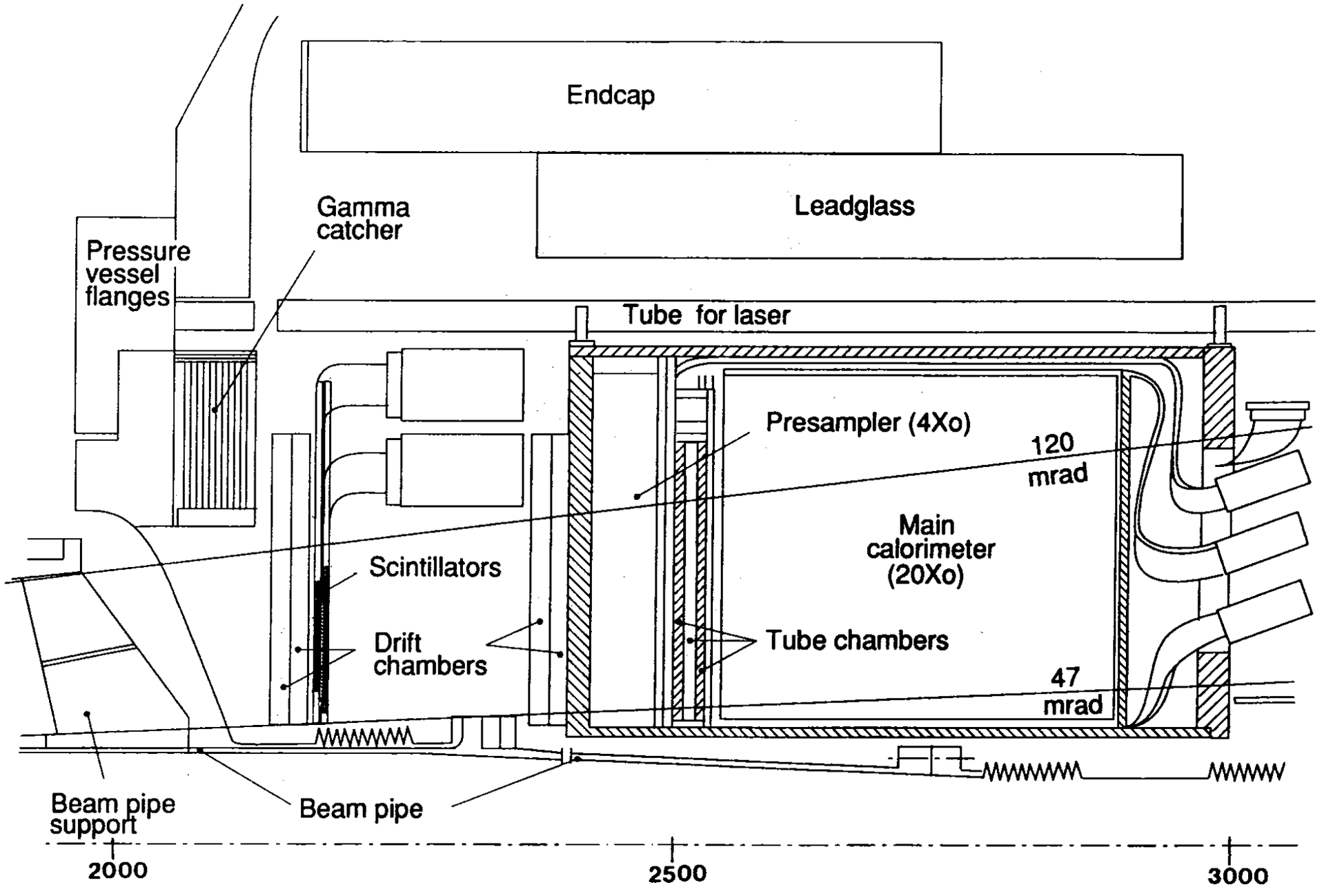
Endcap
Leadglass
Gamma
catcher
Pressure
vessel
flanges
Tube for laser
Presampler (4Xo)
120
mrad
Main
calorimeter
(20Xo)
Scintillators
Drift
chambers
Tube chambers
47
mrad
Beam pipe
support
Beam pipe
2000
2500
3000

Fig. 38

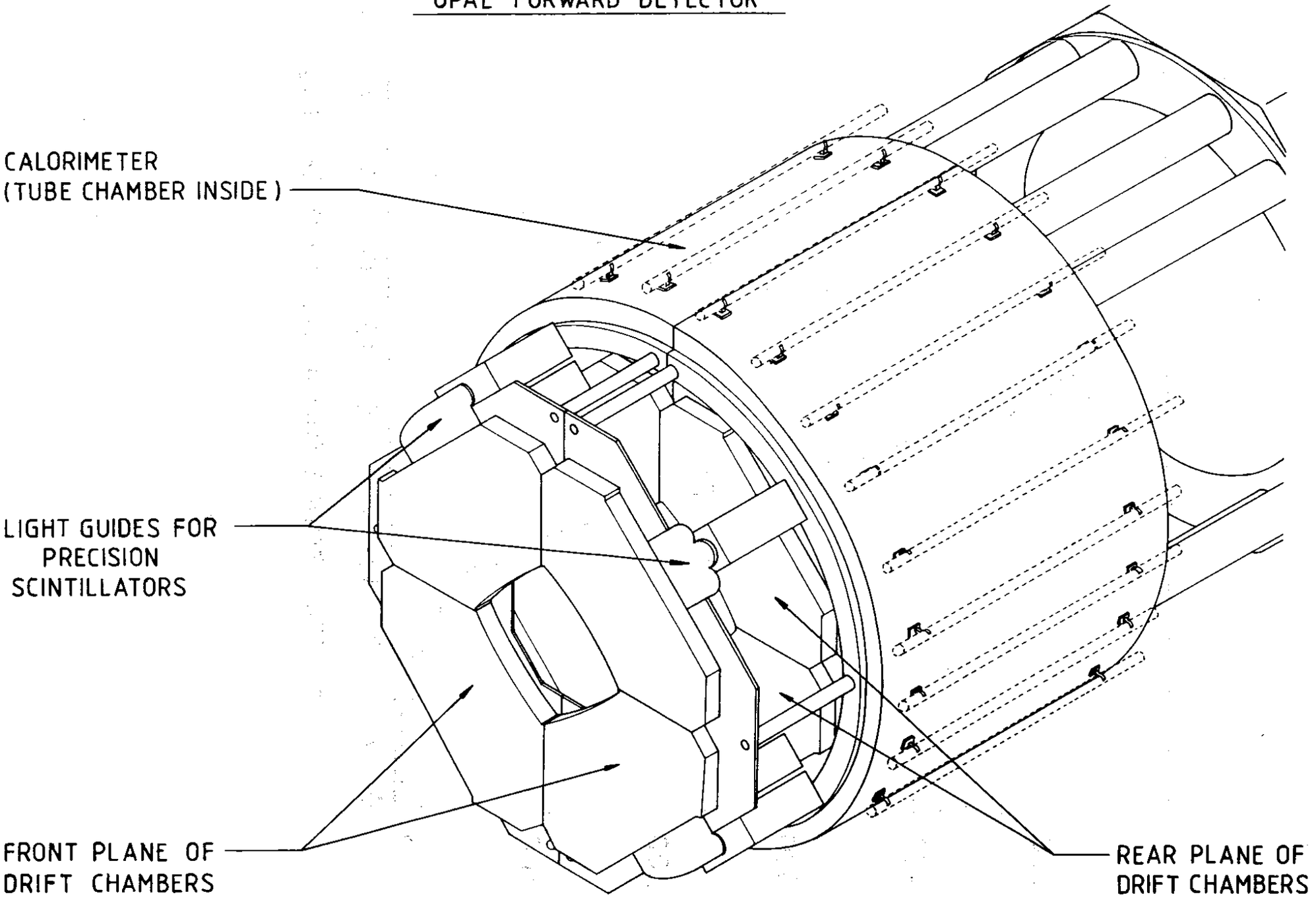
OPAL FORWARD DETECTOR
CALORIMETER
(TUBE CHAMBER INSIDE)
LIGHT GUIDES FOR
PRECISION
SCINTILLATORS
FRONT PLANE OF
DRIFT CHAMBERS
REAR PLANE OF
DRIFT CHAMBERS

Fig. 39

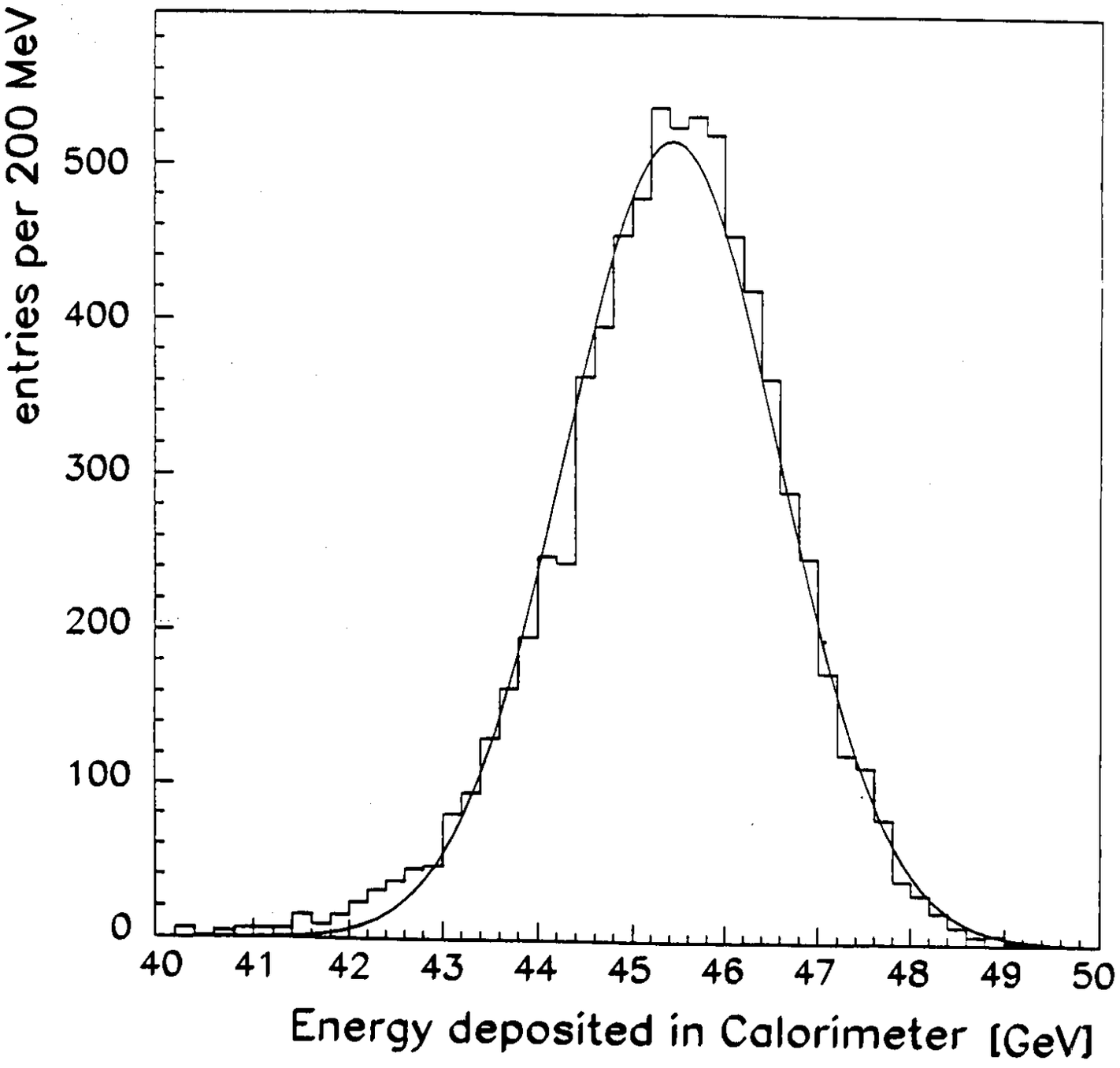
entries per 200 MeV
500
400
300
200
100
0
40
41
42
43
44
45
46
47
48
49
50
Energy deposited in Calorimeter [GeV]

Fig. 40

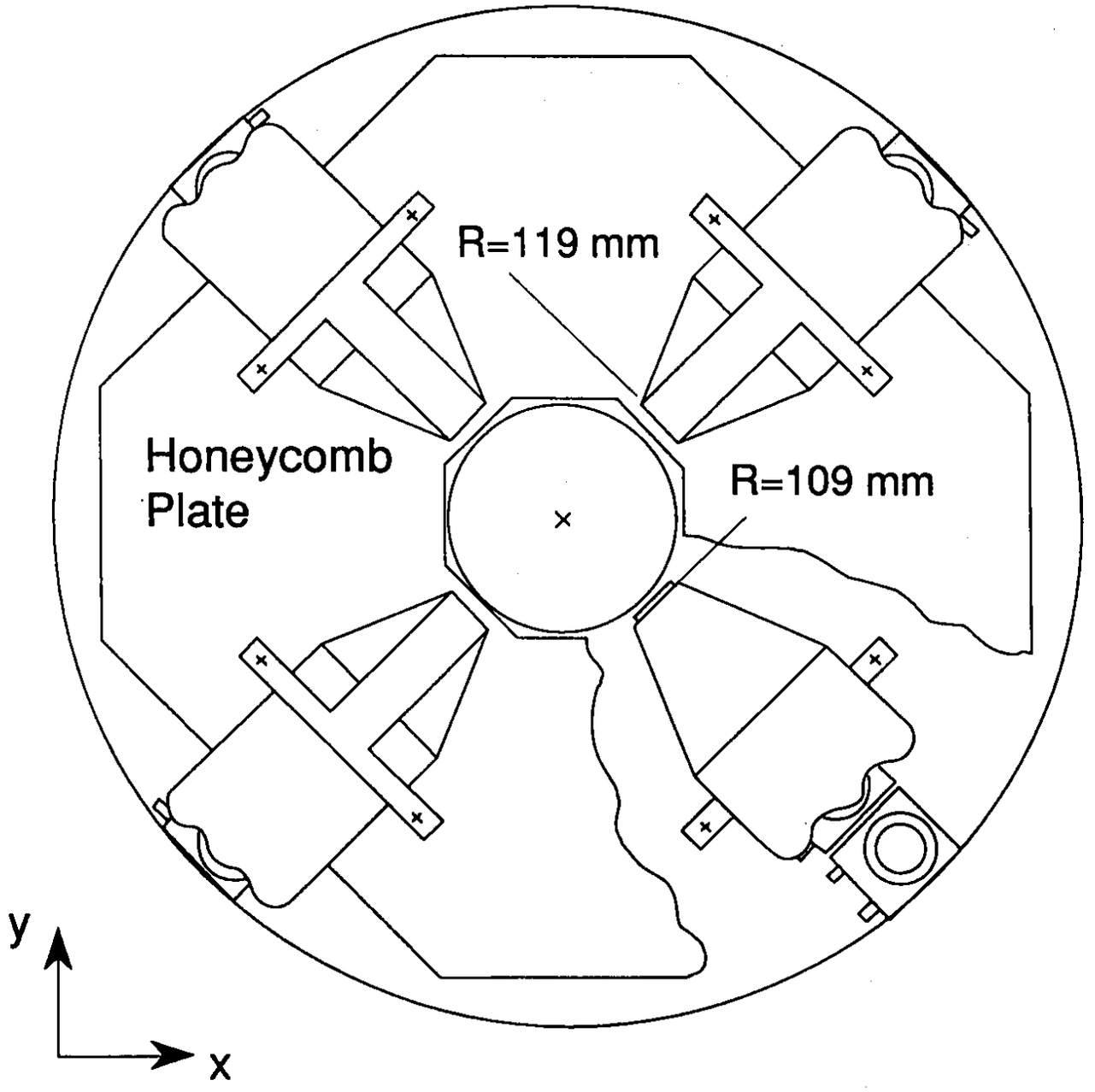

Fig. 41

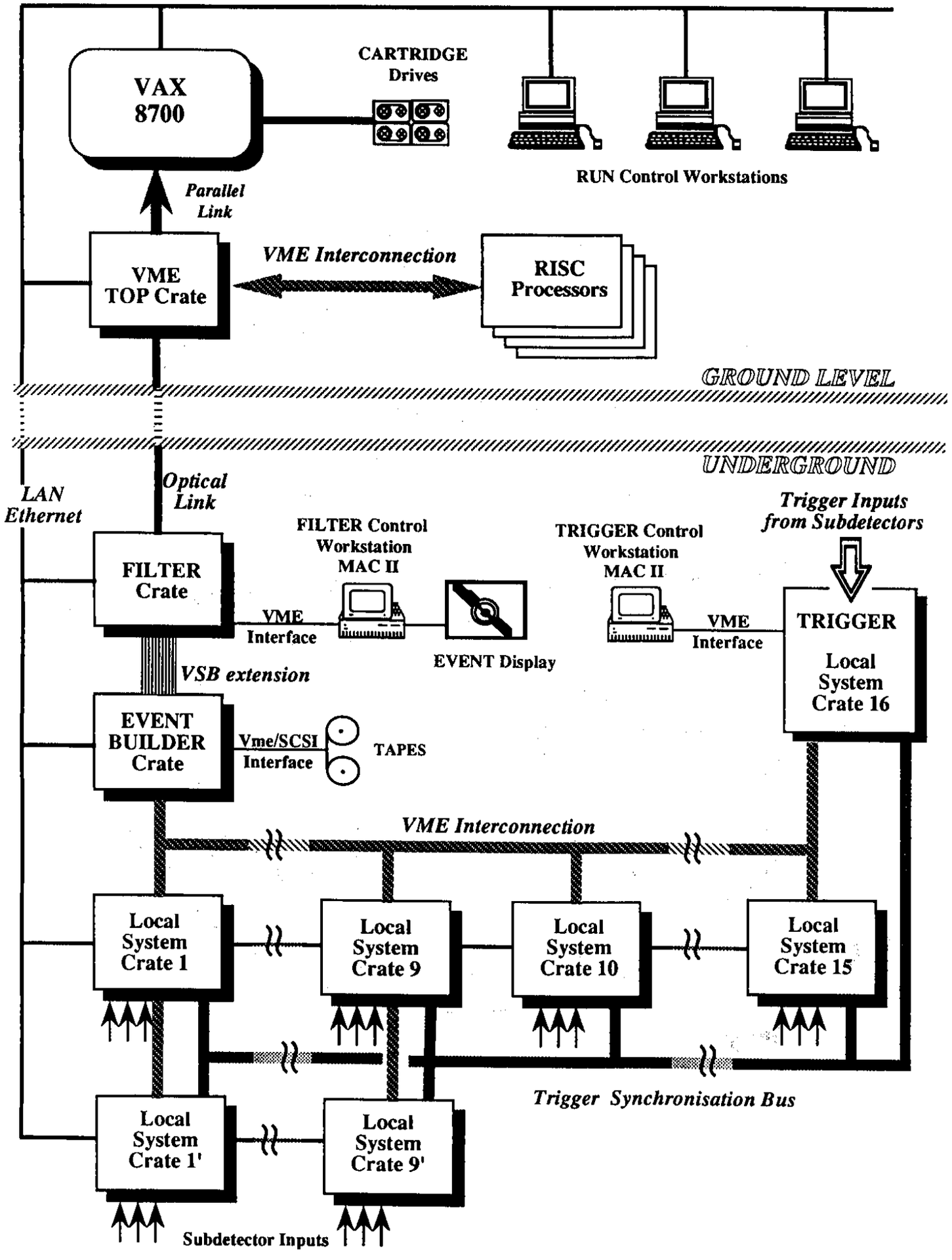
VAX
8700
CARTRIDGE
Drives
RUN Control Workstations
Parallel
Link
VME
TOP Crate
VME Interconnection
RISC
Processors
GROUND LEVEL
UNDERGROUND
LAN
Ethernet
Optical
Link
FILTER
Crate
FILTER Control
Workstation
MAC II
VME
Interface
EVENT Display
TRIGGER Control
Workstation
MAC II
VME
Interface
Trigger Inputs
from Subdetectors
TRIGGER
Local
System
Crate 16
VSB extension
EVENT
BUILDER
Crate
Vme/SCSI
Interface
TAPES
VME Interconnection
Local
System
Crate 1
Local
System
Crate 9
Local
System
Crate 10
Local
System
Crate 15
Trigger Synchronisation Bus
Local
System
Crate 1'
Local
System
Crate 9'
Subdetector Inputs

Fig. 42

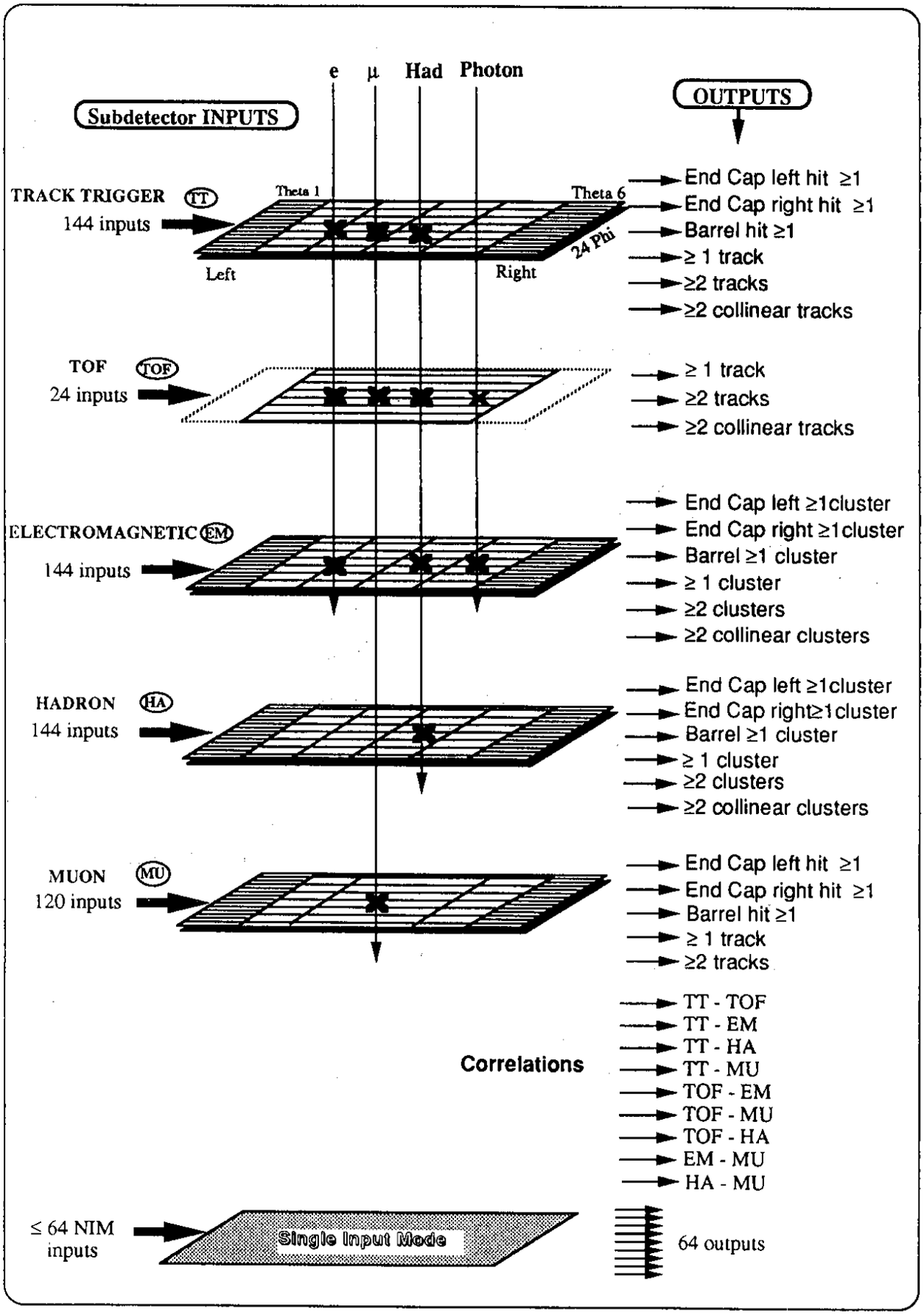
e
μ
Had
Photon
Subdetector INPUTS
OUTPUTS
TRACK TRIGGER TT
144 inputs
Theta 1
Theta 6
24 Phi
Left
Right
End Cap left hit ≥1
End Cap right hit ≥1
Barrel hit ≥1
≥ 1 track
≥2 tracks
≥2 collinear tracks
TOF TOF
24 inputs
≥ 1 track
≥2 tracks
≥2 collinear tracks
ELECTROMAGNETIC EM
144 inputs
End Cap left ≥1cluster
End Cap right ≥1cluster
Barrel ≥1 cluster
≥ 1 cluster
≥2 clusters
≥2 collinear clusters
HADRON HA
144 inputs
End Cap left ≥1cluster
End Cap right≥1cluster
Barrel ≥1 cluster
≥ 1 cluster
≥2 clusters
≥2 collinear clusters
MUON MU
120 inputs
End Cap left hit ≥1
End Cap right hit ≥1
Barrel hit ≥1
≥ 1 track
≥2 tracks
Correlations
TT - TOF
TT - EM
TT - HA
TT - MU
TOF - EM
TOF - MU
TOF - HA
EM - MU
HA - MU
≤ 64 NIM inputs
Single Input Mode
64 outputs

Fig. 43

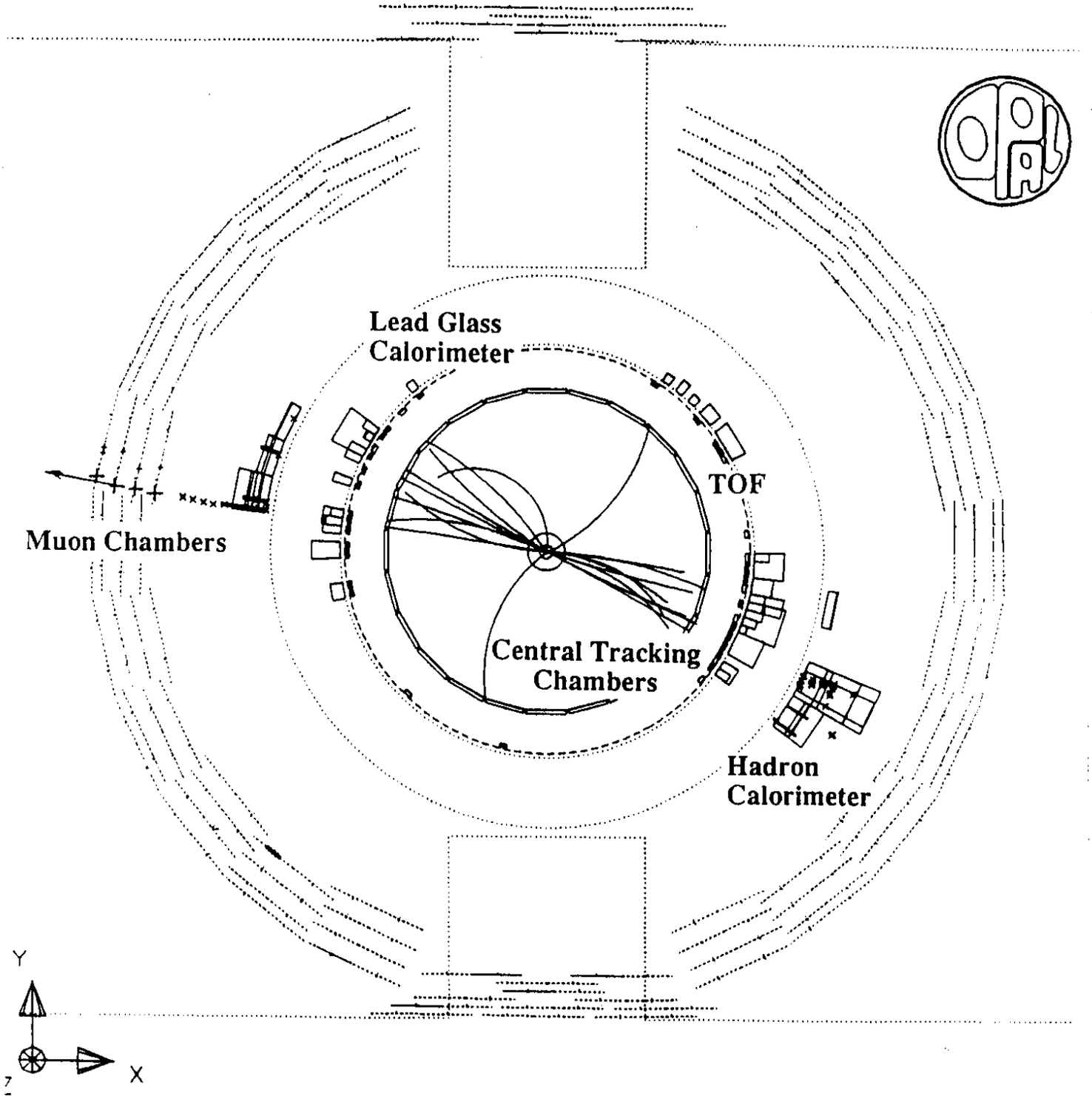

Fig. 44

Imprimé au CERN. Prix : 2.80 Fr.